Fusion Engineering and Design xxx (xxxx) xxx

Contents lists available at ScienceDirect

Fusion Engineering and Design

journal homepage: www.elsevier.com/locate/fusengdes

Stellaris: A high-field quasi-isodynamic stellarator for a prototypical fusion power plant

J. Lion [a,*], J.-C. Anglès [a], L. Bonauer [a], A. Bañón Navarro [b], S.A. Cadena Ceron [a], R. Davies [c], M. Drevlak [c], N. Foppiani [a], J. Geiger [c], A. Goodman [c], W. Guo [a], E. Guiraud [a], F. Hernández [f], S. Henneberg [c], R. Herrero [a], C. Hintze [a], H. Höchter [a], J. Jelonnek [f,g], F. Jenko [b], R. Jorge [e], M. Kaiser [a], M. Kubie [a], E. Lascas Neto [d], H. Laqua [c], M. Leoni [a], J.F. Lobsien [a], V. Maurin [a], A. Merlo [a], D. Middleton-Gear [a], M. Pascu [a], G.G. Plunk [c], N. Riva [a], M. Savtchouk [a], F. Sciortino [a], J. Schilling [a], J. Shimwell [a], A. Di Siena [b], R. Slade [a], T. Stange [c], T.N. Todd [a], L. Wegener [a], F. Wilms [b], P. Xanthopoulos [c], M. Zheng [a]

[a] Proxima Fusion GmbH, Flößergasse 2, Munich, 81369, Germany
[b] Max–Planck-Institute for Plasmaphysics, Boltzmannstr. 2, Garching, 85748, Germany
[c] Max–Planck-Institute for Plasmaphysics, Wendelsteinstr. 1, Greifswald, 17491, Germany
[d] Instituto de Plasmas e Fusão Nuclear, Instituto Superior Técnico, Av. Rovisco Pais 1, Lisboa, 1049-001, Portugal
[e] Department of Physics, University of Wisconsin-Madison, 150 University Ave 2320, Madison, 53706, WI, USA
[f] Institute for Neutron Physics and Reactor Technology (INR), Karlsruhe Institute of Technology (KIT), Kaiserstr. 12, Karlsruhe, 76131, Germany
[g] Institute for Pulsed Power and Microwave Technology (IHM), Karlsruhe Institute of Technology (KIT), Kaiserstr. 12, Karlsruhe, 76131, Germany

ARTICLE INFO

Keywords:
Stellarators
Fusion power plants
Stellarator reactors
Fusion reactor study
Stellarator optimization
Fusion technology
Sector splitting

ABSTRACT

Magnetic confinement fusion research has so far prioritized the tokamak concept, which presents greater design simplicity at the cost of control complexity in comparison to stellarators. Recent progress on high-temperature superconductors (HTS) has enabled a new generation of high-field tokamaks with more compact designs. However, the presence of large magnetic fields implies correspondingly large plasma currents, raising challenges regarding plasma stability. Meanwhile, key milestones have been reached in recent years by Wendelstein 7-X, the world's most advanced stellarator, and breakthroughs in computational optimization have enabled radically improved stellarator designs. In this paper, we present a concept for a new class of quasi-isodynamic (QI) stellarators leveraging HTS technology to overcome well-known challenges of a tokamak. This class of QI-HTS stellarators, labeled Stellaris, is shown to achieve an extensive set of desirable properties for reactor candidates simultaneously for the first time, offering a compelling path toward commercially viable fusion energy. We summarize a comprehensive reactor study, ranging from optimization of the plasma confinement region to first wall cooling, divertor considerations, blanket design, magnet quench safety, support structures, and remote maintenance solutions. Our results demonstrate that a coherent set of trade-offs between physics and engineering constraints can lead to a compelling stellarator design, suited for power plant applications. We anticipate that this work will motivate greater focus on QI stellarators, in both publicly and privately funded research.

1. Introduction

Decarbonization of the energy sector plays a key role in addressing climate change [1,2]. New technologies – including artificial intelligence, with its explosive energy consumption needs – further heighten the need for carbon-free energy sources on an accelerated timeline [3]. Alongside the need for clean electricity, there is growing energy demand for carbon-free heat generation [4], hydrogen [5] and ammonia production [6], water desalination [7], and direct carbon capture from the atmosphere [8].

Fusion stands as a major competitor in the race to supply a significant fraction of the world's future clean energy demands [9]. Economic studies for magnetic confinement extrapolate overnight capacity costs for future fusion power plants in the range of 1–10 $/W [10–13]. Resulting cost estimates for fusion energy range between 20–100 $/MWh [14,

* Corresponding author.
E-mail address: jlion@proximafusion.com (J. Lion).

https://doi.org/10.1016/j.fusengdes.2025.114868
Received 2 September 2024; Received in revised form 20 January 2025; Accepted 6 February 2025

15]. As more detailed cost estimates become available alongside greater maturity of the fusion ecosystem, there are indications that the price of fusion energy will be competitive even relatively early in fusion's technological development [16]. The fuel for fusion is not subject to resource scarcity, as the reactants, deuterium and lithium-6 – as well as neutron multipliers such as Pb, Be, Ti, Mn, or Zr – are abundantly available on Earth, capable of providing virtually limitless resources for future generations. The promise of fusion technology is therefore of the highest relevance for providing human civilization with sustainable energy in the coming centuries.

Under this premise, fusion is being globally pursued through various concepts. Among the magnetic confinement approaches, large-scale projects aiming to close the gap toward a fusion power plant include (but are not limited to) the international research tokamak ITER [17]; the STEP spherical tokamak program [18] in the UK; the high-field conventional tokamak concept of SPARC [19] in the United States, and CFETR [20] in China. Various demonstration device conceptual studies are additionally under investigation [21,22].

While tokamaks have historically been viewed as the clearest path to a fusion power plant, they are prone to plasma disruptions [23], which pose a significant challenge for commercially viable operation. Extensive ongoing scientific efforts aim to solve this issue through prediction [24–26] and mitigation methods [27–30], but there have been no experimental demonstrations that would indicate reliable usage in a power plant setting.

The stellarator is a similar technology to the tokamak, with comparable energy confinement properties [31,32]. However, stellarators with no net toroidal current in the plasma avoid problematic current-driven plasma disruptions by design. These stellarators have the ability to run in steady-state, intrinsically reducing thermal and mechanical component fatigue and eliminating the need for an expensive plasma current drive system. Although in principle tokamaks can also operate in long pulses or even in steady-state, achieving the required steady-state current drive is both technologically challenging and economically demanding, requiring high electrical efficiencies. The absence of current-driven disruptions in current-free stellarators greatly reduces the need for active control of the plasma—circumventing the need for in-vessel coils, which present challenges in environments subjected to high neutron fluxes. Other advantages of stellarators over tokamaks include the absence of a Greenwald-like density limit [33–35], allowing operation at significantly higher densities. This is advantageous because fusion power scales favorably with the square of the fuel density. Furthermore, stellarators do not exhibit the unfavorable 'Eich-scaling' [36] of heat exhaust deposition width on divertor plates seen in tokamaks. On the contrary, stellarators have shown large wetted areas on divertor plates [37–40] and good access to almost complete 'detachment' [41–43], an operation scenario that eases the heat exhaust challenge on the plasma-facing components.

Among the most prominently discussed options, the quasi-isodynamic (QI) stellarator [44] is particularly promising for reactor applications due to its intrinsically minimized self-induced currents, like the bootstrap current [45,46]. Optimized stellarator concepts without QI symmetry can, in general, feature significant toroidal plasma currents. Such concepts present a strong dependency of plasma equilibrium properties on plasma profile shapes, are potentially subject to current-driven disruptions, and – since their bootstrap current does not vanish – likely do not have the ability to use the island divertor concept as an exhaust concept without employing further (unexplored) control systems. Among the investigated stellarator options, the modular, low-shear, QI stellarator holds the highest technological readiness level, following exploration in Wendelstein 7-AS (W7-AS) [47] and the more recent Wendelstein 7-X (W7-X) stellarator [48–50].

W7-X went into operation in 2015, and reached its full design specifications only recently, in 2022. Within a few years, W7-X experiments have demonstrated the reduction of neoclassical transport to a level at which turbulence is the major driver for heat transport in the plasma [51]. It is difficult to overstate the importance of this achievement: W7-X's results demonstrate that optimized stellarators can now be designed to achieve neoclassical transport levels similar to those of tokamaks. Therefore, optimized stellarators are now fundamentally limited by the same physical (turbulent) phenomena that also constrain tokamaks, while maintaining the critical steady-state capability and stability advantages of stellarators.

Table 1
Comparison of the design concept presented in this paper (Stellaris) against the two most recent Wendelstein stellarators. W7-AS values are extracted from [47]. W7-X values are taken from [31].

	W7-AS	W7-X	Stellaris
Minor radius [m]	0.18	0.5	1.3
Major radius [m]	2.0	5.5	12.7
Av. magnetic field strength [T]	2.6	2.5	9.0
Av. power density [MW/m^3]	10	0.3	6.1
Peak ion temperature [keV]	1.7	3.4	15
Peak electron density [10^{20} m^{-3}]	4	2	5
Peak triple product [keV s m^{-3}]	4.6×10^{18}	5.1×10^{19}	12.4×10^{21}

Historically, stellarator reactor concept studies such as the ARIES-CS study [52], the extrapolation of LHD to heliotron-based fusion reactors [53,54], or the HELIAS studies [55–60] have provided important platforms for the fusion community to discuss the extrapolation of physics and the validity of concepts from experiment to reactor scale. However, despite successful operation of W7-X [50,51,61,62], one cannot merely scale W7-X to an economically attractive reactor size, due to a number of known limitations including high fusion-born fast particle losses [63], insufficient plasma-coil distance to fit a neutron shield and blanket at moderate machine sizes [12,64], and high turbulent transport levels, particularly ITG transport [65,66]. Moreover, W7-X's usage of NbTi as a superconductor [67] does not easily scale to the magnetic field strength required for a reactor.

In recent years, the community has proposed various solutions to address these challenges. For example, fast particle losses can be mitigated through precise numerical optimization techniques [68–72]. The issue of insufficient plasma-coil distance has been tackled with new cost functions for stellarator optimization [73] and more compact blanket designs [10]. Turbulent transport suppression has been demonstrated in the presence of strong density gradients [74–77] as well as in plasma geometry optimization efforts [71,78–81]. Additionally, advances in high-temperature superconductors (HTS) have paved the way for achieving higher magnetic field strengths in modern devices [82–85]. Despite this, there is currently no comprehensive stellarator reactor concept study that simultaneously integrates these developments into a single, coherent design. Therefore, it remains unclear whether these advancements can be effectively combined to create a stellarator that is viable for commercial power plants while remaining feasible from an engineering perspective.

In this paper, we aim to bridge that existing gap by presenting a stellarator configuration optimized for all essential reactor aspects, including an engineering feasibility study. We argue that the configuration and concept introduced here offer a promising pathway to a D-T stellarator power plant. This study extends recent breakthroughs in the numerical optimization of QI stellarator plasma shapes, specifically the 'SQuiD' configurations [70,71], toward a viable stellarator fusion reactor.

The design introduced here represents the first of a new class of QI stellarator designs harnessing the high-field potential of HTS magnets. In this paper, the first conceptual design within this class is denoted as Stellaris.

Relevant machine parameters of Stellaris are highlighted in Table 1, providing a comparison to the two most recent Wendelstein stellarators. Note that not all peak values displayed in this table were achieved in the same experiment for each device—peak density values were achieved independently of the peak temperatures. Stellaris represents

a significant leap in scale and performance, being approximately 2.6 times larger in major radius than W7-X and operating at a magnetic field strength that is 3.6 times higher. This substantial increase in size and magnetic field strength results in an anticipated triple product that is roughly 200 times larger than that of W7-X.

The paper is structured as follows. In Section 2.1, we provide an overview of Stellaris. We present an analysis of plasma properties in Section 2.2, and the physics basis in Section 2.3. An engineering analysis is then presented, focusing on fueling (Section 2.4), heating (Section 2.5), divertor design (Section 2.6), a thermal analysis of the first wall (Section 2.7), neutronics for the first wall, the blanket and neutron shield (Section 2.8), magnets (Section 2.9), support structures (Section 2.10), and a remote maintenance solution (Section 2.11). In Section 3, we summarize the achievements presented in this paper and the impact we anticipate they will have on fusion research.

2. Concept and analysis

In this section, we provide an overview of the Stellaris concept and proceed through different aspects of analysis, ranging from physics to engineering properties.

2.1. Overview

Stellaris is a quasi-isodynamic stellarator device with modular coils, a minimized toroidal plasma current, a magnetic island chain at the edge allowing for an island divertor, and HTS superconducting magnets. The device closely follows the W7-X stellarator model, with the addition of multiple improvements necessary for a reactor candidate. The device features a 4-fold discrete rotational symmetry ('number of field periods') in addition to 'stellarator symmetry', an internal discrete flip-mirror symmetry [86].

The underlying plasma configuration of Stellaris belongs to the class of recently proposed SQuID-configurations [71], adapted to meet the requirements of a power plant by dedicated optimization for larger coil-plasma distances. Key parameters of the device are displayed in Table 2. The major radius is approximately 12.7 m while the minor radius is 1.3 m. By comparison, ITER has a minor radius of about 2.0 m [87] and the ARC tokamak concept approximately 1.1 m [10]. We adopt high-temperature superconductors for the modular coils, and remote maintenance is enabled through the splitting of modular sectors. The device is sized to provide about 2700 MW of peak fusion power. Considering the power multiplication incurred in the blanket (Section 2.8), Stellaris is predicted to produce approximately 3150 MW of thermal power and (assuming a simple electrical conversion efficiency of 1/3) nearly 1 GW of electrical power.

A schematic view of the device is shown in Fig. 1. A comparison of component sizes with ITER and ARC is shown in Fig. 2. We note that the displayed machines have different plasma volumes and fusion power targets: for ITER, $V = 840$ m^3 and $P_{\text{fusion}} = 500$ MW; for ARC, $V = 141$ m^3 and $P_{\text{fusion}} = 500$ MW; for Stellaris, $V = 425$ m^3 and $P_{\text{fusion}} \approx 2700$ MW. As shown in Fig. 2, although Stellaris has a larger volume than ARC, its non-planar magnets are analogous in size to the TF magnets of ARC, and are smaller than the ARC Poloidal Field (PF) magnets (not shown).

In the following section, we survey the different subsystems of Stellaris, beginning with attributes of the plasma configuration with different profile shapes and proceeding to expected physics properties, followed by requirements of the heating system to achieve the chosen operational point, analysis and design of the divertor concept, the first wall, blanket, shield, coils, and support structure, and finally, the remote maintenance concept.

Table 2
Key parameters of Stellaris, the high-field stellarator fusion power plant concept presented in this paper. ECRH stands for 'electron cyclotron resonance heating'.

Variable	Value
Minor plasma radius [m]	1.3
Major plasma radius [m]	12.7
Plasma aspect ratio [1]	9.8
Plasma volume [m^3]	428
Plasma surface area [m^2]	940
Axis av. magnetic field strength [T]	9.0
Peak conductor magnetic field strength [T]	24.9
Peak coil current (single coil) [MA]	15.4
Number of toroidal field coils [1]	48
Stored magnetic energy [GJ]	111
Required plasma-coupled ECRH power [MW]	50
Peak fusion power [MW]	~2700
Peak thermal power (after blanket multiplication) [MW]	~3150
Peak electric power [MW]	~1000
Peak neutron wall load [MW m^{-2}]	4.05

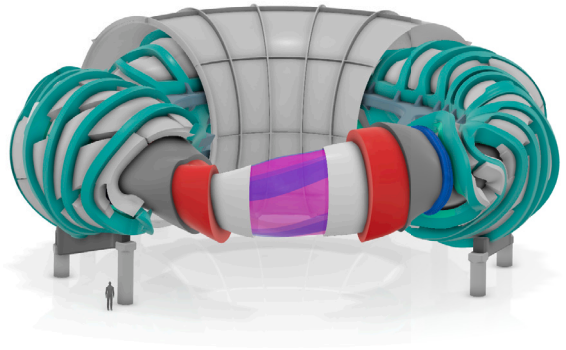

Fig. 1. Overview of Stellaris. Pictured here are the non-planar modular coils (green), the support structure (light grey) and the cryostat (outermost grey shell). The red region indicates the blanket. Blue 'stripes' around the (pink) plasma show the location of the magnetic islands which are used to divert the plasma at the edge. One sector splitting interface is shown in blue. The inner radius of the cryostat is 6.5 m, its outer radius is 18 m. A person is shown for scale.

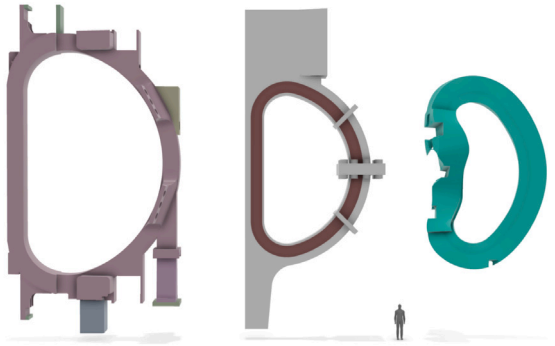

(a) (b) (c)

Fig. 2. Size comparison between one of the ITER TF coils (a), one of the ARC tokamak TF coils [10] (b), and one of the non-planar stellarator coils of Stellaris (c).

2.2. Plasma properties

The stellarator plasma and its properties are of central importance to all reactor subsystems. The stellarator configuration employed here is a variant of the family introduced in [71], called 'SQuIDs'. The plasma configuration for Stellaris was optimized to allow for distant coils using the target formulation from [73] and low fast particle losses using a precise QI formulation from [70].

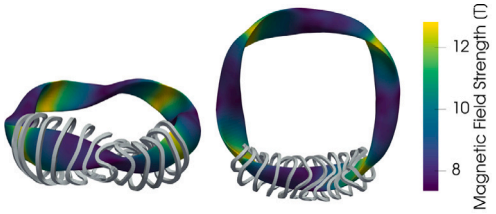

Fig. 3. Visualization of the QI stellarator configuration used for Stellaris. Shown is the VMEC free-boundary plasma boundary at $\langle\beta\rangle_V = 3\%$ with its magnetic field strength. Corresponding coils are shown with their (correctly sized) winding packs for one rotationally symmetric module (one full field period).

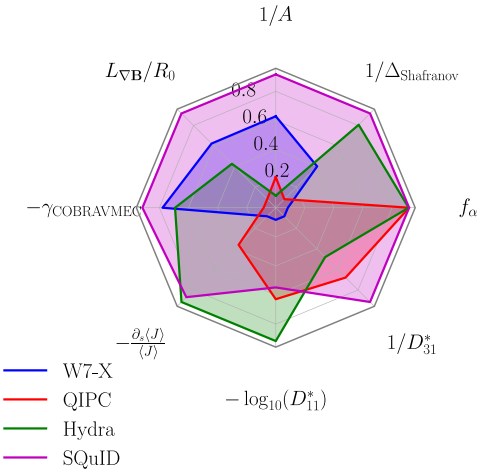

Fig. 4. Comparison between the proposed QI configuration (SQuID) and 3 previously published configurations: W7-X [91],QIPC [92,93], and Hydra [94]. Radial values are normalized by the largest (outermost) and smallest value in the set of configurations. The metrics included in the plot summarize a subset of the reactor-relevant requirements listed in Section 2.2; see Section 2.2 for a description of each dimension. Each configuration is evaluated at its optimized volume-averaged plasma β value. The meaning of the axis labels are explained in the main text.

The configuration used for this study satisfies all relevant reactor requirements simultaneously, including feasible modular coils that leave sufficient space for the required thickness of shielding and breeding materials surrounding the plasma, good flux surface quality at finite β, equilibrium resiliency with respect to finite β effects, ideal-MHD stability, reduced neoclassical transport, and compatibility with the island divertor concept. Additionally, at a sufficiently high peak electron temperature of about 19 keV, the configuration has the ability to prevent impurity accumulation in the plasma core by creating a positive radial electric field. Details on the methodology used to obtain the stellarator configuration are obtainable from Ref. [71]. The rotational transform is chosen to have values between 0.86 on the axis and 0.98 at the edge, avoiding low order resonances in the main confinement volume. The corresponding set of electromagnetic coils is optimized by minimizing the normal component of the magnetic field vector on the last flux surface of the plasma boundary, as introduced in [88]. The total magnetic field is the superposition of the vacuum field generated by the electromagnetic coils and the field generated by the plasma currents. We use the virtual casing principle [89], as numerically implemented by [90], to compute the field generated by the plasma currents. The coils, together with plasma boundary at the targeted β value of $\langle\beta\rangle_V = 3\%$, are shown in Fig. 3.

Table 3 presents several high-level plasma and engineering parameters of the stellarator plasma and its coil-set.

In this paper, unless otherwise stated, we use the free-boundary equilibria obtained with the VMEC code [95] for analysis. The term

Table 3
Main configuration parameters of Stellaris scaled to a minor radius of $a = 1.3$ m. Coil information provided in this table refers to the center filament. Additional information is given in Section 2.2 and in Section 2.9.

Description	Value
Aspect ratio [1]	9.8
Optimized vol. av. β [1]	0.03
Axis rotational transform [1]	0.86
Edge rotational transform [1]	0.98
Edge mirror ratio [%]	26.66
Minimum coil-plasma distance [m]	1.37
Minimum coil-coil separation [m]	0.67
Minimum radius of curvature [m]	0.64

'free-boundary' refers to a plasma equilibrium that is obtained consistently with the vacuum field produced by the electromagnetic coils. The engineering feasibility of the coil-set of Stellaris will be discussed in more detail in Section 2.9.

We visualize the performance of the plasma in a number of relevant metrics in Fig. 4, by comparing it to previously published QI stellarator plasma configurations [91–94]. The diagram showcases a 'performance' plot where outermost values depict highest performance and innermost values depict lowest performance. In this diagram, W7-X [91] refers to the standard configuration of the W7-X experiment at $\langle\beta\rangle_V \sim 4\%$ [96]. The QIPC [92,93] stellarator configuration is a high-β, $\langle\beta\rangle_V \sim 8.5\%$, configuration with improved QI quality and MHD stability with respect to W7-X. Hydra [94] is a proposed QI stellarator configuration that achieves low neoclassical transport, good confinement of fast particles, and reduced integrated bootstrap current with respect to W7-X.

Fig. 4 summarizes the following properties:

- 'A' refers to the configuration aspect ratio $A = \frac{R}{a}$, where a is the plasma minor radius, and R is the major plasma radius;
- '$\Delta_{\text{Shafranov}}$' denotes the Shafranov shift at a volume-averaged β of $\langle\beta\rangle_V \sim 3.0\%$, indicative of the equilibrium resiliency;
- 'f_α' denotes the fraction of confined collision-less energetic particles when launched from mid-radius ($\rho = 0.5$) evaluated with the SIMPLE code [97,98];
- '$-\frac{\partial_s\langle J\rangle}{\langle J\rangle}$' measures the strength of the maximum-J property at $s = 0.5$, and the maximum value across all bounce orbits have been considered. The maximum-J property benefits the confinement of energetic particles [70,99], improves MHD stability [100–102], and suppresses TEM driven turbulence [76,103–105];
- 'D^*_{11}' refer to the mono-energetic radial transport coefficients and indicates the degree of neoclassical particle and energy confinement quality [106];
- 'D^*_{31}' is the mono-energetic bootstrap current coefficient. Both, D^*_{11} and D^*_{31} are obtained with the SFINCS code [107] at mid-radius, for a reference collisionality and normalized radial electric field strength of $\nu^* = 1 \times 10^{-4}$ and $\nu^*_E = 1 \times 10^{-4}$, respectively. Background information, including nomenclature for the normalization chosen can be found in [106] and in [108];
- '$\gamma_{\text{COBRAVMEC}}$' is the highest growth rate in the plasma volume for the ideal-MHD infinite-n ballooning mode evaluated with the COBRAVMEC code [109];
- and finally, '$L_{\nabla\mathbf{B}}$' is the minimum magnetic field gradient length at the plasma boundary, as proposed in [73], which influences the feasibility and distance of the modular coils from the plasma.

For consistency, all dimensions in Fig. 4 are normalized using the minimum and maximum values across all configurations analyzed. Fixed-boundary metrics (i.e., metrics obtained from the equilibrium magnetic field using the optimized plasma boundary as boundary condition) are used for the comparison, as coil information is not available for every configuration. Fig. 4 demonstrates that the proposed QI plasma configuration presented in this paper improves upon the W7-X

configuration in all evaluated metrics.

In the following paragraphs, we offer a more detailed analysis of performance metrics that are particularly important for reactor-relevant plasma configurations.

Fast particle confinement. To evaluate the configuration's confinement of fusion-born alpha particles, we evaluate both collisionless and collisional losses.

We first simulate collisionless trajectories within the plasma volume using the symplectic gyro-center code SIMPLE [97,98] and neglect radial electric fields and slowing-down effects. Any wave-particle interactions of the fast particle population are neglected in SIMPLE.

In SIMPLE simulations, we launch a total of 2×10^5 particles, each with an initial energy of $E_\alpha = 3.5\,\mathrm{MeV}$, close to the original alpha particle energy of a D-T fusion reaction. At initialization, we distribute the particles uniformly in their pitch angle. Particles are launched from flux surfaces equally spaced in effective minor radius. Within each flux surface, the number of launched particles is proportional to an alpha particle birth profile rate, $\lambda_{\mathrm{birth}}(\rho) = n_D n_T \langle \sigma v \rangle_T$. For the analysis presented in this section, the required kinetic profiles are taken from the chosen physics design point (Point A) introduced in Section 2.3. On each flux surface, particles are launched following a volumetric uniform distribution (i.e., they are initialized proportionally to the Jacobian $\sqrt{g}$ derived from the VMEC equilibrium). The particles are considered lost if they cross the $s = 1$ boundary of the plasma.

Sub-figure (a) in Fig. 5 shows the fraction of lost energetic particles at different volume-averaged plasma β values as a function of time after their birth, as obtained from SIMPLE. At the optimized design point, with $\langle \beta \rangle_V = 3.0\%$, the cumulative lost fraction of fusion-born fast particles after 100 ms is approximately 0.7%. This time frame of 100 ms is a representative value for the alpha-electron momentum exchange time at realistic temperatures and densities in stellarator reactors. Note that the configuration was optimized for the full pressure operating point $\langle \beta \rangle_V = 3.0\%$;

As a comparison, we perform a single collisional alpha particle confinement calculation at $\beta = 3\%$ using the Monte-Carlo code ANTS [63]. The code integrates drift orbits in 3D space using a grid-based interpolation of all field-related quantities required. The calculation includes pitch-angle scattering and slowing down from collisions with the thermal background plasma, assumed to consist of electrons, deuterons and tritons. As before, particles are considered lost in this simulation if they cross the $s = 1$ boundary of the VMEC equilibrium. ANTS allows for differentiation between particle and energy losses. Loss fractions of both the energy and the particle loss of the fast particle population as a function of the slowing down time are shown in sub-figure (b) of Fig. 5. We find total alpha particle energy losses at around 0.8% with this higher level of fidelity analysis, consistent with the values obtained with SIMPLE.

Ultimately, the confinement of fast particles is constrained not only by power balance considerations, since fast particles need to be confined to reheat the plasma, but also by the heat load induced by these particles on the first wall. To estimate the magnitude of that heat load, we calculate the lost power from energetic particles as a function of the volume-averaged plasma β, as shown in Fig. 6. As the plasma β increases from vacuum to the desired target design point, the lost fusion power remains below approximately 10 MW. Following the methodology outlined in [110], we estimate the peak heat load on the wall using conservative assumptions, such as assuming no energy loss of fast particles during their slowing-down period. By applying a heuristic peaking factor of 320, which was determined in [110] for a HELIAS-5 configuration, the estimated peak heat load on the wall at the target design point for this study is about $1.4\,\mathrm{MW\,m^{-2}}$. This value is of the same order of magnitude as the photon wall loads, demonstrated later in this paper, in Section 2.7, and is therefore in line with the technological limits of a solid first wall.

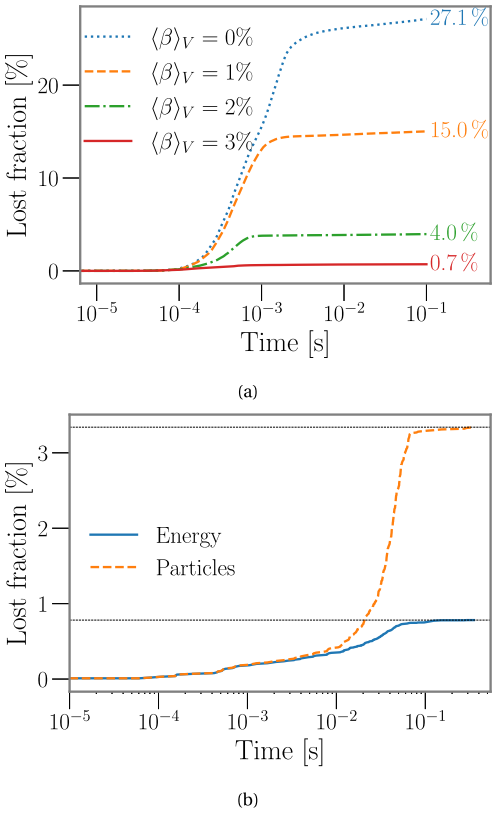

Fig. 5. (a): Lost fraction of energetic particles initialized from a realistic birth profile at different volume-averaged plasma β, as obtained with SIMPLE using collision-less simulations. (b): Results of collisional slowing-down simulations using code ANTS at $\langle\beta\rangle_V = 3\%$ using a realistic alpha particle birth profile. .

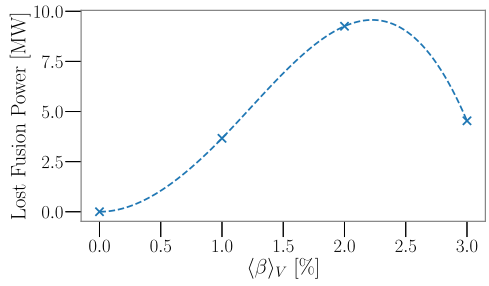

Fig. 6. Lost fusion power from energetic particles initialized from a realistic birth profile at different volume-averaged plasma β as obtained from the VMEC free boundary equilibrium and using the SIMPLE code assuming collisionless fast particle trajectories according to realistic birth profiles of a priori plasma background profiles.

Neoclassical transport. Neoclassical parallel and radial transport must be minimized for QI configurations to be reactor-relevant. Fig. 7 shows the mono-energetic neoclassical radial transport coefficient as a function of the mono-energetic collisionality $\nu_* = \frac{R_0 \nu}{\iota v}$ for the SQuID configuration used here and for the standard configuration of W7-X. Both configurations have been scaled to the same plasma minor radius and the same axis-averaged magnetic field strength.

The figure illustrates that with a finite radial electric field, the proposed configuration exhibits about one order of magnitude lower radial neoclassical transport coefficients compared to W7-X. Furthermore, the transport coefficients remain of a similar size across different plasma β values. This highlights the resiliency of the equilibrium properties against diamagnetic effects. The neoclassical mono-energetic transport coefficients have been evaluated with the SFINCS code [107] on the VMEC free-boundary equilibrium.

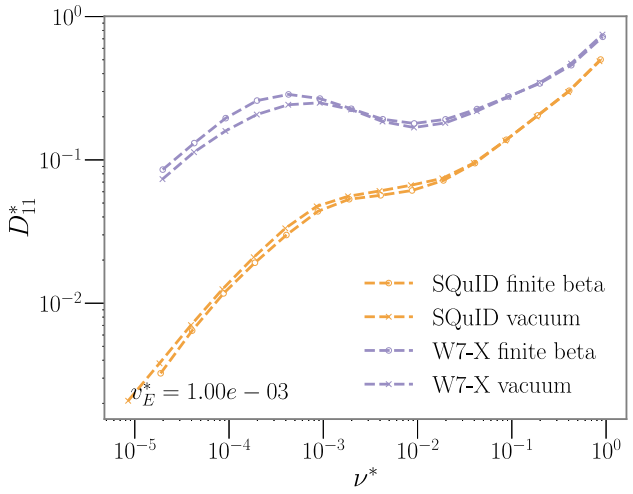

Fig. 7. Neoclassical radial transport coefficients $D_{11}^{\star}$ as a function of collisionality $\nu\star$, in vacuum and at the target volume-averaged plasma $\langle\beta\rangle_V = 3.0\%$. The normalized radial electric field, $\upsilon_E^* = \frac{E_r}{\upsilon B_0}$ was set to 10^{-3}. υ is the particle velocity and B_0 is the flux-surface averaged magnetic field strength. Configurations are evaluated at mid-radius (i.e., $\rho = 0.5$). The computation was performed with SFINCS using free-boundary VMEC equilibria.

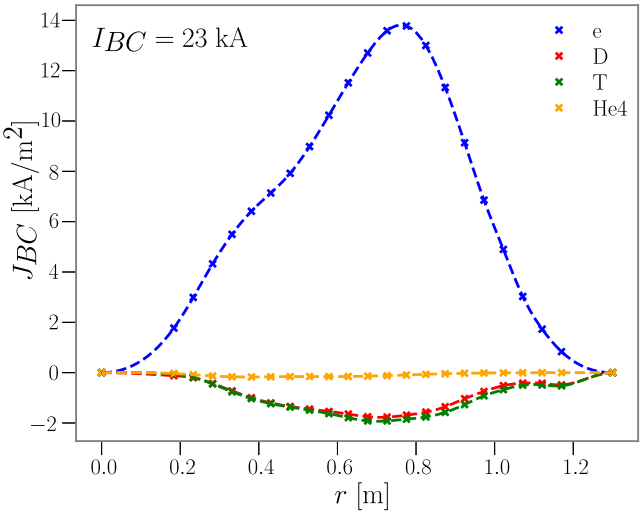

Fig. 8. The bootstrap current density profile J_{BC} for the different species at the design target of $\langle\beta\rangle_V = 3.0\%$ as a function of the plasma minor radius r. The integrated toroidal current is $I_{\mathrm{BC}} \simeq 23\,\mathrm{kA}$.

The bootstrap current is another important neoclassical quantity. Fig. 8 shows the magnitude of the bootstrap current density for different species. Species profiles are computed using the 0.5-D models that will be introduced in Section 2.3. The radial electric field value for this computation was evaluated with the NTSS code [111] in the ion-root case (see). For these profiles, the integrated bootstrap current is approximately $I_{\mathrm{BC}} \simeq 23\,\mathrm{kA}$. For most practical purposes, a toroidal current with this magnitude can be neglected, as it would result in a shift of the rotational transform at the edge of only 0.5% .

Ideal-MHD stability. In QI configurations with low net toroidal current, MHD current-driven modes are expected to be negligible. However, it is important to consider the stability of pressure-driven ideal-MHD modes. In this analysis, local ideal-MHD stability criteria are employed to evaluate the configuration's stability against ballooning and interchange modes.

To this end, we examine the configuration's stability against the ideal-MHD interchange mode using the Mercier criterion [112–115].

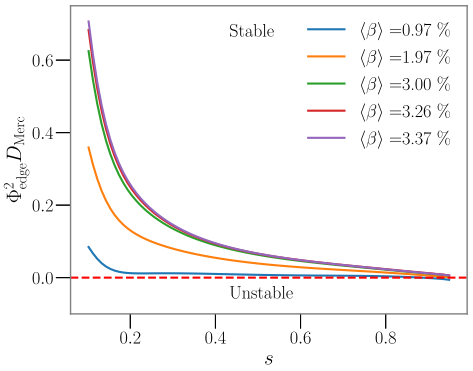

Fig. 9. The normalized Mercier criterion $\Phi_{\mathrm{edge}}^2 D_{\mathrm{Merc}}$ as a function of the normalized toroidal flux s for different volume-averaged plasma β. A positive value of the Mercier criterion suggests a stable configuration with respect to the high-mode number ideal-MHD interchange mode, whereas a negative value suggests an unstable configuration. The proposed configuration features a positive Mercier criterion over the whole plasma volume up to and beyond the target volume-averaged β value of $\langle\beta\rangle_V = 3.0\%$. The red dashed line represents the boundary of stability. The evaluation was performed using the free boundary VMEC equilibrium.

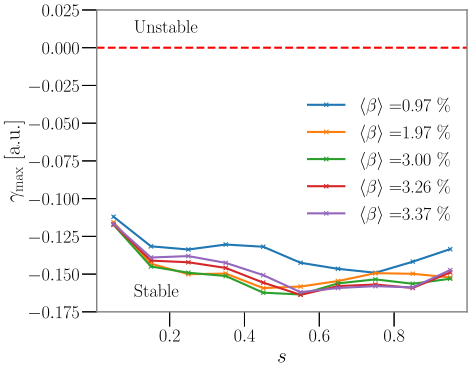

Fig. 10. Highest growth rate of the ideal-MHD infinite-n ballooning mode across all evaluated field lines on a flux surface γ_{max}, plotted as a function of the normalized toroidal flux s for different volume-averaged plasma β. The growth rates are evaluated with the COBRAVMEC code. Negative growth rates indicate a stable configuration, positive growth rates indicate an unstable configuration. The red dashed line represents the boundary of stability. The evaluation was performed using the free boundary VMEC equilibrium.

Appendix D describes the adopted definition of the Mercier criterion. A positive value of the Mercier criterion is a necessary (but not sufficient) condition for a stable configuration at that specific radial location, whereas a negative value suggests potential instability.

Fig. 9 presents the Mercier criterion as a function of normalized toroidal flux for various volume-averaged plasma β values, as evaluated with VMEC using the free-boundary equilibrium. The results show positive values across the entire plasma profile up to and beyond the target β of $\langle\beta\rangle_V = 3.0\%$ (see Fig. 9).

Additionally, we employ the COBRAVMEC code [109], which computes the local (on a field line) growth rates of ideal-MHD infinite-n ballooning modes using the VMEC free-boundary equilibrium solution. Fig. 10 shows the highest growth rate across all evaluated field lines on a flux surface as a function of normalized toroidal flux for various volume-averaged plasma β values. For each flux surface, growth rates are computed on 100 field lines with starting locations uniformly distributed across the poloidal and toroidal directions. We find that the free-boundary plasma configuration is stable against ideal-MHD infinite-n ballooning modes throughout the entire plasma domain up to and beyond the design volume-averaged plasma $\langle\beta\rangle_V = 3\%$.

Equilibrium resiliency with respect to finite-β effects. Optimized QI configurations tend to be particularly resilient against varying plasma

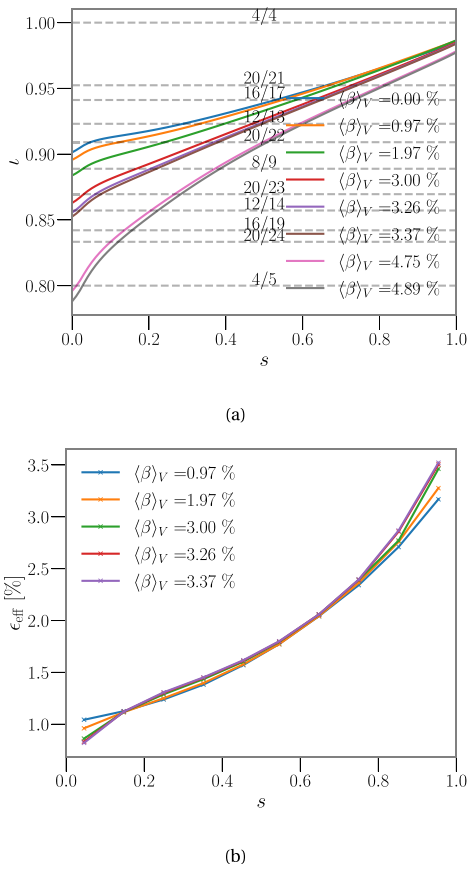

Fig. 11. Profiles of the rotational transform ι (a) and the effective helical ripple, ϵ_{eff}, (b), at varying volume-averaged plasma β as a function of the normalized toroidal flux s. In the rotational transform profile plot, resonant values between $\frac{4}{5}$ and $\frac{4}{4}$ up to the 5th order are shown with dashed horizontal lines. All equilibria use the same pressure profile shape. The evaluation was performed using the free boundary VMEC equilibrium.

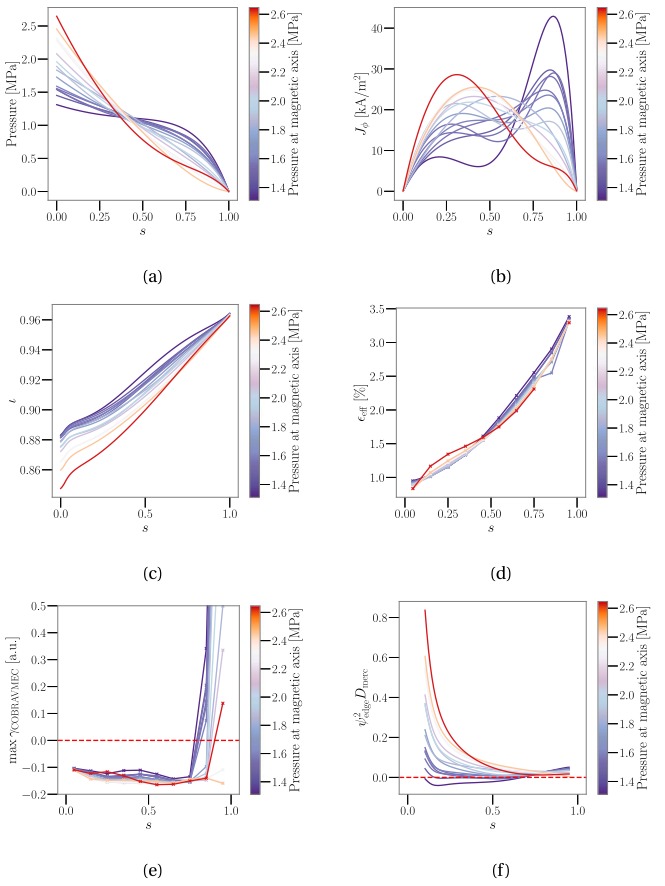

Fig. 12. Sensitivity analysis of equilibrium properties for different pressure and (derived) toroidal current density profiles. pressure profile $p(s)$ (a), toroidal current density profile $J_\phi(s)$ (b), rotational transform profile $\iota(s)$ (c), epsilon effective profile $\epsilon_{\text{eff}}(s)$ (d), maximum growth rate on a flux surface for the ideal-MHD infinite-n ballooning mode profile $\gamma_{\text{COBRAVMEC}}$ (e), and the normalized Mercier criterion profile $\psi^2_{\text{edge}} D_{\text{Merc}}(s)$ (f). All as a function of the normalized toroidal flux s. In case of the ideal-MHD criteria, a red, dashed, line represents the stability boundary. All profiles are color-coded based on their pressure value at the axis. All equilibria have the same stored integrated energy and the same integrated toroidal current.

profiles. In order to validate this point for the present SQuID configuration, we analyze the resiliency of key metrics with respect to finite β and profile effects. We note that this analysis is rarely done in the literature, and configurations are often only optimized for one set of profile profiles. However, consistent with the spirit of this reactor study, we aim to address potential drawbacks of the Stellaris for reactor applications. We split the analysis in two parts: first, we investigate the resiliency with respect to changing plasma β for a fixed profile; second, we assess the contribution of the profile shape for a fixed volume-averaged plasma β. We take the corresponding a priori profile from the identified design point in Section 2.3, see Fig. 16, as the default pressure profile, then compute a VMEC equilibrium in free boundary for each pressure profile variation.

Fig. 11 presents the rotational transform profile and the epsilon effective, ϵ_{eff}, profiles at various volume-averaged plasma β values, two key metrics that are particularly sensitive to small changes in pressure profiles. Plasma β values up to and beyond the target design point are shown. The bootstrap current was neglected in this simulation. The rotational transform profile only crosses a resonance value (e.g. $\iota = 0.8$) at a high plasma β of $\langle\beta\rangle_V \simeq 4.75\%$. ϵ_{eff} captures the neoclassical transport in the $1/\nu$ regime with negligible electric field, which is the regime with the highest neoclassical heat flux. We find that the neoclassical transport properties in this regime are robust to the plasma β. Also, the edge rotational transform is found to be resilient against profile effects, which is particularly relevant in achieving a stable island chain for divertor applications.

In a second step, we analyze how changes in pressure and toroidal current profile shapes affect the equilibrium properties. As before, we evaluate the free boundary VMEC equilibrium using different pressure profiles sampled around the reference profile. Each modified profile is scaled to maintain the same total plasma energy as the original profile.

To simulate a realistic bootstrap current profile, we use a toroidal current profile based on the plasma pressure variation across flux surfaces,

$$J_{\text{tor}}(s) = J_\star s(1-s)\frac{dp}{ds} \,. \tag{1}$$

Given the connection between the pressure gradient and the bootstrap current, this expression represents a simple informed proxy for the expected current density profile. Additionally, we enforce the current density to vanish at the magnetic axis and at the LCFS.

While varying the profile shape, we scale $I_\star$ such that the integrated current stays constant at a (conservative) value of 100 kA.

Fig. 12 shows the sampled pressure profile and toroidal current density profiles. For each profile, the equilibrium properties were calculated using the VMEC code in the free-boundary mode. A total of 16 equilibria have been evaluated.

Almost all evaluated metrics reveal configuration resiliency with respect to profile shapes. Despite the different pressure and toroidal current profiles, the rotational transform remains far from critical

low-order rational values (e.g. 0.8). The ϵ_{eff} profile shows remarkable resiliency to profile variations.

The two chosen metrics for evaluating MHD stability suggest that the profile shape can affect the MHD stability of the configuration. Positive growth rates for the ideal-MHD infinite-n ballooning mode are observed near the plasma boundary, suggesting instability in that region for profiles with strong pressure gradients. In reality, such unstable profiles would likely flatten toward profiles that are MHD-stable.

It should be noted that even if linear ideal-MHD stability is violated for some regimes, the plasma can still be non-linearly MHD stable [116,117]. Modeling tools to test non-linear MHD stability are under development [118].

The resiliency of the equilibrium properties with respect to finite-beta effects have been optimized only indirectly via the QI optimization. Future optimized configurations could benefit from including additional metrics directly targeting the resiliency of MHD stability.

Flux surface quality. A set of nested surfaces is crucial for plasma confinement. In a stellarator field, nested flux surfaces are not guaranteed to exist. The electromagnetic coils need to be carefully optimized so that islands and stochastic regions are minimized within the confined volume. At the same time, reliable island divertor operation across different plasma β values requires maintaining both stable island location and size.

As plasma pressure increases, pressure-driven currents arise. These currents can significantly alter the vacuum field and 'break' flux surfaces. In most previously proposed stellarator configurations, pressure-driven currents caused significant stochasticity of flux surfaces in a substantial portion of the plasma volume [117,119–124]. This phenomenon has been observed both in simulation and in experimentation. It is therefore critical to assess whether a set of nested flux surfaces is preserved as the plasma β increases. The (indirect) minimization of the Shafranov shift should also lead to good flux surface quality at finite β. To assess the flux surface quality at finite β, the HINT-3D equilibrium code [125,126] has been employed. This code does not rely on the assumption of the existence of a nested set of flux surfaces, unlike VMEC, making it suitable to analyze configurations with potential pressure-driven modifications.

Fig. 13 shows that no signs of loss of confined plasma volume are visible as the plasma β increases. At $\beta_{\text{axis}} = 8.0\%$ (which corresponds to $\langle\beta\rangle_V \sim 3.0\%$), HINT-3D calculates a Shafranov shift of ~8.0%, which translates to a radial magnetic axis displacement of ≃0.1 m. Moreover, the 4/4-island chain is well-preserved, while the resonant islands themselves are moving slightly. The precise location and orientation of the resonant islands will need to be controlled with an array of correction coils, which are not further specified in this paper.

Ambipolar radial electric field. Stellaris utilizes tungsten coatings as the primary material for both the first wall and the divertor. Experiments with tungsten divertors have shown that tungsten atoms can be sputtered and potentially accumulate in the core of the plasma [127]. This accumulation can lead to a radiative collapse, causing operations to halt.

A negative radial electric field (i.e., an electric field pointing radially inwards) is known to be a significant factor in driving heavy impurities toward the core [128,129]. Conversely, a positive radial electric field can act to 'flush out' these heavy impurities.

Recent efforts have focused on developing methods to optimize stellarator configurations to achieve a positive electric field within the plasma core under reactor-relevant conditions (i.e., $T_e \simeq T_i$) [71,108,130]. The proposed configuration has been optimized similarly to the configurations presented in [71]. Therefore, it is expected to support a positive radial electric field in reactor-relevant conditions as well.

The 1-D NTSS [111] code has been used to compute the radial electric field profile from the ambipolarity condition. The mono-energetic neoclassical transport coefficients for the necessary particle fluxes are calculated using the SFINCS code [107]. Details of the simulation set-up can be found in [108].

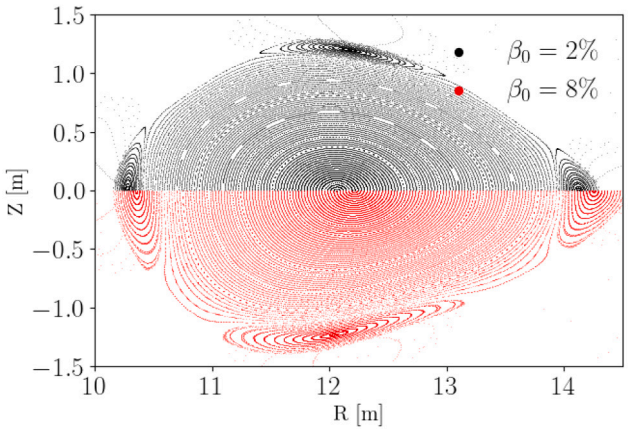

Fig. 13. Poincaré plots of the cross-section at $\varphi = \frac{\pi}{4}$ at 2% (black) and 8% (red) peak β values, corresponding to 1% and 4% volume averaged beta respectively. R is the cylindrical major radius (which is 0 in the center of the device) and Z is the Cartesian coordinate. The cross section is mirror symmetric at the $Z = 0$ plane. The analysis reveals preservation of good, nested flux surfaces as plasma β increases. The 4/4 island chain remains intact across all relevant β values. The equilibrium magnetic field was calculated using the HINT-3D equilibrium code [125,126].

The proposed configuration has the potential to support a positive radial electric field, as shown in Fig. 14. However, calculations based on the target design point and plasma profiles outlined in Section 2.3 predict a negative electric field. By adjusting the operational point toward a higher electron temperature ($T_{e,0} = 19.8\,\text{keV}$) and lower ion density ($n_{i,0} = 1.7 \cdot 10^{20}\text{m}^{-3}$), the configuration can achieve a positive radial electric field. This operational regime aligns with the 0-D analysis, but it comes at the expense of reduced fusion power output ($P_{\text{fusion}} = 860\,\text{MW}$).

While electron-root plasmas for reactor conditions are compelling to address impurity transport challenges, the radial location of the root transition is important: if it takes place at mid-radius, as in the case of Fig. 14 (orange line), it could potentially lead to an 'annulus' of impurity density accumulation at the region of the root transition, and therefore potentially to a radiative collapse of the plasma. Secondly, at the location of the root transition the radial electric field vanishes—in a stellarator, this is expected to lead to maximal neoclassical transport. Consequently, kinetic profiles might flatten at these locations. However, this may not be a significant drawback if the root transition were located near the plasma edge, where turbulence shearing effects may enable advanced confinement regimes. Future research will explore this possibility in more detail.

2.3. Physics performance

To determine possible operational temperatures and densities, we chose an integrated treatment of the power balance to assess the required auxiliary power and the fusion gain. This method is sometimes referred to as a '0.5D' treatment, as we calculate with an a priori assumed profile shape, but enforce the power balance by equating the integrated loss power with the integrated heating power, rather than solving a set of transport equations. In this paper, we will equivalently use the term '0D' for this method, for simplicity. High-fidelity profile predictions are still the subject of active research [132–134], and only preliminary calculations are available for the Stellaris design.

To obtain key parameters for the design point, we choose a simple parametrization of the ion density and electron temperature profiles:

$$T_e = T_{e,0}\left(1-\rho^2\right)^{\alpha_T}, \tag{2}$$

$$n_i = n_{i,0}\left(1-\rho^2\right)^{\alpha_n}, \tag{3}$$

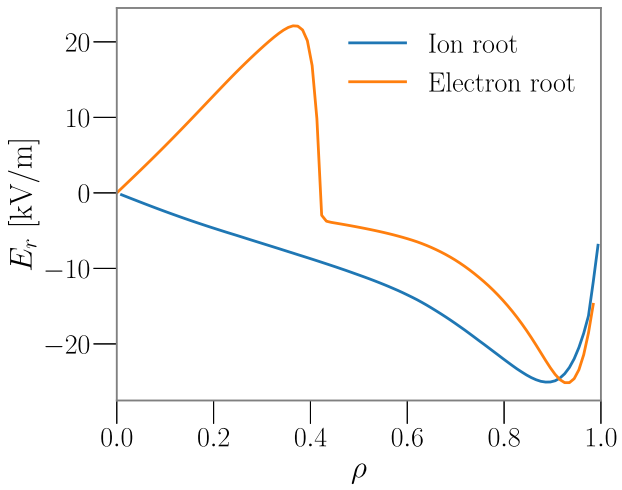

Fig. 14. Radial electric field profiles, E_r, evaluated with the NTSS code for two operational scenarios as a function of the normalized minor plasma radius ρ. The 'Ion-root' label refers to an E_r profile obtained from the 0-D design point labeled as 'A' in Section 2.3 (red dot in Fig. 15). This regime exhibits a purely negative electric field. 'Electron-root' refers to a profile obtained by operating at higher temperature and lower density, namely at $T_{e,0} = 19.8\,\mathrm{keV}$ and $n_{i,0} = 1.7 \cdot 10^{20}\ \mathrm{m}^{-3}$, which allows for a positive radial electric field. All profiles use a fixed ratio between electron and ion temperatures of $T_i/T_e = 0.95$.

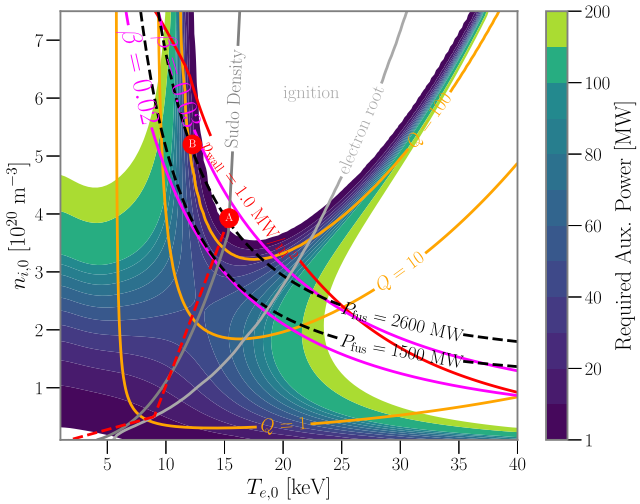

Fig. 15. POPCON plot illustrating the operational space of Stellaris. The y-axis represents the on-axis ion (fuel) density $n_{i,0} = n_{D,0} + n_{T,0}$ in units of $10^{20}\ \mathrm{m}^{-3}$, and the x-axis denotes the peak electron temperature $T_{e,0}$ in keV. The color gradient indicates the auxiliary power required, in MW, as shown by the color bar on the right. Contour lines depict various operational constraints and performance metrics including fusion power (P_{fus}), wall power load (p_{wall}), volume averaged plasma beta (β) and fusion gain (Q). The red circles marks specific operating points of interest at constant fusion power, labeled by 'A' and 'B'. The red dashed line shows a possible path to reach the design point from start-up with minimized auxiliary power. The dark gray line indicates the Sudo density limit [131]. The light gray line indicates above which temperature an 'electron root' appears in the center of the plasma at $T_i/T_e = 0.95$. White regions correspond to areas where the auxiliary power is beyond the color bar limits and would be either inaccessible (high T, low n or high n low T) or the plasma would ignite (high T, high n).

where $T_{e,0}$ and $n_{i,0}$ are varied to match the integrated power balance, and $\alpha_T = 1.2$ (a peaked profile shape) and $\alpha_n = 0.35$ (a flat profile shape) are fixed for this study, informed by density profiles observed in W7-X, e.g. [135]. These profiles are in line with the assumptions of previous stellarator reactor studies [12,136].

Appendix A describes the model fidelity used in this section. In summary, we use the fusion cross-section model from Bosch and Hale [137] for the fusion reaction rates. For line and continuum radiation, we use a priori assumed impurity fractions and calculate the cooling factors using the Aurora code [138], relying on the Atomic Data and Analysis Structure (ADAS) database [139]. Synchrotron radiation is modeled using the model described in [140]. We apply the ISS04 energy confinement time scaling law from [141], with a modification to replace the heating power by the ratio of plasma energy divided by the energy confinement time. Then, an averaged global energy confinement time is assumed: $\tau_E = \tau_E^{\mathrm{ISS04}}\left(T, B, a, A, \iota_{2/3}\right)$. Helium ash profiles are obtained using a fixed ratio of particle-to-energy confinement time. Fast particle pressures are modeled using the model of [142]. For the purpose of this analysis, we take a conservative value of the fast particle confinement of 95% and a fixed ion-to-electron temperature ratio of 0.95. An important assumption is a helium suppression factor f_{suppr}, heuristically reducing the amplitude of the resulting helium ash profile in the analysis. This factor accounts for the distinction between alpha particle birth location and thermalization location [110]. Assumed parameters are summarized in Table 4.

Table 4
Assumed parameters for the 0D studies in this section. f_{ren} refers to the proportionality factor of the ISS04 energy confinement time scaling, f_α measures how much of the alpha particle energy re-heats the plasma, $\tau^\star/\tau_i$ is the ratio between particle and energy confinement time (for all species), f_{suppr} is a heuristic factor used to model the suppression of helium ash, and n_W/n_e is the ratio between core tungsten density and central fuel density.

Variable	Assumption
f_{ren}	1.0
f_α	0.95
$\tau^\star/\tau_E$	8.0
f_{suppr}	0.5
n_W/n_i	10^{-5}

Fig. 15 shows a scan of the peak electron temperature $T_{e,0}$ and the peak ion density $n_{i,0}$, along with the required auxiliary power to support the operation point and relevant operational constraints, in a power-output-contour (POPCON) plot. Two chosen operation points are indicated with two red circles (labeled 'A' and 'B'). The red dashed line indicates a path to reach the operation point 'A' with minimal auxiliary heating power. According to the employed model, about 50 MW of auxiliary heating power would need to be installed to reach the desired operation point.

Table 5 summarizes machine and plasma parameters for both operation points. It is worth highlighting that the ratio of the volume-averaged electron density over the Sudo limit density [131], $\langle n_e \rangle_V / n_{\mathrm{Sudo}}$ at the chosen operation point 'B' is slightly greater than one. However, as suggested by recent research [143], the Sudo limit strongly depends on the impurity fraction in the edge, and higher fidelity models should be employed to calculate the density limit more accurately. Ultimately, although only the two operation points with the highest fusion power are shown here, the performance of the plasma equilibrium is sufficiently resilient at lower β values, indicating that all other operation points with $P_{\mathrm{aux}} < 50$ MW are likely feasible (e.g. an operation point with lower fusion power and lower fusion gain could be chosen, too, which would result in higher component lifetimes and easier burn-control). However, to keep the same output power of the machine, scaling should be done along lines of constant fusion power (dashed black lines in Fig. 15).

Profiles at the operation point 'A' are shown in Fig. 16. The profiles have a constant ratio between the minor plasma radius and the profile gradients when $T_{e,0}$ and $n_{i,0}$ are scaled (e.g. at $\rho = 0.6$ we find ratios of $a/L_T = 2.25$ and $a/L_n = 0.66$).

An important aspect to discuss is the control scheme required to support the suggested operation points. Compared to tokamaks, stellarators usually require very limited effort on control systems. In the

Table 5
Selected plasma and machine parameters for the two design points shown in Fig. 15. A-priori profiles are used according to Eq. (3). Ratios taken for $\tau^\star/\tau_E$ are assumptions. n_{O1} refers to the cut-off density of electron cyclotron resonance heating (ECRH) in the first ordinary (O1) mode. In further studies, until not otherwise stated, values for point A are taken. Point B would violate the 'Sudo- density limit' [131], but might still be feasible with sufficient plasma purity.

Description	Point A	Point B
Minor plasma radius [m]	1.3	1.3
Major plasma radius [m]	12.74	12.74
Axis averaged B_0 [T]	9.0	9.0
Aspect ratio [1]	9.8	9.8
Plasma volume [m^3]	425	425
Plasma surface area [m^2]	327	327
f_{ren} [1]	1.0	1.0
Vol av. Z_{eff} (core) [1]	1.20	1.21
Vol. av. beta [%]	2.76	2.81
Vol. av. el. density [10^{20} m^{-3}]	3.17	4.21
Peak helium ash density [10^{20} m^{-3}]	0.56	0.83
Peak el. density [10^{20} m^{-3}]	5.06	6.89
Peak D density [10^{20} m^{-3}]	1.96	2.60
Peak T density [10^{20} m^{-3}]	1.96	2.60
$n_{e,0}/n_{O1}$ [1]	0.64	0.87
$\langle n_e \rangle_V / n_{Sudo}$ [1]	1.00	1.55
Peak el. temperature [keV]	15.40	12.25
Peak ion temperature [keV]	14.63	11.64
Fusion gain [1]	∞	182
Aux. power at operation point [MW]	0	14.77
Fusion power [MW]	2700	2700
Peak fusion heating [MW/m^3]	5.51	6.02
P/S_{LCFS} (no edge radiation) [MW/m^2]	1.18	0.91
Total plasma energy [MJ]	504.65	533.14
Av. neutron wall power [MW/m^2]	2.87	2.87
Av. photon wall power [MW/m^2]	0.70	0.72
Peak triple product [$keVs/m^3$]	3.93×10^{21}	5.66×10^{21}
Confinement time [s]	1.46	1.99
Alpha slowing down time [ms]	43.76	23.75
Ratio $\tau^\star/\tau_E$ [1]	8.00	8.00
Tritium burn rate [g/day]	416.57	416.49
Rel. tungsten fraction core n_W/n_e [10^{-6}]	7.76	7.55

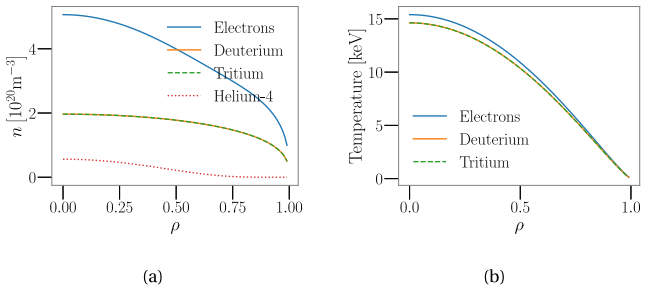

(a) (b)

Fig. 16. Steady-state density profiles (a) and temperature profiles (b) for the chosen design point (Point A) as a function of the normalized radius $\rho = r/a$. The shape of the profile corresponds to the analytical expression used in Eq. (3) for $\alpha_T = 1.2$ and $\alpha_n = 0.35$.

case of Stellaris, the requirements are reduced to achieving density control, detachment and edge radiation control, and potentially control of the edge island locations through an array of control coils. If the chosen design point is thermally unstable, an additional control scheme or confinement degradation scheme should be employed to achieve burn-control. While density control is widely adopted in current experimental fusion devices, resilient mechanisms for temperature control are not yet well-established, but are conceptually straightforward: plasma confinement degradation can be achieved by tuning coil currents or controlling the tritium fraction in the core. Alternatively, it may be possible to use electron-cyclotron-current-drive (ECCD)-induced confinement degradation [144]. We expect the temperature to be ultimately limited by temperature gradient-driven turbulence or electromagnetic turbulence, such as kinetic ballooning modes. However, no tools or workflows currently exist to predict limits with high confidence.

To contextualize the confinement time model utilized in this section, we compare the resulting profiles at the operation point against a higher fidelity transport simulation of the selected stellarator configuration. This simulation assumes that turbulent timescales are distinctly separated from those governing significant changes in the density and temperature profiles.

For this analysis, turbulent diffusivities are computed using flux-tube simulations with GENE [145] and then passed to the transport solver TANGO [146,147], similar to the approach described in [148]. The transport equations are solved with fixed density profiles, and the electron and ion temperature values are constrained by a Dirichlet boundary condition set to 4.2 and 5.2 keV respectively at $\rho = 0.8$, informed by the assumed kinetic profiles of Fig. 16 at this location. The GENE simulations are conducted at the flux-tube with field-line label $\alpha = 0$, specifically at $\rho \in \{0.1, 0.4, 0.6, 0.8\}$.

To reduce any thermal runaway effects and allow for a more direct comparison of the resulting profiles, we set the power source in TANGO fix to the fusion heating profile expected at the 0.5 D design point. We distribute this heating 80% to the electrons and 20% to the ions, following [149]. Note that by choosing fixed fusion heating profiles, the resulting profiles will change, while the heating sources are not updated. The purpose is not a fully integrated, fully consistent temperature profile simulation, but instead a qualitative comparison to determine whether the assumed temperature gradients can be supported by full electrostatic turbulence. For this reason, other radiation losses, such as Bremsstrahlung, were neglected as a heat sink for the electrons. In order to obtain the profiles, an iterative loop is established between the heat fluxes obtained with GENE and the transport solver TANGO, following a methodology similar to that in [148,150]. The equilibrium is treated as fixed and is not updated within this simulation workflow. It is worth noting that if electromagnetic effects were included, one might expect stabilization of turbulence levels, leading to lower stiffness—provided that the system remains below the threshold for kinetic ballooning instability. We also remark that the effect of the neoclassical $E \times B$ shear is not included in this simulation. Recent studies show that even moderate neoclassical $E \times B$ shear in W7-X can change turbulence levels significantly [151].

Fig. 17 shows the resulting temperature profiles for the given assumptions. We find that the GENE+TANGO results indicate that peak temperature values of the 0.5 D profiles are supportable by electrostatic turbulence level within the used model fidelity, when making favorable assumptions of the edge temperature value. However, the simulations demonstrate high sensitivity to the assumption of the edge temperature, which again highlights the importance of coupling core- and edge-transport simulations for first-principle profile prediction simulations in stellarators.

On high confinement regimes in stellarators. Before concluding this section, we put the assumptions taken on confinement quality into perspective: significant uncertainties still exist in predicting the maximum achievable density and temperatures of a stellarator dominated by turbulent transport. keVs

Experimentally, a wide range of confinement properties has been observed in both W7-X and W7-AS. In W7-X, confinement times deviate significantly between 'ion-temperature clamping' experiments [65] and higher performance experiments in quasi-steady state after pellet injections [75]. In W7-AS, several articles report on high-confinement (H-Mode) in different forms [47,152,153] with significantly reduced transport levels.

It has been hypothesized that the ratio of heating power over plasma boundary surface area, P/S, is decisive for achieving the transition from low- to high-confinement, as seen in tokamaks [32,154]. In ASDEX-Upgrade (AUG), within $2 < \bar{n}_{19} < 6$, the P/S threshold value to access H-mode is $P/S \simeq 0.07\,MW/m^2$. Instead, W7-X has only reached

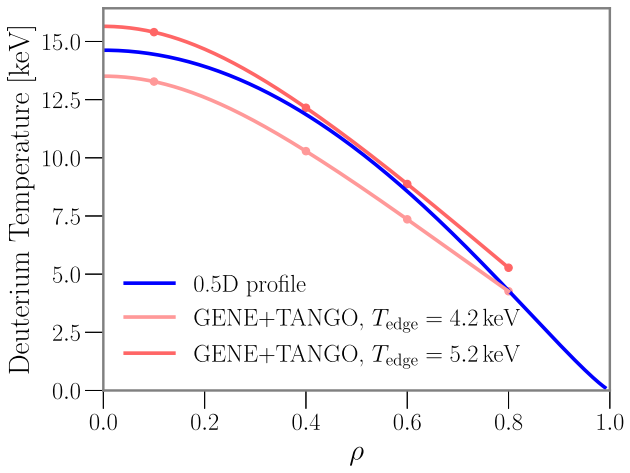

Fig. 17. Comparison of the 0.5 D deuterium temperature profile and results of two electrostatic GENE+TANGO simulations with different assumptions on the boundary value for the temperature at $\rho = 0.8$. Fixed density profiles and fixed heating power were assumed and were taken from Design Point A from Table 5. All radiative losses were neglected for the GENE+TANGO simulations.

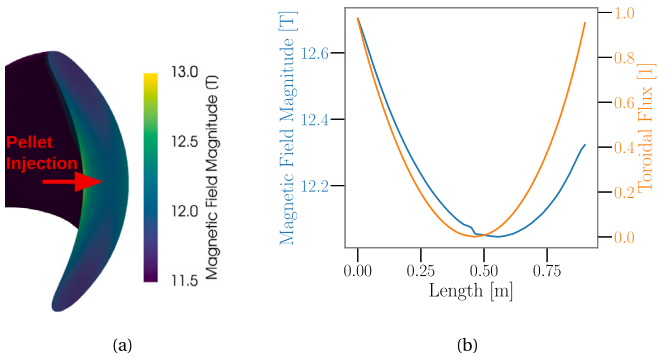

Fig. 18. (a): the pellet injection location, chosen in the $\varphi = 0$ plane (the bean-shaped plane). (b): corresponding plot of the magnetic field magnitude and the toroidal flux over a straight line in the bean-shaped plane located at $Z = 0$ and $\varphi = 0$, where Z is the Cartesian coordinate and *phi* is the cylindrical toroidal angle.

a maximum value of $P/S \simeq 0.02\,\mathrm{MW/m^2}$ [32]. For the design point in this paper, P/S is on the order of 1.18 $\mathrm{MW/m^2}$, significantly higher than the values measured in W7-X and AUG, even when accounting for respective magnetic field and density dependencies [154]. This suggests that, if there indeed exists a P/S threshold above which H-mode behavior occurs, the chosen physics design point of Stellaris may need to be corrected to account for confinement enhancement due to H-mode. In that case, resilient operation in an electron-root regime would ensure low impurity retention, addressing a common issue with many tokamak H-mode regimes. This point alone would justify the need for an intermediate-step device on the path toward a stellarator power plant, to determine whether H-mode physics follows analogous patterns as in tokamaks.

Isotope effects are another potential confinement-enhancing effect not typically covered in the ISS04 confinement time scaling laws. While this effect is not significantly observed in the neoclassically dominated heliotron LHD [155,156], it could still be relevant in optimized stellarators where confinement is ultimately limited by turbulence, as is the case with W7-X and the Stellaris concept. Related multi-machine regression fits in tokamaks suggest a decrease of turbulence levels for deuterium-tritium plasmas compared to pure hydrogen plasmas [157], and initial first-principle studies seem to support those findings [158]. Future deuterium campaigns in W7-X will shed more light on whether such an effect could be exploited in future stellarator power plant designs.

2.4. Fueling & density profile control

As indicated by W7-X experiments, density profile control is a highly promising mechanism to reliably suppress ITG turbulence [74,75,135,159,160]. The required density steepening can be achieved by either (a) increasing the core density by means of fueling (with cryogenic pellets or using neutral beam injection) or leveraging turbulent particle pinches [49,161,162], or (b) decreasing the edge density, for example using boronization [163], efficient edge pumping, or active boron powder injection [164]. An overview of density profile induced enhancements of plasma performance in W7-X is given in [135].

A stellarator reactor would greatly benefit from the possibility of externally controlling the steepening of density gradients. As no reliable predictive capability is yet available for turbulent particle pinches, we suggest density profile control for Stellaris via both core fueling with cryogenic pellets and edge fueling via gas puffing.

While the technology of pellet injectors is well-established and has been demonstrated in various experiments [165–170], the pellet deposition profiles cannot yet be fully simulated predicatively, and first simulations are just becoming available [171]. From these simulations, it is understood that the plasmoid drift effect that enables central fueling is strongest if the pellet injection takes place from a high-field region of the machine. Experimental studies show less pronounced sensitivities of the injection path to high- and low-field side [172]. Other control parameters, such as pellet sizes and injection speeds, are relatively inefficient to achieve central fueling.

We therefore propose the installation of a high-frequency pellet injector on the inboard side of the machine (e.g. in the bean-shaped plane of the stellarator plasma), where the distance in real space between the outermost plasma layer and the center is the smallest. Fig. 18 offers a visualization of the injection location in the bean shaped plane. Launching the pellet from a high-field region of the machine maximizes the plasmoid drift effects according to current understanding [171], potentially enhancing central fuel deposition. In the concept presented in this paper, the space in the high-field side bean plane is densely filled with structural material, posing a challenge for installing a pellet port. However, the port opening can be as small as 10 mm in diameter, as the cryogenic pellets are usually only a few millimeters wide. Dedicated studies are needed to determine the port opening that maximizes central fueling efficiency.

Gas puffing is used in almost all tokamak and stellarator experiments, and is an established method for plasma startup and edge fueling. Further research is needed, both theoretically and on experimental devices, to determine how the penetration of gas fueling via the plasma edge is expected to vary in large and high-density stellarators, where neutral particles may be unable to reach the confinement region. Analogous challenges exist for high-field, high-density tokamaks, where gas fueling is considered a control variable. Given uncertainties regarding gas penetration through the edge, we consider high-speed pellet injectors to be an important necessity for Stellaris.

2.5. Heating

There are different schemes available for heating fusion plasmas, of which the most promising are:

- Ion Cyclotron Resonance Heating (ICRH) [173–175], which requires installing antennas within the plasma vessel, resulting in antenna straps being in contact with the plasma—and therefore usually needing to be protected by highly conducting Faraday shield bars. With such a heating scheme, sputtering naturally occurs at the antenna, resulting in a significant impurity source for the core plasma. Additionally, the effect of strong, unshielded neutron irradiation on the antennas must be considered;

- Lower Hybrid Heating (LHH) [176,177], which also needs launchers that are close to the plasma;
- Neutral Beam Injection (NBI) is seen as difficult for reactor applications due to large port requirements, which cause problems with tritium breeding performance and free neutron streaming [178]. The negative ion NBI apparatus reaching MeV energies for reactor applications also poses major challenges for economic viability of the reactor, due to large capital costs. Wall-plug efficiencies of NBI systems typically remain below 30% [179];
- Electron Cyclotron Resonance Heating (ECRH), which features high levels of theoretical understanding at both an engineering and physics level. Reactor-relevant ECRH technology was demonstrated by W7-X [180–183] and ECRH systems will also be implemented in ITER [184] and DTT [185–187] in addition to being conceptualized for EU-DEMO [188,189]. While W7-X uses a quasi-optical transmission in air, DTT and DEMO will use evacuated quasi-optical transmission systems. ITER, on the other hand, will make use of overmoded waveguides. ECRH offers particularly a high technological readiness level for reactor applications;
- Other heating schemes, such as Transit Time Magnetic Pumping [190] and Alfvén Wave Heating [191–194], have been investigated experimentally, but have not received widespread acceptance and are not considered in more detail here.

Due to the above arguments and wide acceptance for reactor applications [188,189], we have selected ECRH as the primary heating method for Stellaris. The microwaves used for this technology are generated by a set of MW-class microwave sources that can be installed far away from the torus hall and can be guided through a system of actively cooled mirrors (as in W7-X, DTT and DEMO) or waveguides (as in ITER) toward the injection port. Such a concept is highly attractive, as the complexity of the heating system can be mostly decoupled from that of the torus building.

Gyrotrons are the only known microwave sources capable of providing the necessary MW-class output power as continuous waves [195–197]. Hence, gyrotrons are used in all large-scale magnetic confinement fusion devices that use ECRH.

For ITER, the gyrotron efficiency is expected to be 50% [184], leveraging beam energy recuperation via a depressed collector [198]. As of today, most gyrotron designs use Single-stage Depressed Collectors (SDCs). In the future, Multi-stage Depressed Collectors might increase the gyrotron efficiency to above 60% [199–202], making it an attractive heating solution even for steady-state applications in non-ignited plasma scenarios.

While W7-X now uses a gyrotron class of 1.0 MW and 1.5 MW operating at 140 GHz [203], ITER will operate with 170 GHz gyrotrons [204]. For future high-field machines to be heated via ECRH, it is necessary to demonstrate efficient operation of 240 GHz high-power gyrotrons. The technological development of gyrotrons is constantly progressing toward higher power and higher frequencies [200,205–207], ultimately enabling higher magnetic fields and more economical operation.

For the heating scheme of Stellaris, we propose using the first ordinary (O1) mode as the default scheme, noting that it has been well-studied for ITER [208]. To ensure that high-density plasmas can be heated, we choose the location of ports such that the first extraordinary (X1) mode can also be used. The X1 mode would permit heating far from the plasma cut-off density $n_{X_1}^{\mathrm{crit}}$, which is given by the constraint

$$n_e < n_{X_1}^{\mathrm{crit}} = \frac{2\, m_e \epsilon_0}{e^2} \omega_{\mathrm{gyro}}^2, \tag{4}$$

where n_e is the electron density, m_e is the electron mass, e is the elementary charge and ω_{gyro} is the local electron gyro-frequency. Although not yet experimentally investigated in stellarators, X1 mode heating is well-studied in tokamaks [209,210]. A requirement for X1 mode heating is a port design that allows a beamline with a monotonically decaying magnetic field strength to permit wave propagation. It is worth noting that X1 mode heating from a high-field region would heat the high-energy tail of the electron distribution function. Further study is needed to determine how this would impact plasma performance.

The injection beam path for the proposed device is illustrated in Fig. 19, showing an access point on the inboard side of the device. This unusual placement of an ECRH port not only enables the injection of the ECRH via a high-field region, but also frees access at the outboard side of the device, easing remote maintenance requirements. This is especially relevant for the remote maintenance concept of Stellaris, which uses sector splitting, as described in Section 2.11. It is worth noting that inboard access ports are particularly enabled by the high aspect ratio of Stellaris, and likely cannot be replicated in a comparable tokamak at lower aspect ratio.

A total of eight ports, each with 300 mm of diameter and a circular cross-section, are situated between the coils on the inboard side of every half module. Stress analyses (presented in Section 2.10) indicate that peak stresses around the port opening stay within design limits. The ECRH ports are installed with stellarator symmetry and can be adjusted to include a non-zero toroidal component. This set-up allows for the possibility of canceling small amounts of residual net toroidal currents by varying the relative ECRH power between the stellarator-symmetric ports, without requiring movable mirrors near the vessel or remote-steering launchers.

The port diameter was chosen to be as small as is reasonably possible in order to mitigate degradation of the tritium breeding performance of the blanket. Still, in reality, specific neutron shielding techniques would need to be employed, such as a labyrinth path to ensure that free neutron streaming through the port is minimized. Such considerations are outside the scope of this paper.

We anticipate Stellaris to operate with 50 MW of ECRH power in the plasma, necessitating approximately 6.25 MW of power to be transmitted through each port. To achieve this, we propose a configuration of 7 waveguides per port with outer diameters of 90 mm, fitting well within the 300 mm circular cross-section of the ports. Each waveguide would have an inner diameter of 60 mm, close to the design of the ECRH upper launchers for ITER, which have inner diameters of 50 mm [211]. Assuming a transmission loss of 10% between the gyrotron output and the launcher, each port would require seven 1 MW gyrotrons to deliver approximately 6.3 MW into the plasma. Greater margins could be achieved by increasing the output power per gyrotron, providing greater flexibility and robustness in achieving the desired power levels.

We remark that the high mirror ratio of QI stellarators allows for the use of a broad range of gyrotron frequencies, as the gyrofrequency scales linearly with the magnetic field strength. In this study, the magnetic field strength at the plasma boundary varies between 7.3 T and 13 T in the toroidal direction, corresponding to gyro-frequencies ranging from 200 GHz to 363 GHz. To minimize the required gyrotron frequencies, the chosen port location enables heating close to the toroidal low-field region of the stellarator, shown on the right-hand-side of Fig. 19. The potential effects of a resulting skewed distribution function of the electron population caused by the heating of trapped particles at the bottom of the magnetic mirror are yet to be investigated, but may be sufficiently small when the dominant heating term is the fusion heating at the operation point.

In order to validate the contention that wave absorption can take place with the given port set-up, we plot the local gyro- (electron cyclotron) frequency and the cut-off density along the beam-path in the plasma. Fig. 20 shows the cold resonance at $\langle\beta\rangle_V = 0\%$ and $\langle\beta\rangle_V = 2\%$ along the chosen beam-path in a cross section of the plasma, as well as the relativistically shifted broadening of the resonance. We chose a value of $\langle\beta\rangle_V = 2\%$ for the analysis here as the auxiliary heating is maximized between 1% and 2% volume averaged plasma β, as shown in earlier in Fig. 15. We model the relativistic shift on the gyro-frequency by employing a Maxwell-Jüttner distribution; the broadening experienced at the target design point (Point A from Table 5) is shown in Fig. 21. Fig. 21 visualizes this information again

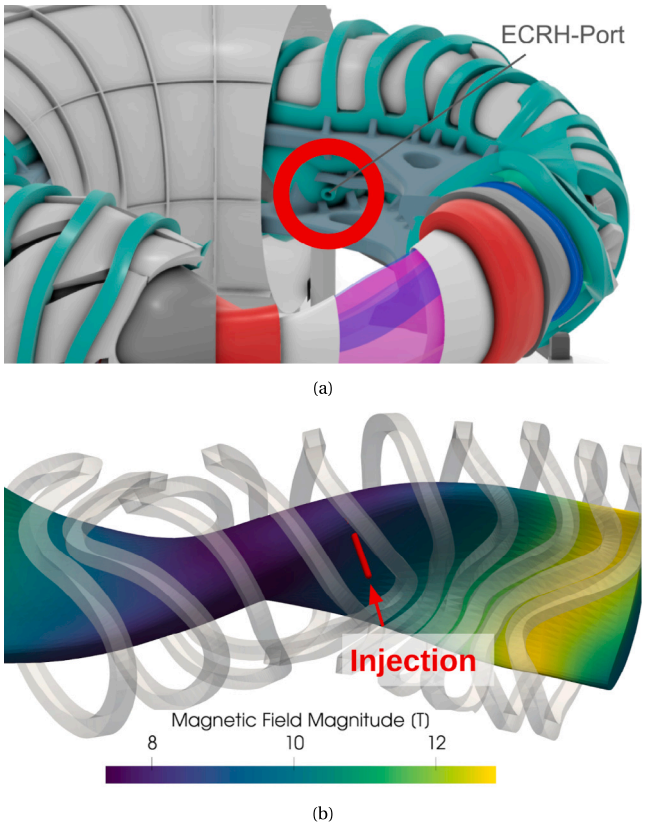

Fig. 19. Visualization of one of the chosen port locations for the X1 heating scheme. (a) Opening in the inboard support structure that allows for high field side injection to allow X1 wave propagation. (b) Visualization of the field strength at the last closed flux surface and chosen high-field location of injection. Fig. 21 and Fig. 22 show relevant quantities over the beam path, here shown in red.

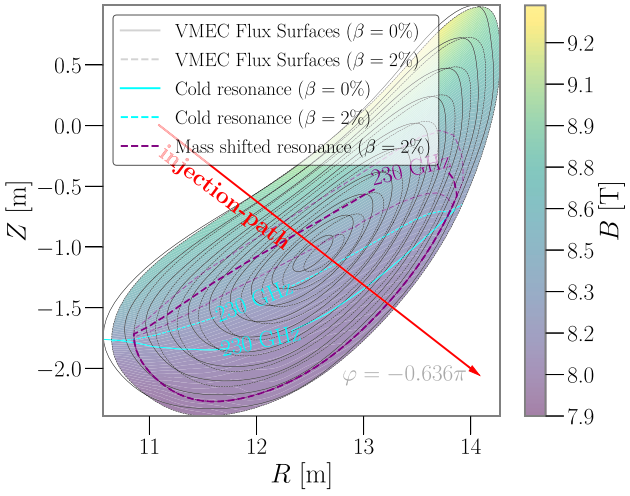

Fig. 20. Visualization of 230 GHz resonance frequencies for (volume-averaged) $\beta = 0\%$ and $\beta = 2\%$ in one of the 8 port locations that allow for ECRH heating. Here a toroidal cross section of $\varphi = -0.636\,\pi$ is plotted. The mass (relativistically) shifted frequency is shown with thin purple dashed lines via the 20% and 80% quantiles of the distribution function. The beam path corresponds to the one in Fig. 19. The plot shows that a gyrotron with frequencies in the range of 230 GHz is realistically able to heat the plasma through a range of β values.

in a 1D plot, showing the strictly monotonically decreasing gyrotron frequency required for X1-mode heating. Based on this analysis, a set

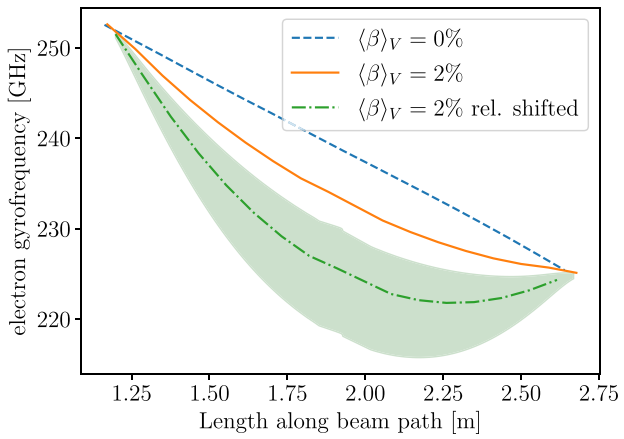

Fig. 21. Electron gyrofrequency at different plasma β values along the for the chosen ECRH port as a function of distance along the beam path. The diamagnetic effect of the plasma β leads to a reduction of the field and thus a reduction of the gyro-frequency. In this picture, the ECRH microwaves would be injected from the left. Relativistic mass shift and Doppler broadening lead to a smear-out of the gyro-frequency at a given spatial location along the beamline, here visualized with 20% and 80% quantiles of the distribution function. Corresponding normalized toroidal fluxes and the critical densities are shown in Fig. 22.

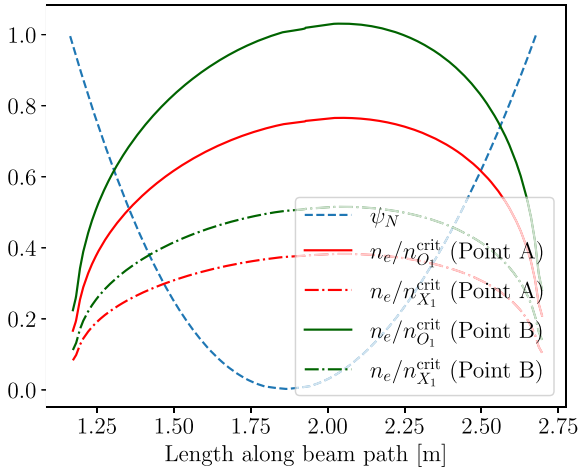

Fig. 22. Normalized toroidal flux (blue dashed) and electron density ratios for heating assessments, shown as a function of distance along the chosen beam path (same abscissa as in Fig. 21). The y-axis is a numerical value and shared between the curves. Green solid line: ratio of electron density over the O1 cut-off density at $\langle\beta\rangle_V = 2\%$, showcasing that the cut-off density is reached near the origin for 'operation point B' shown in Fig. 15; the red solid line shows the same for 'operation point A'. Green/red dotted–dashed line: the ratio of electron density over the X1 cut-off density at $\langle\beta\rangle_V = 2\%$, staying well below the cut-off density for both 'operation point A' and 'operation point B'.

of gyrotrons operating at frequencies around 230–240 GHz is capable of effectively heating the plasma across a range of β values, achieving relatively central deposition. For applications in which precise central heating is necessary, frequency-tunable gyrotrons could be employed to fine-tune the deposition location, ensuring optimal heating conditions.

As the local cut-off density for finite wave propagation in a stellarator varies as a function of the toroidal angle, we analyze the local density in comparison to the O1 and X1 mode cut-off densities along the chosen beam path, the two suggested heating scenarios. Fig. 22 illustrates that for the default design point (Point A) (as defined in Table 5), O1 mode heating appears feasible, as the local plasma density remains below the O1 cut-off density. However, for the high-density design point (Point B), the local plasma density exceeds the O1 cut-off, making O1 heating impractical. In this scenario, only X1 mode heating

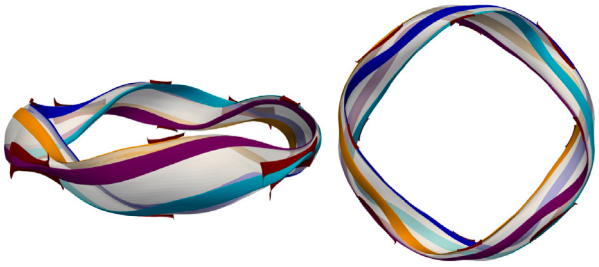

Fig. 23. Visualization of edge islands (colored tubes) together with the LCFS of the plasma boundary in vacuum (semi-transparent) in side and top view. Dark red plates show the discrete target plates of the island divertor as used for the analysis in this section.

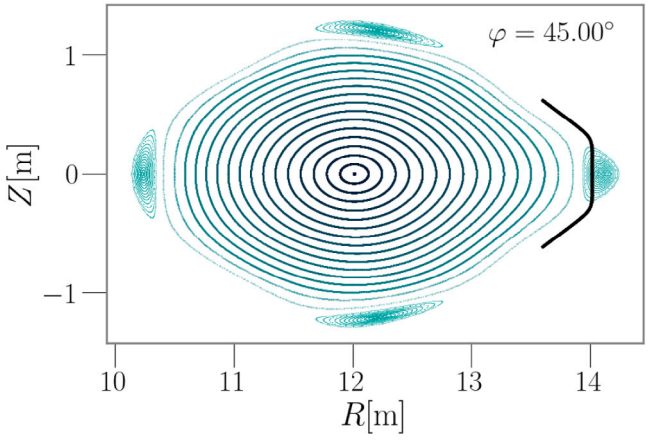

Fig. 24. Visualization of target plates (black) in the cross section at toroidal angle of $\varphi = 45°$, superposed with a Poincaré plot of the vacuum field. R is the cylindrical major radius (which is 0 in the center of the device) and Z is the Cartesian coordinate.

remains viable, as it allows for effective heating despite higher plasma densities due to its higher cut-off density.

2.6. The island divertor

QI stellarators, through their minimization of parallel plasma currents, allow for several stable X-points induced by deliberately placed magnetic islands at the plasma edge. The island divertor concept is an attractive candidate for a stellarator reactor due to its ease of access to detached conditions [41], its observed large wetted areas [38], and its comparably high technological readiness level, compared to other stellarator divertor concepts. Compared to tokamaks, stellarators with an island divertor usually feature very large connection lengths [39], which broaden strike lines on divertor plates due to the effect of cross-field transport over long physical distances [39]. While stellarators at reactor scale can have connection lengths in the range of kilometers, typical tokamak values range between 5 and 50 m for comparable machines [212].

The island divertor has been well studied in W7-X [37,42,213], although the W7-X open geometry has been found to provide insufficient neutral gas compression for effective pumping and density control. For Stellaris, we propose using a shape-optimized tungsten-based island divertor that operates with strong detachment in steady-state. This section describes initial efforts toward such a design.

For an island divertor to function effectively, it is crucial to sufficiently suppress the bootstrap current to prevent significant changes in the rotational transform at the plasma edge. Such changes could shift the location of the magnetic islands relative to the installed divertor plates, potentially preventing the desired intersection between the islands and the target plates. Keeping the resonant island structures intact ensures that the magnetic islands consistently intersect the divertor target plates at the intended locations. As shown in Fig. 8, the total bootstrap current for the stellarator design is calculated to be approximately 23 kA. This low value supports the use of resonant islands at the edge to create the required X-points, as the edge rotational transform is only calculated to change by 0.5% from vacuum conditions to the equilibrium where the steady-state bootstrap current is achieved.

Fig. 13 shows that the stellarator concept presented in this paper offers the desired magnetic island chain at the edge across a wide range of plasma β values, from start-up (where no kinetic pressure is present in the stellarator) to the final plasma β (where the islands are slightly larger, but still preserved). This feature is necessary for installing a set of divertor plates at the edge that cross the islands.

To meet the functional requirements of a divertor solution, the system must efficiently exhaust particles while managing the heat fluxes that impact material surfaces. Additionally, the divertor must support robust tritium recycling and effectively remove helium ash. A number of these issues are currently being addressed within a design effort to upgrade the Wendelstein 7-X divertor, including tungsten-based plasma-facing components and enhanced geometrical features for improved neutral gas pumping efficiency [214].

In this paper, we focus primarily on demonstrating the feasibility of placing a set of target plates that intersect the 4/4 island chain, with an emphasis on the thermal aspects of the divertor design. Other critical aspects of the Stellaris divertor – such as recycling efficiency, ash removal, neutral gas compression, and erosion rates – are acknowledged, but left for further exploration in subsequent studies.

The divertor plates proposed for Stellaris are optimized to limit heat loads by following a two-step design approach, as outlined in [215]. In the first step, the plates are strategically positioned and adjusted to ensure that a significant portion of the power crossing the Scrape-Off Layer (SOL) is captured by the plates. The second step involves optimizing the length of the plates to ensure that the heat loads remain below the desired flux limits. This approach aims to minimize the divertor plate area, while ensuring that heat flux constraints are met.

A smaller divertor area is beneficial because it reduces the absorption of neutrons that are crucial for tritium breeding in the breeding blanket, a topic further explored in Section 2.8. The location of the target plates is illustrated in Fig. 23, showing a 3D visualization of their placement, and in Fig. 24, where we display a cross section at $\varphi = 45°$. Unlike typical tokamak designs [212] and similar to the design of the W7-X divertor [216], the selected divertor plates are toroidally discontinuous.

To model the resulting heat flux, we utilize the code `EMC3-Lite` [217]. The physics model employed by `EMC3-Lite` is based on an anisotropic heat diffusion model along a set of field lines within a 3D geometry, described by the equation

$$\frac{\kappa_e}{n_e}\nabla_\parallel^2 T + \chi_\perp \nabla_\perp^2 T = 0, \tag{5}$$

where the Bohm sheath boundary condition [218,219] is applied as

$$Q_{\parallel,\mathrm{PFC}} = -\kappa_e \nabla_\parallel T_{\mathrm{PFC}} = n c_s \gamma T_{\mathrm{PFC}}. \tag{6}$$

In this context, $\kappa_e = \kappa_{e0} T^{5/2}$ represents the Spitzer heat conductivity [220,221], with κ_{e0} being a constant and T the temperature (assumed identical for ions and electrons). Here, n_e denotes the electron density, and $\chi_\perp$ is the perpendicular thermal diffusivity, which accounts for turbulent transport. $Q_{\parallel,\mathrm{PFC}}$ represents the parallel heat flux (expressed as power per unit area) on the Plasma Facing Components (PFCs), while T_{PFC} refers to the plasma temperature at the PFCs. The ion sound speed, c_s, is given by $\sqrt{2k_B T/m_i}$, where k_B is the Boltzmann constant and m_i is the ion mass, with γ being the sheath transmission factor.

A key advantage of the `EMC3-Lite` model compared to commonly employed diffusive field line tracing (DFLT) methods [222–227] is

its ability to simulate bidirectional heat transport, allowing heat to travel both forward and backward along the magnetic field line at any point. In contrast, DFLT lacks this capability, which can result in underestimations of heat loads in magnetically shaded regions, as demonstrated in [228].

Compared to higher fidelity models, such as the EMC3-EIRENE code [229], EMC3-Lite does not solve the Braginskii-like fluid equations for the edge plasma or include a kinetic neutral model. EMC3-EIRENE has shown both qualitative and quantitative agreement with experimental data from W7-X [230,231]. Although currently not ideal for automated PFC design due to its computational cost and complexity, and therefore not utilized in this study, EMC3-EIRENE would be highly suitable for high fidelity modeling of devices like Stellaris, and can be harnessed to better characterize detachment under reactor conditions, further advancing the divertor concept. Despite its simplified approach, the EMC3-Lite model is expected to sufficiently cover the physics relevant to the distribution of non-radiated heat exhaust over the target plates [217,228]

An important factor in calculating the heat loads on divertor plates is understanding the extent of edge radiation and the degree of detachment within the scrape-off layer (SOL). In this analysis, we assume that the reactor operates under conditions of strong edge radiation and nearly complete detachment, ensuring most of the heat flux is radiated away in the last layers of the confined plasma and within the SOL itself.

Achieving stable detachment is critical, as it protects the divertor target plates from excessive heat loads. To facilitate this, an active control system, likely involving a noble gas puff system, will be required. Stable detachment and control mechanisms in island divertors have already been demonstrated in the W7-X stellarator [42,232], as well as radiative edge cooling techniques [233,234]. Both of these mechanisms are expected to undergo further scientific investigation in W7-X.

For this analysis, we assume that 90% of the net heating power in the plasma core is radiated before reaching the divertor region. This means that, for a total of 500 MW of heating power, the divertor must be capable of handling 50 MW. To accurately estimate the heat loads on divertor plates, two additional hyperparameters are critical: (1) the ratio of parallel to perpendicular transport, which depends on temperature and density, and (2) the perpendicular diffusion coefficient $\chi_\perp$, representing turbulent cross-field transport. There remains considerable uncertainty in estimating appropriate values of these parameters. For the purpose of analyzing peak heat loads, we consider a lower bound of $T_{\mathrm{LCFS}} = 100\,\mathrm{eV}$ with $\chi_\perp = 3\,\mathrm{m^2\,s^{-1}}$ and an upper bound of $T_{\mathrm{LCFS}} = 200\,\mathrm{eV}$ with $\chi_\perp = 1\,\mathrm{m^2\,s^{-1}}$, where temperature values at the Last Closed Flux Surface (LCFS) are taken as proxies to estimate the ratio of parallel to perpendicular transport. Obtaining more accurate estimates for these quantities should be a focus of future studies. The density was set to $n_{\mathrm{LCFS}} = 10^{19}\ \mathrm{m^{-3}}$. Under these assumptions, our simulations indicate that the divertor plates in Fig. 23 capture 97% of the non-radiated heat for the lower parallel/perpendicular transport parameters ($T_{\mathrm{LCFS}} = 100\,\mathrm{eV}$ and $\chi_\perp = 3\,\mathrm{m^2\,s^{-1}}$) and 99% for the higher transport parameters ($T_{\mathrm{LCFS}} = 200\,\mathrm{eV}$ and $\chi_\perp = 1\,\mathrm{m^2\,s^{-1}}$). The corresponding peak heat loads are simulated at $5\,\mathrm{MW\,m^{-2}}$ and $9.5\,\mathrm{MW\,m^{-2}}$, respectively. In the scenario with higher perpendicular transport, the divertor wetted area is broader, and therefore heat loads on the targets are lower, but more of the heat is also reaching the first wall. The simulated heat fluxes for the main target elements under the most pessimistic assumptions are illustrated in Fig. 25. These values remain below $10\,\mathrm{MW\,m^{-2}}$, which is a commonly applied threshold for steady-state heat fluxes in divertor designs [235]. This strike-line width is simulated to about 200 mm.

It is crucial to emphasize that the obtained values strongly hinge on the assumed radiated power fraction, underscoring the importance of robust detachment control in the divertor region, and potentially additional edge radiation control using deliberate impurity seeding. Complexity of the design and simulations increases when considering transient heat flux limits. Such situations could arise during the start-up phase of Stellaris, before full detachment is achieved, or in operational

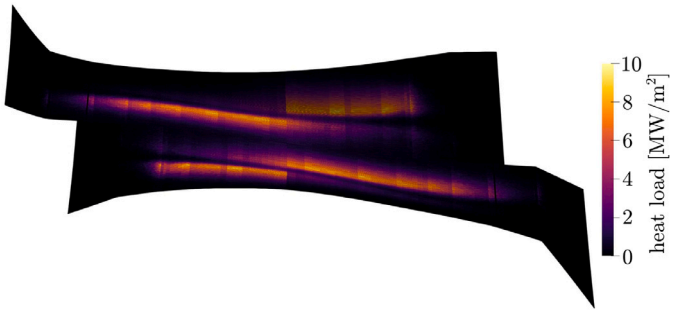

Fig. 25. Simulated heat load patterns on the proposed divertor targets in the 45° plane, using the code EMC3-Lite, for $T_{\mathrm{LCFS}} = 200\,\mathrm{eV}$ and $\chi_\perp = 1\,\mathrm{m^2\,s^{-1}}$. The width of the strike line is approximately 200 mm.

scenarios where detachment control is momentarily lost due to a failure mode. For instance, it has been reported that in W7-X the divertor plates experience significant heat loads during the initial seconds of a discharge, before detachment is established and the heat loads on the target plates effectively drop to zero [236]. As with the incorporation of additional functional requirements into the divertor design, evaluating transient heat loads is beyond the scope of this study and should be addressed in the future.

In conclusion, this analysis serves as an initial step toward the development of a reactor-relevant island divertor concept for Stellaris. While this study primarily focused on the thermal management aspect of the divertor, the optimization of PFC arrangements to fulfill all exhaust requirements is an ongoing effort within the fusion community. We note that it is crucial to transfer the insights and lessons learned from the W7-X divertor to a new, fully integrated, reactor-relevant divertor design. Such a dedicated effort will be instrumental in bridging the gap between experimental findings and power plant applications.

2.7. First wall

In the previous section, we considered the importance of strong edge radiation to distribute a significant portion of the heat load across the first wall before charged particle heat fluxes reach the target divertor plates. The adopted operational scenario anticipates that approximately 90% of the heat flux is radiated in the outer layers of the plasma and the SOL. In this section, we examine wall cooling capabilities. We adopt a more conservative approach, assuming that 100% of the heating power is radiated through core and edge radiation. This assumption is specifically geared toward estimating the maximum heat load on the first wall, which is critical for understanding peak temperature conditions.

Our focus here is on a three-dimensional Finite Element thermal analysis. We do not delve into the subject of erosion by neutral particles, which tends to be less significant in stellarators than in tokamaks, provided that the SOL thickness is adequately large [237]. In the Stellaris design, we ensure that the first wall is positioned at a minimum distance of 100 mm from the plasma. This spacing is expected to mitigate erosion rates, allowing us to limit the present investigation to thermal effects.

For broader context, the most comprehensive overview of the first wall challenges in DEMO can be found in [238], though a comparable in-depth study for stellarators is yet to be published. This gap in the literature underscores the need for dedicated research into the unique first wall challenges posed by stellarator designs like Stellaris. In order to estimate the peak temperatures, we employ the same first wall geometry used in other sections of this paper, i.e., for divertor (Section 2.6) and neutronics (Section 2.8) simulations. The wall encloses the edge

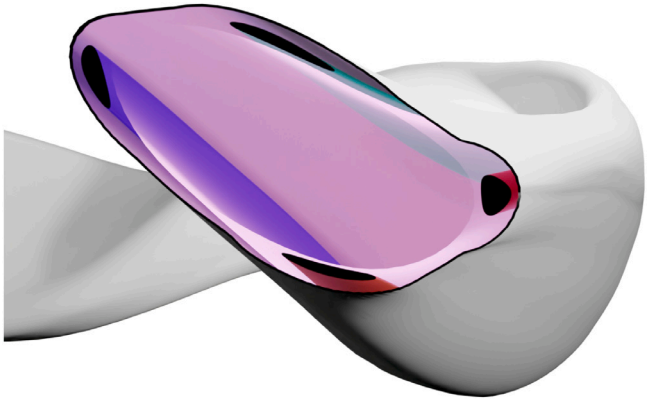

Fig. 26. Visualization of the chosen first wall geometry, which leaves sufficient space for the divertor target plates crossing the magnetic islands, shown here in different colors for qualitative distinction. The chosen first wall geometry is the same across all analyses in this paper.

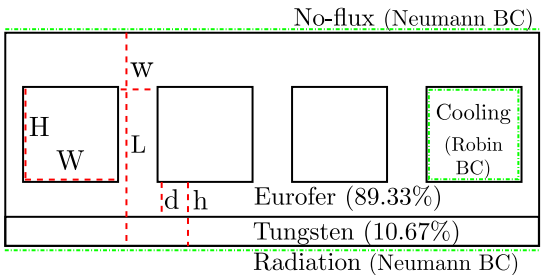

Fig. 27. Cross section at constant toroidal angle through the first wall design as used for the FEM analysis in this section. Actual dimensions are $H = 12\,\text{mm}$, $W = 12\,\text{mm}$, $w = 5\,\text{mm}$, $L = 27\,\text{mm}$, $d = 3\,\text{mm}$, $h = 5\,\text{mm}$. Channel cross sections are square in our study for ease of modeling, but would be rounded in the actual wall. The wall section in our model is a single strip wrapping around the poloidal direction, mainly due to the fact that we have not fixed a tile design yet. This is not fully realistic, but it allows us to perform a reliable analysis. The sector is defined by the toroidal angle and the channels follow the parametrization of the surface, meaning they are not all the same length, but they are all around one meter long.

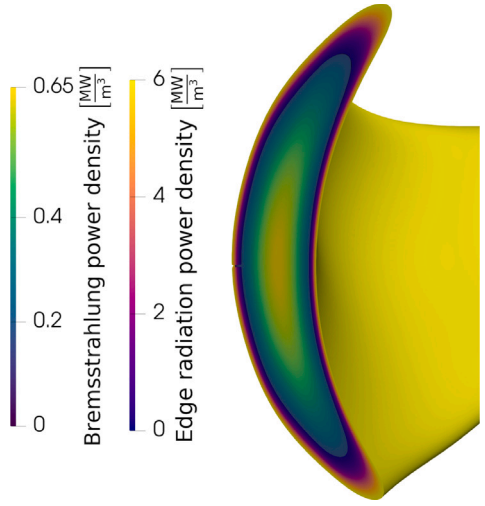

Fig. 28. Cross section through the plasma illustrating emission from both the plasma core (green color legend) and edge (red color legend).

magnetic islands that are used for the island divertor solution, and is shaped to maximize the breeder volume outside of it (see Fig. 26 for a visualization of the geometry).

While multiple first wall concepts for stellarators are currently being explored, we select a straightforward approach for this analysis: a solid EUROFER97 wall with a 2 mm-thick tungsten armor serving as the plasma-facing surface. This choice is justified by the low loss of fast particles, as demonstrated in Fig. 6, which permits the use of a solid wall rather than more complex designs—such as those requiring liquid walls to handle highly localized heat loads due to significant losses of fusion-born α particles.

The first wall in this design incorporates several rectangular cooling channels running in the toroidal direction, utilizing pressurized helium gas as the primary coolant. We simulate helium at 8 MPa with an inlet temperature of 350 °C; the helium's outlet temperature is computed dynamically and is below 370 °C. Here *inlet temperature* refers to the temperature at the *front* of the first wall; similarly, the *outlet temperature* is the temperature of the helium after flowing along the plasma-facing side. Our study does not take into account the other two sides of the first wall module. The conceptual dimensions of this first wall design are illustrated in Fig. 27. Although an interlayer between the EUROFER97 and tungsten layers will be included in the actual design, it is omitted from our model due to its negligible impact on the overall temperature distribution.

It is important to note that the feasibility of this manufacturing process will be the focus of subsequent studies. However, we emphasize that the helium-cooled lithium lead (HCLL) blanket design serves as a precedent, indicating the potential practicality of our proposed approach.

In estimating the first wall temperature, we begin by calculating the heat loads consistent with the design point outlined in Section 2.3 and 100% radiation of the heating power. The radiation source is divided into two parts: core radiation and edge radiation.

First, core radiation is computed using the '0.5D-profiles' introduced in Section 2.3, considering contributions from Bremsstrahlung, tungsten impurity radiation, and synchrotron radiation. For edge radiation, we model a Gaussian profile centered around $\rho = 1$ (discarding any emission at $\rho > 1$) to represent line radiation from partially ionized impurities, such as Argon or Krypton [239]. These impurities would need to be injected into the plasma to enable significant radiation of the core heating power, facilitating a radiating edge and achieving divertor detachment. Fig. 28 illustrates the combined emission region in one cross section of the plasma from both core and edge as assumed and calculated for the first wall power estimates.

The first wall is also subjected to a volumetric heat load due to neutrons produced by fusion reactions in the plasma. We include this aspect in our model and simulations by incorporating the power density data presented in the later Section 2.8, visually represented in Fig. 37.

We determine the peak temperatures in the first wall using a two-step process. First, to calculate the heat load on the first wall, we follow the method suggested in [240], where the first wall power density, p_W, is obtained by integrating over a source volume V:

$$p_W = \int_V \frac{\phi_s}{4\pi\|\vec{r}_W - \vec{r}_S\|^2} \left(\vec{n} \cdot \frac{\vec{r}_W - \vec{r}_S}{\|\vec{r}_W - \vec{r}_S\|}\right) dV. \tag{7}$$

Here, ϕ_s is the local emission; $\vec{r}_S$ is the position vector of the source; $\vec{r}_W$ is the position vector to the wall; and $\vec{n}$ is the normal vector of the wall.

To implement this method, a regularization is necessary. We choose to set the heat flux from a volume element on a surface area to zero if the distance exceeds a characteristic length for the machine; in this case, 8 m, since for the chosen configuration, this is a clear upper bound on the distance between two points that have a direct line of sight to each other. When computing the integral in Eq. (7) numerically, we set the integrand to zero for contributions that satisfy $\left(\vec{n} \cdot \frac{\vec{r}_W - \vec{r}_S}{\|\vec{r}_W - \vec{r}_S\|}\right) < 0$. We verified a posteriori that this algorithm works effectively, as the total emitted power from the LCFS and the total absorbed power by

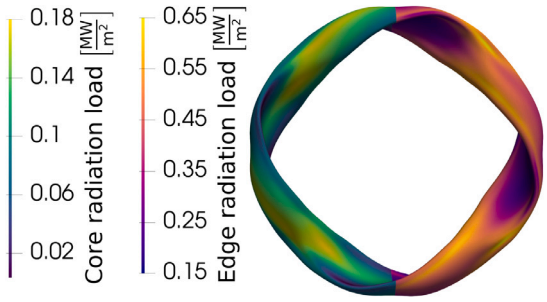

Fig. 29. Visualization of the calculated first wall heat loads, distinguished by source. The left-hand half shows the received core radiation, the right-hand half the received edge radiation. Strong deviations in the toroidal and poloidal direction are observed. The total power at the wall is the sum of both sources and its values span the range $0.18\,\mathrm{MW\,m^{-2}}$ to $0.77\,\mathrm{MW\,m^{-2}}$.

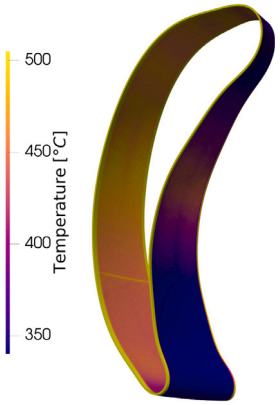

Fig. 30. Simulated temperature in a toroidal segment of the first wall, using the methods and parameters described in the text. With the current design, peak temperatures are simulated to stay below 500 °C and peak in the central module.

the first wall differ by only about 2%. The volume integral is carried out in VMEC coordinates [241], and the Jacobian determinant $\sqrt{g}$ is obtained directly from the VMEC code.

In the second step, we solve the heat equation as a Finite Element problem within a small toroidal section of the first wall. To obtain a conservative estimate, we select a section that includes the geometry points with the highest anticipated radiation load; the volumetric neutron load does not show significant enough variability to affect the results if we changed section. For simplicity, the analysis omits the divertor plates, recognizing that they could potentially shield some of the heat loads on the first wall. We also assume that all radiation is absorbed in the first layer of the wall, which we model as a Neumann boundary condition in the Finite Element analysis. Any reflection or black-body radiation effects of the first wall are neglected.

The method employed for this calculation is detailed in Appendix B. The power loading on the first wall, distinguished by source is shown in Fig. 29. The resulting temperature distribution for this design is shown in Fig. 30. With the given assumptions, the steady-state temperature remains below 500 °C—a design limit typically imposed for EUROFER97 steels [238]. We conclude that a helium-cooled first wall can be designed to withstand the heat fluxes anticipated for the high power density design point proposed in this study. We note that evaluating thermal stresses due to temperature asymmetries is beyond the scope of this study, and warrants further investigation.

2.8. Lithium blanket & neutron shield

In this section, we explore a potential breeding blanket and shield design for Stellaris. Research on stellarator breeding blankets in the literature addresses a range of topics, from balance of plant considerations [242] to detailed neutronics analyses [64,243–248] and evaluations of structural capabilities [249,250].

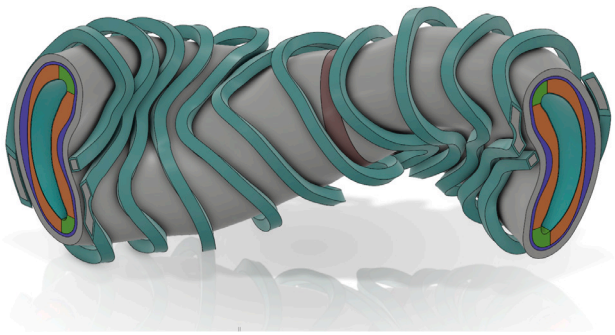

Fig. 31. The geometry used in the neutronics simulations. Light green is the first wall, orange is the homogenized breeding blanket, blue is the neutron shield, gray is the vacuum vessel and green are the divertor modules. Coils are shown in turquoise. The brown section shows the sector interface that will be introduced in Section 2.11.

Previous investigations into stellarator breeding blanket concepts have primarily focused on dual-cooled lithium-lead and helium-cooled pebble bed designs as potential breeders. These concepts aim to optimize both tritium breeding and structural integrity, balancing neutron economy with effective heat transfer and material endurance.

However, prior reactor studies for stellarators have consistently highlighted a critical challenge: the close proximity of the optimized stellarator coils to the plasma. This proximity has been shown to be insufficient to provide adequate neutron shielding, posing a significant risk to the integrity and longevity of the coils in realistic reactor settings [52,64]. Furthermore, the limited distance between the plasma and the coils has been identified as the primary constraint on overall machine size, directly influencing the feasibility of achieving a viable reactor configuration [12]. The Stellaris concept strategically addresses this challenge. By ensuring that the coils are positioned farther away from the plasma in relative terms, this design provides greater space for tritium breeding and neutron shielding, allowing the overall reactor size to be reduced. The blanket concept itself was chosen from different available options and finally adapted to match a set of requirements that is in line with the overall machine design.

In the current breeding blanket design, the primary tritium breeding material is a liquid lead-lithium (PbLi) eutectic alloy with 16 atomic percent lithium. This material serves a dual role as a neutron multiplier and tritium carrier. The liquid breeding material allows for drainage to ease remote maintenance operations. The breeding zone is actively cooled using water at pressurized water reactor (PWR) conditions, ensuring efficient thermal management. EUROFER97, a low-activation steel known for its structural integrity under fusion-relevant conditions, is selected as the structural material for the blanket [251]. The nuclear data cross sections for the materials are derived from the ENDF/B-VIII.0 library [252], with interpolations adjusted for material temperature. To further enhance neutron management, an In-vessel Neutron Shield (INS) composed primarily of tungsten-carbide (WC) is incorporated. This material not only serves as a neutron shield, but also functions as a neutron reflector, effectively increasing the backscatter to the blanket and boosting the tritium breeding ratio (TBR).

The Vacuum Vessel (VV) design is modeled after the EU DEMO project [253], utilizing SS316LN as the structural material. The design includes a neutron shield in the bulk cooling region, with a thickness reduced from the originally proposed 60 mm to 50 mm. Boron-carbide (BC) is chosen for the shield due to its superior absorption cross section in the thermal neutron range compared to WC.

Active cooling is essential for maintaining the structural integrity of the breeding blanket, as the chosen structural material, EUROFER97, has a maximum operating temperature limit of 550 °C [254]. The breeding blanket's composition is optimized for both thermal management and tritium breeding, consisting of 73.5% PbLi eutectic, 12.5% water,

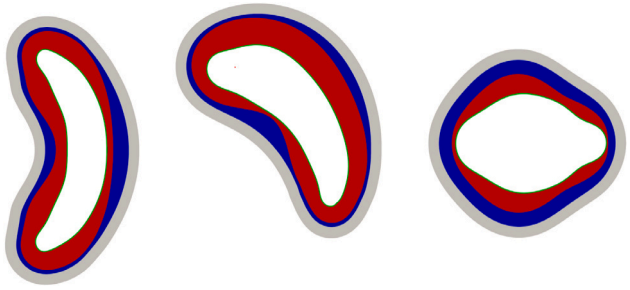

Fig. 32. Cross section visualization of the radial build at the $\varphi = 0$, $\varphi = \pi/8$ and $\varphi = \pi/4$ cross sections (where φ is the cylindrical toroidal angle). The thin green line is the first wall, red is the homogenized breeding blanket, blue is the shield, and white is the vacuum vessel. Note that the divertor is not included in this visualization.

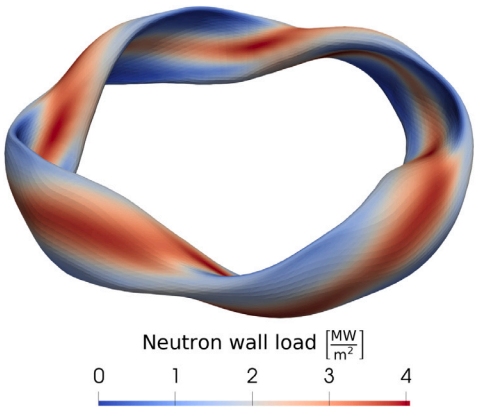

Fig. 33. The distribution of the neutron wall load on the first wall of Stellaris operating in full power, at 2700 MW fusion power.

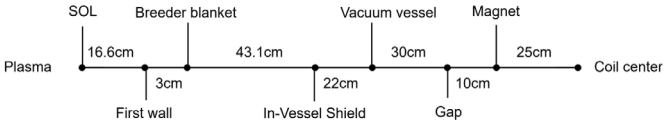

Fig. 34. Averaged component thicknesses and gaps of the radial build. Values are only approximate, as large variations in both toroidal and poloidal directions exist.

and 14% EUROFER97 by volume. This composition accounts for the segmentation effect in the structural budget, ensuring the blanket's performance and durability.

To achieve a tritium breeding ratio (TBR) above 1.05, considered sufficient to close the fusion fuel cycle [255], a lithium-6 enrichment level of 70 % has been chosen.

The decision to use a water-cooled breeding blanket simplifies the power plant's primary and secondary cycles, aligning them with those of a conventional PWR. The high water content in the blanket has a significant thermalization effect, which shifts the neutron spectrum toward thermal energies—increasing the reaction rate and improving tritium production. Additionally, the high heat capacity of water compared to gas cooling reduces the need for large cooling ports, which helps in optimizing the overall design.

The first wall, as described earlier, is proposed to be helium-cooled, while the breeding blanket utilizes water cooling. This necessitates the use of two distinct cooling loops. The choice of helium cooling in the first wall is driven by two main considerations. First, the lower pressure in the helium loop allows for a thinner first wall, enhancing thermal efficiency. Second, helium cooling offers greater resilience against critical heat flux events, which are particularly challenging to manage in high-pressure water cooling systems.

For the breeding blanket segmentation, one potential configuration is the single module segment (SMS) design [256]. In this configuration, each toroidal section of the reactor is split into poloidal segments approximately every meter. Each segment is supplied independently to ensure modularity and improve detectability of failures within a module. Within each segment, the manifold configuration directs helium through back manifolds located behind the neutron shield, routing it radially toward the first wall, while the breeding blanket's water cooling system is fed through separate manifolds and distributed poloidally.

This modular approach reduces the need for complex manifold systems at the back of the blanket, thereby creating more space for a sufficiently large INS. The simplified geometry of the SMS design not only facilitates maintenance but also enhances the overall efficiency of neutron shielding and tritium breeding, making it a compelling choice for the reactor's blanket configuration.

Given the varying plasma-to-coil distance across different poloidal and toroidal positions, we implement variable thicknesses for both the blanket and the shield. This design strategy enables the optimization of TBR while ensuring adequate neutron shielding at the cryogenic coils. For instance, the INS thickness at various toroidal angles is shown in Fig. 32, with a minimum thickness of 100 mm and a maximum thickness of 225 mm. Additionally, the averaged thicknesses for each layer of the radial build are illustrated in Fig. 34. To optimize the thickness of the INS, we use a simple one-dimensional exponential decay model for the fast neutron flux within the radial build, using two material fractions for INS and BB. In particular, we vary the shielding thickness, using a fixed first wall and outer shield surface, in order to minimize the neutron flux variation in a point-by-point fashion. The choices of materials for INS and BB are kept constant during this optimization.

In the following neutronics simulations, we employ the 3D neutron Monte-Carlo simulation code `OpenMC` [257,258], integrated with `DAGMC` [259] for efficient particle transport simulations. The `CAD-to-DAGMC` tool [260] was utilized to convert the detailed CAD geometry into a meshed representation suitable for the analysis. A comprehensive three-dimensional (3D) 90-degree reactor model is initialized, incorporating multiple material layers, each homogenized into a single `OpenMC` material for simplification. The reactor geometry used in the neutronics analysis is depicted in Fig. 31, which illustrates the various reactor layers, including the magnets described separately by their casings and winding packs. For the particle sources, we employ a neutron source function based on the plasma profiles introduced in Section 2.3, utilizing the nuclear reaction rates from [137]. The neutronics simulations presented in this section are consistent across both physics design Point A and Point B, as defined in Table 5, because the fusion power remains constant and the effects of plasma temperature on the neutron source distribution are neglected.

To approximate the neutron source, we use a monoenergetic source at 14.06 MeV, with the spatial distribution discretized into 30 radial points, 50 poloidal points, and 100 toroidal points. This source is then represented as multiple point sources in the `OpenMC` simulation environment. The resulting neutron wall load is shown in Fig. 33, using the method proposed in [240].

We proceed to analyze the chosen breeding blanket and shielding concept through five key evaluation steps:

- Tritium Breeding Ratio Analysis: We assess whether the design achieves sufficient tritium breeding using a multi-layer 3D model that includes separately homogenized materials for each layer.
- Power Multiplication: Due to endo- and exothermal nuclear reactions within the blanket, we estimate to which degree the total neutron power is amplified by the blanket, a critical value to estimate the commercial viability of a fusion power plant.
- Neutron Shielding for Superconductor Protection: We evaluate the effectiveness of neutron shielding in minimizing fast neutron flux into the superconducting coils—ensuring long operational

lifetimes for the device, as fast neutron fluences are measured to significantly degrade the performance of superconducting coils after $3 \times 10^{22}\,\mathrm{m}^{-2}$ [261]. The neutron fluence on the copper stabilizer should also be considered as the conductivity has been shown to reduce with neutron irradiation by 5% after a neutron fluence of $1.5{\times}10^{23}\,\mathrm{m}^{-2}$ [262]. One strategy to potentially address a conductivity decrease would be to make the copper stabilizer thicker to accommodate the anticipated decrease in conductivity.

- Neutron Shielding for Cryogenic Area Protection: We determine whether the neutron shielding sufficiently reduces nuclear heating in the cryogenic regions to acceptable levels, ensuring the integrity of the cryogenic components.
- Lifetime Estimation of Key Components: We estimate the operational lifetime of the main components of the machine, considering the neutron flux and the resulting material degradation over time.

Safety and activation calculations, as well as structural and thermal simulations, fall outside the scope of this analysis.

Tritium breeding ratio analysis. We performed a neutronics simulation using 15×10^6 particles per batch over 5 batches, tallying TBR, nuclear heating, and neutron flux. Periodic boundary conditions were applied at the $\varphi = 0$ and $\varphi = \pi/2$ surfaces, where φ represents the toroidal angle. No particle loss was observed during the simulation, ensuring accurate results.

The simulation was focused solely on neutron transport, with the nuclear heating tally assuming that secondary gamma power is deposited locally. The computed TBR, accounting for the remote maintenance solution discussed in Section 2.11 and a conceptual divertor model, is 1.1070 ± 0.0002. After considering a 3% reduction due to the heating ports, the final TBR stands at 1.074, which includes margins to account for uncertainties and potential incomplete models.

Power multiplication. Using the same 3D neutronic simulation that was employed for the TBR calculation, we also tallied the power multiplication within the blanket, which primarily results from exothermal (Li-6, n) reactions. From this analysis, we obtained a power multiplication factor of 1.2. The initial 2160 MW of neutron power produced by the reactor is thus amplified within the blanket to a nuclear power of approximately 2611 MW. This thermal power is what can be extracted from the blanket and shield systems, contributing to the overall energy balance of the power plant. Corresponding simulation results are shown in Fig. 37.

Neutron shielding for superconductor protection. To ensure sufficient statistical accuracy in the estimation of fast neutron fluxes in the volume of the superconducting magnets, we performed a dedicated simulation with a total of 2.5×10^9 Monte Carlo particles.

The resulting fast neutron flux ($E_n > 0.1\,\mathrm{MeV}$) at the magnets is illustrated in Fig. 36. The average fast neutron flux is estimated to be $1.8 \times 10^{13}\,1/\mathrm{m}^2/\mathrm{s}$. As the statistics of the Monte Carlo simulation even at 2.5×10^9 launched particles is particularly low, and assuming local shielding can be used in severely loaded sections, we consider the 99th quantile for the lifetime estimation of the coils due to fast neutron flux, which is about $9.5{\times}10^{13}\,1/\mathrm{m}^2/\mathrm{s}$. Estimating the allowable fluence for ReBCO superconductors (from degradation of the critical current density in the superconductor by fission neutrons [261]) as $3{\times}10^{22}\,1/\mathrm{m}^2$, the magnet system would have a lifetime of approximately 10 full power years at a fusion power of 2700 MW.

Additionally, the neutron spectra at the coils are presented in Fig. 35, providing further insight into the distribution of neutron energy levels impacting the superconducting magnets.

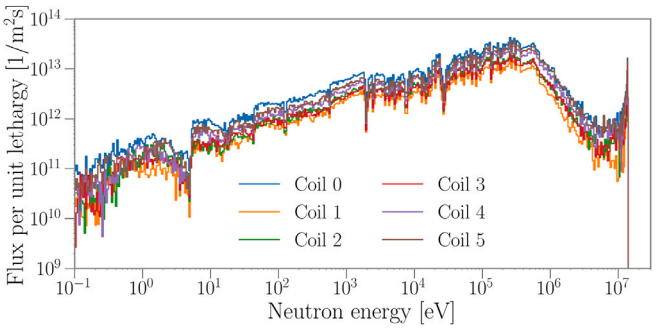

Fig. 35. Neutron flux per unit lethargy, as obtained from OpenMC with the set-up described in the text. The spectra describe the winding pack of all six coils independently at full power.

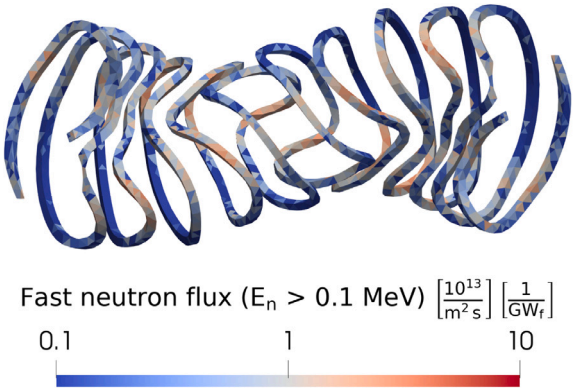

Fig. 36. Fast neutron flux, as obtained from OpenMC with the set-up described in the text. The figure shows the unstructured mesh tally on the magnet. The maximum neutron flux is $7.27 \times 10^{13}\,1/\mathrm{m}^2/\mathrm{s}/\mathrm{GW_f}$ (neutron flux normalized by GW fusion power), and the mean value is $6.6 \times 10^{12}\,1/\mathrm{m}^2/\mathrm{s}/\mathrm{GW_f}$.

Neutron shielding for cryogenic area protection. For the nuclear heating at the winding pack, we obtain an average value of $35.5\,\mathrm{W/m}^3$. This heat load will need to be managed by the cryo-plant of Stellaris and is in the order of the EU DEMO target, which is about $50\,\mathrm{W/m}^3$ peak nuclear heating [263].

However, it is important to note that the EU DEMO requirement is designed for a 4 K cryogenic environment, whereas the magnets in Stellaris are anticipated to be cooled to 20 K. Operating at this higher temperature offers an increase in efficiency of the cryogenic plant. Overall, maintaining an average nuclear heating below $50\,\mathrm{W/m}^3$ is considered an applicable reference for ensuring viable power plant efficiency, considering the parasitic power consumption by the cryo-plant.

It should also be noted that local differences in nuclear heating power density can lead to local temperature variations within the winding pack, which again can affect quench behavior. However, these temperature differences are highly dependent on the detailed cooling design within the winding pack and a respective analysis is left for further studies.

Lifetime estimation of key components. To estimate the operational lifetime of key reactor components, we calculate the Displacements-Per-Atom (DPA) in regions experiencing the highest neutron flux, specifically the first wall and the divertor.

Neutron damage was tallied using OpenMC via the '444 Microscopic Cross-Section Type (MT) reaction' for iron isotopes in the first wall and copper isotopes in the divertor. DPA values were evaluated using two models: the NRT model [264] and the more recently developed ARC model [265].

The ARC model, which has shown good agreement with molecular dynamics simulations, particularly at higher energies [266], provides

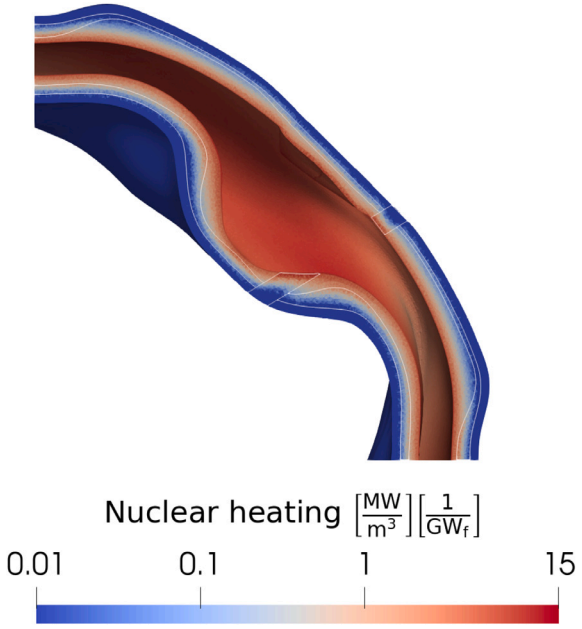

Fig. 37. Nuclear heating, as obtained from OpenMC with the set-up described in the text. The figure shows a cross-section through the $Z = 0$ plane of the radial build. The maximum heat deposition is at the first wall, with a peak value of 12.1 $\text{MW/m}^3/\text{GW}_\text{f}$. White lines mark the boundary of the neutron shield and the sector splitting bellow.

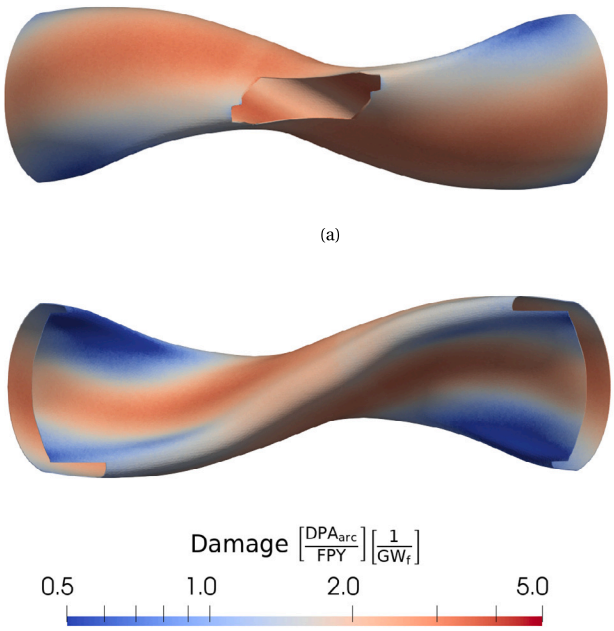

Fig. 38. Damage rate on the first wall described by the Displacement Per Atom (DPA) per GW of fusion power per year using the ARC-DPA model. (a) displays the outboard, and (b) shows the inboard side. Peak value is 3.9 DPA/GW_f/year and is located on the inboard side, around the mid plane. The mean integrated value is 2.2 DPA/GW_f/year. The colorbar is shared between the two sub-figures.

a more accurate estimate of neutron damage in these components. However, we also present results from the NRT model, which has been commonly used in past studies.

Most lattice-atom interactions occur at high neutron energies ($E_n >$ 1 MeV), where the Primary Knock-on Atom (PKA) energy typically exceeds the cutoff energy E_{cutoff}. Beyond this threshold, most of the excess energy is lost to electronic interactions. The damage energy per displacement process is thus approximated as $E_\text{D} \approx E_{\text{cutoff}}$. The cutoff energy was computed as $E_{\text{cutoff}} = 1000 \cdot A$ keV, where A is the atomic mass [267]. For our simulations, 56 keV for Fe and 63.5 keV for Cu were used in the ARC model to compute the displacement efficiency.

DPA was determined by dividing the number of displacements by the atomic density of the respective element in the material. For example, in the first wall, DPA was calculated as the displacements of iron isotopes normalized by the atomic density of iron in the homogenized material.

Using the NRT model, the peak DPA in the first wall is 34.9 DPA/FPY, while the ARC model yields 10.7 DPA/FPY, where FPY represents full-power years. Similarly, in the divertor, the peak DPA is evaluated to 36.2 DPA/FPY for the NRT model and 6.1 DPA/FPY for the ARC model. These values align with previous studies, which report similar ratios for Fe and Cu under 14 MeV neutron irradiation [268].

Fig. 38 illustrates the ARC-DPA simulation results for the first wall. After four years of operation at full 2700 MW fusion power, the cumulative peak DPA in the first wall is approximately 42.8 DPA, while for the divertor cooling elements, it is approximately 24.4 DPA.

In addition to DPA, the accumulation of helium and hydrogen within materials is also a critical factor in determining the lifespan of components in a fusion reactor. These quantities are typically measured in atomic parts per million (appm). Reliable first-principle simulations for the accumulation of helium or hydrogen in materials induced by 14 MeV neutrons are currently not available. Instead, heuristic estimates from related studies suggest an accumulation rate of approximately 10–30 He appm/DPA [269–271], although the methodologies behind these estimates are sometimes questionable and lack the required data for benchmarking purposes. Applying these estimates to the first wall of Stellaris suggests a range of 40–120 He appm/FPY/GW_f, or equivalently 110–320 appm per full power year (FPY) in peak locations.

The actual lifespan of these components will depend not only on DPA and on the accumulated helium and hydrogen gases due to nuclear reactions, but also the operational temperatures, and the structural requirements of the materials. One particularly important factor is the ductile-to-brittle transition temperature (DBTT), which is influenced by both the DPA and the accumulated helium within the material. Ensuring that structurally significant materials such as those in the first wall and blanket remain above the DBTT throughout the reactor's operational life is crucial. EUROFER steel under irradiation tends to harden (increasing yield strength), but also becomes more brittle. Operating steel in this hardened, brittle state is not necessarily disqualifying, provided that the material is used well below its yield strength limit.

As no structural stress simulations are performed in this analysis, the parameters for Stellaris are compared with available literature data for context and understanding. At negligible helium accumulation (He appm), the estimated DBTT for EUROFER97 under neutron irradiation is expected to occur around 200 °C [272]. However, when helium accumulation is present (a more relevant scenario for this analysis), the DBTT value carries significant uncertainties due to the limited material data available. For the EUROFER97-based first wall of Stellaris, which is expected to operate around 500 °C (see Section 2.7), the wall should remain well above the DBTT, despite the uncertainties induced by helium accumulation in the material [273].

Given these conditions, we estimate that Stellaris could achieve about 4 full power years of operation at 2700 MW fusion power, corresponding to approximately 42.8 DPA, before key components would need to be replaced by remote maintenance. Future high-flux, 14 MeV neutron irradiation facilities [274,275] are expected to provide greater clarity for these estimates. Furthermore, a detailed structural analysis of the first wall, blanket, and shield systems could align the structural requirements with the material properties, helping to determine when

Table 6
Key neutronics values as obtained from a 3D OpenMC calculation. FPY are full power years. 'Power Multiplication' is sometimes also called 'Energy Multiplication' in the literature.

Description	Value
TBR	1.074
Power Multiplication	1.20
Fast neutron flux (99th quantile) at coils [$1/m^2s$]	9.5×10^{13}
Coil lifetime (99th quantile) [FPY]	~10
Peak fast neutron flux at coils [$1/m^2s$]	2.0×10^{14}
Peak DPA in the first wall [DPA/FPY]	10.7
Estimated first wall structure lifetime [FPY]	~4–6
Peak nuclear heating (blanket) [MW/m^3]	35
Mean cryogenic nuclear heating (winding pack) [W/m^3]	35.5

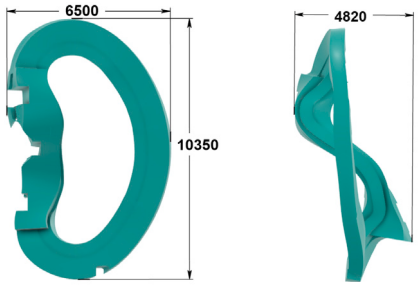

Fig. 39. Physical dimensions of the first coil of the coilset, including its casing (in mm). With casing, the coil is about 10.4 m tall, has 6.5 m of radial extent, and extends over 4.8 m in toroidal direction.

the safety margin relative to the yield strength limit might be exceeded.

Going forward, several strategies could be employed to manage elevated neutron irradiation levels, including:

- Targeted Replacement of High-DPA Sections: replacing only the first wall sections experiencing the highest Displacements-Per-Atom (DPA) levels could be an efficient strategy. These targeted replacements would not only extend the overall reactor lifespan, but also provide valuable samples for material characterization under high DPA conditions, contributing to better understanding and prediction of material behavior. Analysis of first wall replacement has not been performed, but it may be necessary to limit the amount of first wall replacements so that such replacements can be carried out during scheduled maintenance periods.
- Increasing Radial Distance Between Plasma and First Wall: by increasing the distance between the plasma and the first wall, the neutron flux density at the wall can be reduced, lowering the DPA rate and extending the lifespan of the wall and other reactor components. Non-constant offsets between the first wall and the plasma could be considered to optimally utilize the available space while remaining within first wall, breeding and shielding limits. Non-uniform offsets could also help reduce heterogeneity of DPA across the first wall by moving parts of the first wall that have the highest DPA outwards. The magnitude of any achievable reduction in DPA by optimizing the offsetting of the first wall to the plasma has not been studied within this paper, but is investigated in similar contexts [240].
- Applying Treatments to Enhance EUROFER97 Properties: enhancements to the properties of EUROFER, as explored in studies such as [276], could improve its resilience to radiation damage and potentially increase the lifespan of the first wall without requiring major design changes.
- Using a More Neutron-Resilient Material: exploring the use of alternative materials such as Oxide Dispersion Strengthened (ODS) steels or other Reduced Activation Ferritic/Martensitic (RAFM) steels could offer greater resistance to neutron damage compared to EUROFER97. However, these materials currently have a lower technological readiness level, and their implementation would require further research and development [277,278].

Additionally, the feasibility of using ferromagnetic steels such as EUROFER – which would affect the magnetic field quality in the plasma, and hence the confining properties – would need to be validated.

In conclusion, we have presented a preliminary conceptual study for the blanket and neutron shield system of Stellaris. This study includes estimates of the TBR, fast neutron fluxes at the superconducting magnets, nuclear heating in the cryogenic areas, and DPAs at the first wall. Key parameters are summarized in Table 6. It is important to emphasize that this study employs a simplified homogeneous model for the shield and breeder zones.

Future work should focus on advancing this preliminary model by conducting a detailed analysis of a heterogeneous blanket configuration. This will involve evaluating the neutronics, mechanical, and thermal performance of such a blanket, alongside a thorough manufacturability assessment. A critical risk to address is the interaction between lead-lithium and water, a well-documented exothermic reaction [279]. To mitigate this, we currently rely on established designs like the WCLL, which incorporates double-walled tubes to bolster the reactor's safety and reliability [280]. Additionally, further research—including simulation and experimental studies—will be necessary to address corrosion challenges and to understand the magnetohydrodynamic effects in liquid lithium-lead, similar to the studies performed in [245]. Activated corrosion products, activated lithium-lead and activated water will also require careful shielding considerations, due to their mobility around the building. These steps will be crucial for refining the blanket and shield design to ensure it meets the demands of a commercial fusion reactor.

2.9. Magnets

In Fig. 39 we display a selected coil of Stellaris with its corresponding casing, including physical dimensions in millimeters. The coils have an approximate size of $7 \times 5 \times 10$ m, with a typical circumference of 25 m, and the conductor needs to be manufactured using superconducting material, for which multiple options exist. High-temperature superconductors (HTS), particularly ReBCO-based superconductors, have important advantages for high-field magnetic confinement fusion. Most notably, they allow for designs with higher magnetic field strengths, as the superconducting material can withstand much larger critical current densities at high magnetic field strengths compared to conventional low-temperature superconductors [281–283]. The technology is also reaching maturity, with ReBCO-based coils tested at relevant parameters—despite outstanding problems such as quench management and high stored energy. At the time of writing, the current record for the highest field strength achieved by a tested magnet has 45.5 T [284] of peak field on the HTS. The SPARC tokamak [19] is currently being constructed using ReBCO-based magnets.

Despite their advantages, ReBCO-coated conductors pose several challenges for cable design, which typically involve assembling hundreds of individual HTS tapes in a specific arrangement. The major limitations for cables, especially in fusion applications, can be attributed to three key aspects. First, the mechanical stress and strain that the conductor and the cable endure during the manufacturing process and operation result in significant limitations. Second, the anisotropic behavior of the ReBCO material under magnetic fields leads to critical current density values that are much lower for magnetic fields perpendicular to the flat face of the tape than for magnetic fields parallel to the tape, especially for the fields and temperatures of interest. Third, ensuring electro-thermal stability (i.e., avoiding quench events and loss of superconducting state) is crucial during the design process.

Several successful cabling techniques have been developed over the past decade to address these challenges. Among these are concepts such

as CORC, VIPER, CroCo, and BRAST [83,85,281,285–287]. Additionally, HTS 'stack in groove' approaches – as applied in the Toroidal Field Model Coil (TFMC) built in collaboration between MIT's Plasma Science and Fusion Center (PSFC) and Commonwealth Fusion System (CFS) for the SPARC project – have shown promising characteristics [288,289].

For the superconducting magnets in this study, we propose a Non-Insulated (NI) concept. The NI method in the present work ensures that there is electric insulation between pancakes (azimuthally insulated) and only steel (electrical contact) between radial turns. More specifically, referring to Fig. 40, electric insulation between pancakes implies that current can only move in the Φ-coordinate direction (azimuthal) through the joints/connections at the first and last turns of each pancake (the yellow sheet represents the electric insulation). On the other hand, radial electric contact means that current can leak in the r-coordinate direction (radially outward), particularly during transients. The terminology of such a concept is coherent with the current literature (e.g. TFMC and FSU/NHMFL [282,289]).

Unlike low-temperature-superconducting (LTS) magnets, HTS magnets are fundamentally unlikely to quench unless they have a serious defect in them. Nevertheless, demonstration of quench management is necessary for risk mitigation purposes. NI coils offer a self-protecting mechanism without complex external systems, allowing current to bypass local hotspots and enhance thermal stability. They are passively protected by natural current redistribution. However, large stored magnetic energy and highly non-uniform critical current distributions (especially with low critical current regions) can still cause damage [288,289]. To mitigate quench damage, it is crucial to ensure that the ratio of operational current density to critical current density, j_{op}/j_{crit}, varies only very weakly along a turn, and does not exceed a critical limit, which we take here to be 80%.

For the conductor design discussed here, we consider a fully pre-soldered, field-aligned Stack Tape Cable (STC), enveloped in a copper jacket that constrains the tape stack in the chosen orientation, similar to the CroCo concept [286]. We exploit the anisotropic properties of ReBCO tapes and align the 'ab plane' (flat face) of the ReBCO tapes/stacks with the magnetic field orientation, generalizing and extending to the whole winding pack an approach proposed for the helical (heliotron) reactor with the STARS conductor [290,291]. Field alignment improves performance, but adds design complexity requiring precise calibration and advanced manufacturing techniques. Additionally, we utilize grading techniques (i.e., intentionally reducing the number of tapes where the magnetic field is lower [292]) to achieve an almost constant j_{op}/j_{crit} ratio along the turns.

The conductor is wound in non-planar stacked 'radial' plates made of stainless steel 316 (SS316), similar to concepts in previous designs [293,294]. Fig. 40 shows a cross section of the winding pack for a 256-turn coil (coil 4) and the geometric and material details of the single unit cell. For each coil, we select a square winding pack with a variable number of turns, ranging from 225 to 324 turns per coil.

We note that the winding pack orientation is fully decoupled from the HTS tape stack orientation. The winding pack orientation is chosen so that a flat face is tangential to the plasma at each point, allowing for a vacuum vessel surface that is as flat as possible and maximizing available space for the radial build while minimizing peak fields within the winding pack. Conversely, the orientation of the HTS tape stack is chosen to align with the magnetic field orientation at each point along the cable for each turn inside a winding pack.

Each turn is sized at 20 mm × 20 mm, with a 6 mm × 6 mm soldered tape stack embedded in a 15 mm diameter round copper former.

With these dimensions, the current per turn is constrained to a maximum value of 50 kA, allowing for the use of 'off-the-shelf' current leads to realize the connection between the superconductor in the coils at cryogenic temperatures to the bus bars, which are connected to the coil power supplies, at room temperature. The coils are cooled to 20 K using supercritical helium channels at 15–20 bar. This approach entails using the casing as the pressure vessel itself, eliminating the need for leak-tight pressure seals between the plates/turns. However, issues such as uncontrolled helium flow distribution could arise; the cooling concept is still under exploration. Alternative designs include closed channels with welded lids or soldered-in copper/steel pipes. In this paper, the operating temperature (Top) is set to 20 K to provide a consistent basis for analysis, but it may be desirable to lower the operating temperature to around 10–15 K to provide more margin. In the chosen unit cell configuration, the current density per turn is about 112 A/mm^2, and the current density per copper fraction is approximately 355 A/mm^2, aligning the winding pack design with similar proposed designs [288,289]. The resulting material fractions of each winding pack are summarized in Table 7. We summarize major coil features in Table 8. Note that we report the specs for only six coils due to symmetry (i.e., 48 coils divided into four periods, with each period containing 12 coils: six independent and six mirrored), simplifying the representation.

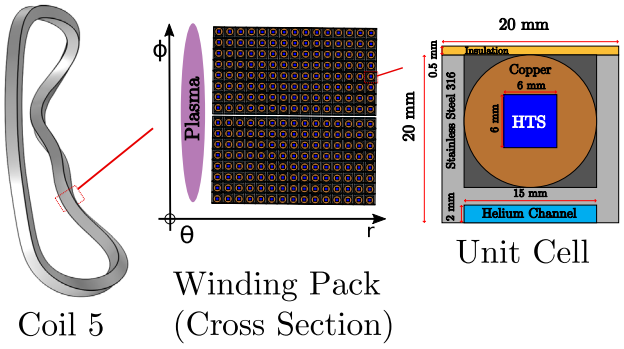

Fig. 40. A perpendicular cross section through the winding pack of the coil. The casing is not shown here, and the stacks are not aligned with the field for the sake of clarity. Note that Φ represents the toroidal coordinate, Θ the poloidal coordinate and r the radial coordinate.

Table 7
Material fractions in a winding pack of one of the Stellaris coils.

Material	Fraction [%]
Tape stack	9
Copper jacket	35
Solder	12
Steel	36
Helium (cooling)	8

In the following paragraphs, we discuss a high-level concept of a magnet system for the first version of the coils for the Stellaris class of stellarators, focusing on how the above challenges are addressed. Our focus here is on the *feasibility* of the concept, as opposed to a full engineering analysis. Some important design aspects, such as screening currents and field quality, are not covered in this short analysis. Instead, to validate the proposed design, we discuss the maximum field on the conductor and the operational critical current margin, the winding-induced curvature and torsion, the structural integrity of the winding pack, the contact resistance between turns, and peak temperatures and currents during a quench event.

Peak fields and critical current density. The peak magnetic field in stellarator coils can vary significantly from one coil to the next, especially in QI stellarators with a large magnetic mirror ratio. The peak field is also heavily dependent on the size of the winding pack, and is a decisive parameter for force and critical current density calculations. Here, we compute the peak fields using a 3D magneto-static model carried out by means of finite element analysis with the commercial software COMSOL MultiPhysics® [295]. For this calculation, we assume that the current density distribution is uniform across the winding pack cross-section. Fig. 41 shows the peak fields for each independent coil. At the chosen 9 T axis-averaged magnetic field strength, the peak field inside

Table 8
The main coil parameters for every unique coil in Stellaris. 'WP' stands for 'winding pack'. j_{op} refers to the operational current density (in the text , j is used equivalently). Minimal distances are with respect to the neighboring coil.

Coil Number	0	1	2	3	4	5
I (total Amp-turns) [MA]	15.4	14.6	13.8	12.9	12.5	11.2
Number of turns	324	324	289	289	256	225
Turn current [kA]	47.6	44.9	47.8	44.7	48.9	49.8
j_{WP} [A/mm^2]	119	112	120	112	122	124
$j_{tape\text{-}stack}$ [A/mm^2]	1323	1249	1330	1243	1360	1384
Cross section side length [mm]	360	360	340	340	320	300
Min. casing-to-casing dist. [mm]	11.4	114	91.4	135	326	475
Min. casing-to-LCFS dist. [m]	1.06	1.04	1.05	1.08	1.11	1.07
Coil mass, no casing [ton]	24.2	25.4	21.6	21.5	19.0	17.0
Peak field [T]	24.6	23.1	22.0	21.0	21.4	19.5
Max. curvature [m^{-1}]	1.97	1.75	1.94	1.42	2.12	1.86
Min. curvature radius [m]	0.51	0.57	0.52	0.60	0.47	0.54
Max. torsion [rad/m]	5.27	3.76	4.46	3.76	3.99	3.91
Max. j_{op}/j_{crit} no grading [%]	60.5	46.5	50.2	54.1	56.3	55.8
Max. j_{op}/j_{crit} with grading [%]	80	80	80	80	80	80
Tape length no grading [km]	807	847	721	717	636	567
Tape length with grading [km]	167	161	146	134	131	118
Max. turn linear force [kN/m]	540	404	398	400	450	380
Max. WP linear force [MN/m]	174	131	115	115	115	85
Peak stress on WP [MPa]	<650					
Self-inductance [H]	1.30	1.44	1.10	1.10	0.90	0.62
Total energy [GJ]	110.58 (2.76 GJ per coil)					
Turn-to-turn contact res. [μΩ]	11.2	11.2	10	10	8.85	8.85
Charging time [h]	≃600 (26 days)					
Max. temp. during quench [K]	<300					

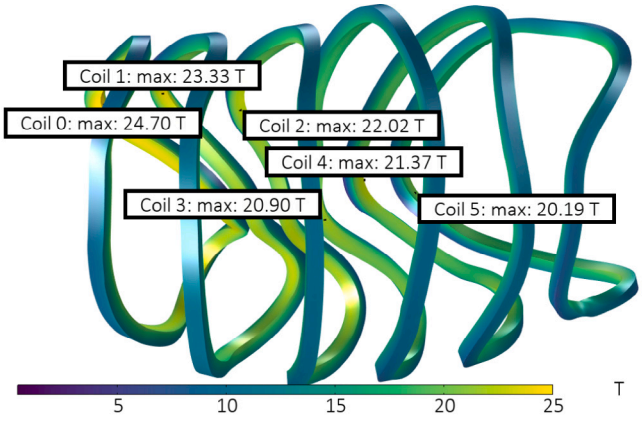

Fig. 41. Results of a 3D magnetostatic finite-element simulation in one half-module, taking into account the field generated by Stellaris. Pictured is the magnetic field strength at the surface of the winding pack. The size for each winding pack is consistent with values reported in Table 8. The labels indicate the maximum value of the field for each coil and the colormap indicates the norm of magnetic field in Tesla (T).

the winding pack reaches 24.59 T.

We now evaluate the effect of the high magnetic field strength in terms of the critical current of the HTS tape stack cable. ReBCO-based HTS tapes have a strong dependence of the critical current on the magnitude of the field component orthogonal to the direction of the current and the angle between the field and the so-called $\hat{c}$-axis of the ReBCO crystal, which is usually (but not always) orthogonal to the flat side of the tape. We model this effect by using the magneto-angular parametrization of the critical current density as a function of the field strength and the angle between the field and the c-axis suggested in [296]. We fit this model to a dataset of measurements of the critical current of a commercial ReBCO 2G HTS wire collected at 20 K and different field strengths and angles with respect to the tape [297]. The critical current values presented here are calculated at 20 K, since we assume that the temperature is uniform in the winding pack and that there are no transients. Later, a temperature dependency

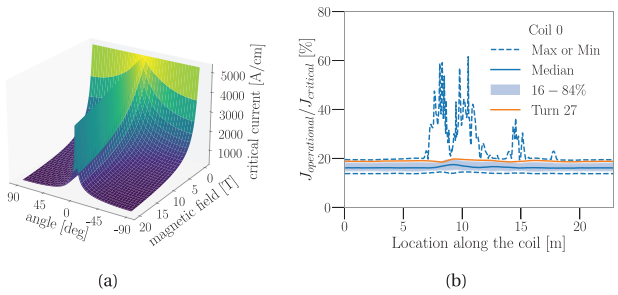

Fig. 42. (a): Critical current density parametrization as a function of the field strength and angle between the field and the plane, at 20K, for a commercial ReBCO 2G HTS tape. Here the magnetic field always refers to the component on the plane orthogonal to the current direction. (b): Ratio of operational current density over critical current density along coil 0. A representative turn is shown in orange, while the distribution across turns is illustrated by the maximum and minimum values (dashed blue), the median (solid blue), and the interval between the 16 % and the 84 % quantiles (shaded region).

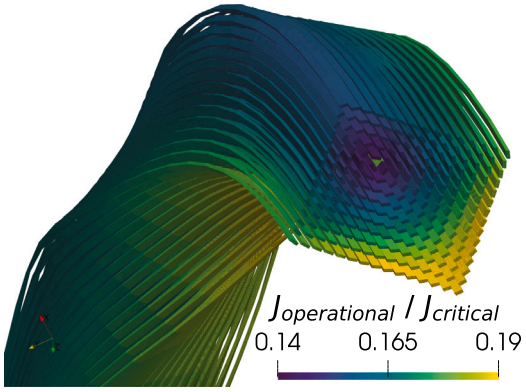

Fig. 43. A cross section of coil 5, displaying all turns as thin layers to emphasize the field-aligned orientation of each turn. The turns are colored according to the ratio j_{op}/j_{crit}, before applying any grading.

will be considered for the quench modeling. The left plot of Fig. 42 shows the model we use for j_{crit} as a result of our fit.

We exploit the high anisotropy of j_{crit} with respect to the inclination angle to maintain a high critical current despite the large field values inside the coil winding pack by orienting the tapes within the winding pack optimally. To obtain the actual orientation of the tapes, we employ a simple optimization algorithm to balance the required level of field alignment while minimizing torsion in the tapes. Fig. 43 shows a cross section of the winding pack of coil 5, illustrating the chosen orientation. Each turn is represented simplistically as a flat cable to highlight the orientation of the tape stack.

With this orientation, we calculate j_{crit} along the coils. To do so, we compute the magnetic field using a Biot–Savart integration over a finite coil with a square cross-section and uniform current density [12,298].

Illustrative results of the critical current density calculations are shown in the right-hand-side plot of Fig. 42, which displays the ratio of the operational current density to the critical current density for the turns present in coil 0, the coil experiencing the highest magnetic field strengths. The horizontal orange line indicates the j_{op}/j_{crit} ratio along a representative turn inside the coil. To illustrate the distribution across turns, we display the maximum and minimum values, as well as the median and the interval between the 16% and 84% quantiles for each cross section along the winding pack central filament path.

The safety margin of 80% is not exceeded at any point, and a grading technique can be employed to tune the critical current density so that a relatively constant j_{op}/j_{crit} is achieved. This grading could

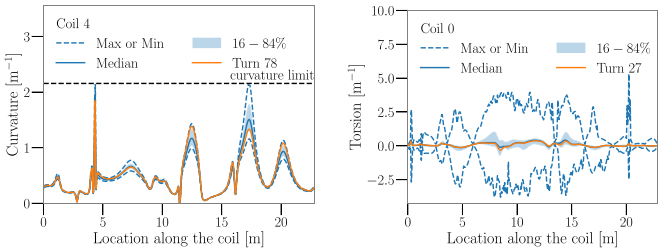

Fig. 44. (a): Analogously to the right plot in Fig. 42, curvature distribution for coil 4. The upper limit is obtained by measurement in CroCo [286] cable stack as described in the text. (b): Torsion distribution for coil 0.

involve locally replacing the superconducting tape with copper tape (or other stabilizers compliant with the tape structure) wherever needed. Using this technique would also reduce the amount of HTS tape required: coil 0, without grading, would require 807 km of 6 mm tape, but with perfect grading (assuming $j_{op}/j_{crit} = 80\%$ everywhere), this requirement decreases to 167 km.

It must be reiterated that locally aligning and grading the tapes introduces engineering complexity to the design and manufacturing process. Alignment requires precise calibration due to the narrow j_{crit} peak around the ReBCO $\hat{c}$-axis, which restricts flexibility for adjustments and necessitates advanced manufacturing tools and techniques for tracking tape alignment. In our quench simulations, we proceed with the assumption of a constant j_{op}/j_{crit} throughout the turns, as achieved through tape grading.

Winding-induced strain. HTS stacks degrade under strain, induced by bending and twisting them into the required form for fusion magnets. Stellarator non-planar magnets are particularly complex. Previous studies have examined bending strain and field alignment optimization [299,300]. While a full strain analysis is beyond the scope of this paper, especially considering the strong anisotropy of the HTS tape stack as a composite material, we can draw conclusions about the feasibility of this concept by analyzing the curvature and torsion profiles of each turn across the winding packs. In the context of this analysis, we refer to curvature as the total curvature, equal to the square sum of the geodesic and normal curvatures.

The left plot of Fig. 44 illustrates the curvature profile for coil 4, which experiences the largest curvature values across the coil set. Turn-to-turn variation is significant, especially in high-curvature regions. To extract a curvature limit, we compare this distribution to the values obtained in [301] for a CroCo [286] cable with a maximum size of 3×3 mm. That study shows that the bending radius achieving critical current degradation is lower than 5%, meaning $I_c/I_c^0 > 95\%$, where I_c^0 is the critical current of the unbent cable, with ranges between 206 and 250 mm for the cable under consideration. The minimum bending radius depends only mildly on the bending angle, indicating no significant difference between applying hard-way or easy-way bending for this type of cable. However, the minimum bending radius exhibits some statistical variation across the samples collected in the aforementioned study. We therefore consider a reference value of 232 mm, which is the average value obtained for the measurements in easy-way bending only, the ones showing the largest degradation. We scale this value to a 6×6 mm cable, obtaining 464 mm as the minimum bending radius, which implies a curvature limit of $\kappa_{limit} = 2.16\ \mathrm{m}^{-1}$. All turns are safely below this limit, allowing us to conclude that degradation induced by bending is not a limiting factor for the present concept.

The right plot of Fig. 44 shows an analogous distribution for the torsion of coil 0, which experiences the highest torsion values. A typical turn experiences torsion below 1 rad/m. However, some turns present a spike in the torsion profile up to about 5 rad/m, corresponding to a twist pitch of about 1.25 m. Investigation of these cases showed that these turns experience a highly twisting magnetic field, where the magnitude of the field component orthogonal to the current direction drops to almost zero, fluctuating significantly. A study of the impact of torsion on HTS tapes demonstrates no degradation for twist pitches larger than 200 mm [302], suggesting that our concept is safely above the degradation limit.

It is important to emphasize that critical current degradation is not the only problem that appears when applying large torsion. Another key issue is delamination, wherein the different tapes in the stack may naturally follow slightly different orientations. While a complete analysis of delamination is beyond the scope of this paper, we assume in our concept that the copper jacket surrounding the HTS tape stack is strong enough to hold the cable in place, inducing the necessary torsion and curvature to achieve the required orientation of the tape stacks.

Structural analysis. We now evaluate the effect of the high magnetic field inside the coil in terms of the material stress and strain concentrations for the magnet design. An axisymmetric model was employed to approximate the magnetic field $\mathbf{B}$ and the resulting $\mathbf{I} \times \mathbf{B}$ loads. This approach simplifies the analysis while capturing the maximum field magnitude (~25 T) and the corresponding peak loads, which are critical for understanding the structural forces in the system. The model effectively treats the coil as a planar coil in a linear arrangement to approximate the field within the winding pack, with the external field represented as a linear stack of circular coils. It is acknowledged that the axisymmetric assumption does not account for directional variations in $\mathbf{B}$ that occur in the true 3D geometry, which could influence the detailed load distribution. However, for the purposes of this study, the axisymmetric model provides a reasonable first approximation. Future work will include a more detailed 3D analysis to address these directional effects. For consistency with the inter-coil support structure model (introduced in the next section) and the magnetic field peak and distribution, we locate the center of the winding pack at a radius of 2.5 m. The out-of-plane (hoop) stress is then evaluated by integrating over the full revolution of the coil. Appropriate continuity boundary conditions are applied to the surfaces of the 'air' domain proximal to the outer pancakes. In the simulation, the plates and casing are modeled as independent bodies in contact with each other, with no friction or clamping, to capture the most conservative stress state.

The wall thicknesses of the casings are consistent with the intercoil support structure (introduced in the next section). In this section, we show only local effects within the winding pack.

Fig. 45 illustrates the resulting von Mises stress plot within the winding pack as obtained with the model described above. The peak stress is located at the center of the winding pack, toward which the local forces are oriented. For the present design, the peak stresses are in the range of 600 MPa, well below the imposed stress limit of 800 MPa (see Section 2.10). The peak strain on the HTS stack due to the deformation of the winding pack is below 0.2%, which is within acceptable limits [303,304], even when adding strain from bending.

Charging time and steady state losses. Charging times are crucial, as they significantly impact the duration of remote maintenance periods. Additionally, electrical losses in steady-state are important to estimate parasitic electrical inefficiencies in the reactor's power balance. To obtain the value of the contact resistance (R_c), we used a two-dimensional electrostatic model to calculate the current path between adjacent cables. This model assumes no insulation between turns in one pancake, but complete insulation between pancakes. Other insulation approaches, such as partial or metal insulation [305–307], are not considered for the time being. From the present design, we obtain an overall contact resistivity ranging from a maximum of 11.2 μΩ for coil 0 to a minimum of 8.85 μΩ for coil 5. The different resistance values are due to the varying number of turns per coil. Resistive joints with resistance in the order of 4 nΩ have been demonstrated in the literature [288,308,309], and this value is assumed here. Inductance

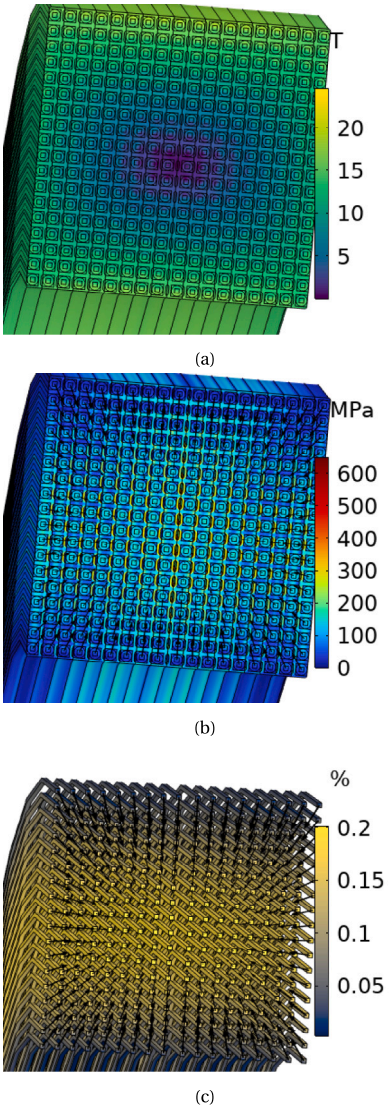

Fig. 45. Visualization of (a) the three-dimensional revolved magnetostatic field strength within the winding pack cross-section, (b) the von Mises stress in a revolved cross-section of the winding pack of coil 0, and (c) the strain state in percent due to the deformation of the winding pack. Although based on a 2D model, the results are represented using a 3D revolved rendering for visualization purposes.

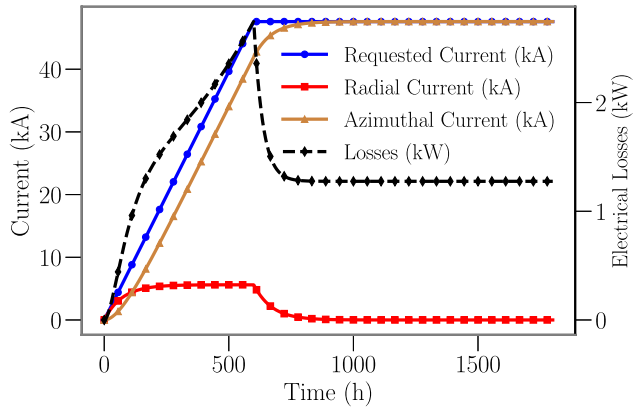

Fig. 46. Azimuthal and radial current distribution, and electrical loss power evolution for one group of coils (i.e., 8 coils with the same current connected in series) during charging. The overall turn-to-turn contact resistance per coil is around 8.85 μΩ (Coil 4), and the charging time is 600 h.

values are obtained via a loop integral, using a central filament approximation of each coil. To simulate the dynamic behavior of the NI coil during charging, steady-state, and open-circuit quench scenarios, we implemented a simple low-fidelity electrothermal circuit model commonly used in the literature [310,311]. This simple model captures the key aspects of charging, steady state, and quench dynamics in NI coils. Designing for an open-circuit scenario is essential due to several critical engineering causes that can lead to such a failure. Potential causes include power supply failure and current leads failure, during which the current can no longer be driven through the coil, resulting in uncontrolled conditions.

To simulate the charging and steady-state behavior of Stellaris, we group the coils with the same currents in series (eight coils per period), resulting in six groups of coils. Fig. 46 shows an electrical simulation for one of the coil groups (specifically, coil group 4), though the simulation was carried out considering the full stellarator. The typical pattern of the radial currents (red dashed line) in a non-insulated coil is visible, with radial currents being non-zero during charging and dropping to almost zero after an exponential decay, forming a plateau. Note that any non-zero radial current due to the redistribution at the joints or at the current leads is currently neglected.

The AC losses (black dashed line) exhibit non-linear behavior during ramp-up due to the presence of the superconductor (power-law behavior), while the constant plateau for $t > 800$ h represents the losses due to the resistive joints. In the simulation, we assume a resistive joint every two pancakes. With an operational turn current of approximately 50 kA, we achieve a heating power as low as 10 W per joint. This results in approximately 7.5 kW steady-state losses for the entire stellarator coil set of Stellaris, which is negligible compared to other electricity consumption and within the cooling capacity of existing cryocooler designs. Note that this steady state electrical power should be smaller than the total nuclear heating of the coils, the coil cases, and the remaining 20 K cooled parts of the support structure, which will be examined in future studies.

The coil group needs to be charged over a period of 600 h (25 days) to reach its full operating current. The charging duration is deliberately set to a very slow ramping rate, to mitigate the risk of inducing a quench due to transient losses. This cautious approach is necessitated by the large inductance and the characteristic L/R-time constants of the NI coils.

Quench considerations. Quench detection systems and active protection systems for NI coils—such as quench heaters, magnetic damping [312], and capacity discharging [313]—can help ensure that a coil quenches uniformly, and such concepts are currently under development. Design methodologies for systems with the elevated energy levels of the present design are explored in the literature [314]. However, in the current design we opt for a passive quench protection system, meaning that the coil's energy is entirely dissipated within the coil's cold mass. As a first model, one can calculate the temperature rise upon dissipating all the coil energy within the coil, factoring in cryogenic material properties [315] and the unit cell configuration. We find that the overall temperature in the coils of the current design remains below 300 K for each coil when uniformly heated with its own stored magnetic energy. Note that this upper limit temperature is utilized in literature [316–319].

As the pancake-to-pancake joints are resistive in the design presented here, the primary current redistribution occurs within the individual pancakes during the initial phase of the quench. Assuming an almost constant $j_{op}/j_{crit} \sim 0.8$, achieved via a combination of alignment and grading, we simulate the quench behavior of a single pancake with sixteen turns, using the inductance and energy parameters derived from the full coil of Stellaris. In the conventional circuit model [310,311], each RL unit represents one turn of the pancake—assigned with inductance, mutual inductance with other turns, a critical current value, and a turn to turn contact resistance. These unit cells are then arranged in series to represent 16 RL units (i.e., 16 turns).

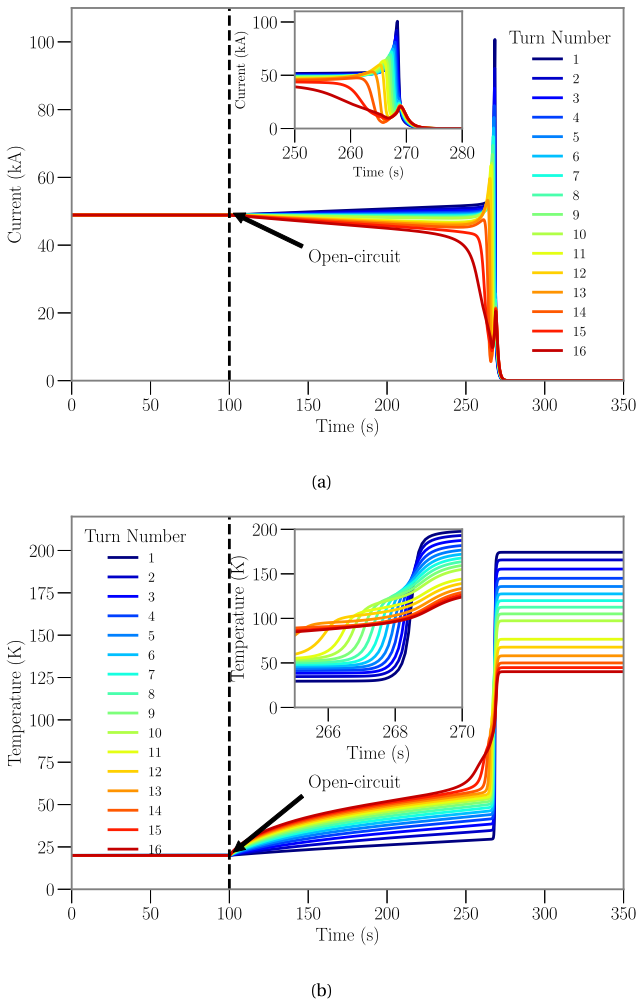

Fig. 47. Quench behavior in one pancake as obtained with 1D open circuit model, with inductances and resistivities corresponding to Coil 4. (a): Dynamics of the turn current during a quench. (b): Simulated temperature rise within the winding pack.

In Fig. 47, we plot the current and temperature distribution during an open circuit event for coil 4. When we open the circuit in the simulation, we first observe an incubation phase (between 100 and 265 s), where the current flows radially and redistributes according to contact resistance and inductance. This phase is followed by an inductive phase (between 265 and 269 s), in which the azimuthal current rapidly redistributes between turns due to inductive coupling, creating current distributions within seconds and generating an 'inductive quench wave' typically observed in NI coils [289,320,321].

The quench concludes with the resistive phase ($t > 269$ s), where the coil transitions to a normal resistive state and the energy is entirely dissipated within the coil's cold mass. In the bottom panel of Fig. 47, the maximum temperature after the quench events is shown to remain below 200 K for each turn. It is important to note that these temperatures represent the maximum value calculated for each 1D section in the simulation. Given the nature of the 1D model, however, they can be interpreted as approximate averages for each turn, rather than local hotspot temperatures. The actual hotspot temperature within a turn could be significantly higher due to finer-scale non-uniformities that are not resolved at the simulation's current level of detail. This is particularly relevant in cases of low thermal conduction between turns, where localized heating can be more pronounced. To account for these uncertainties, we adopt a conservative maximum allowable hotspot temperature of 300 K for safety considerations. Future work will focus on enhancing the resolution of the simulations to capture hotspot temperatures at a 'sub-turn' level, providing a more accurate representation of the temperature distribution during quench events. The different temperatures between turns (ranging between 120 K and 200 K) are due to the varying current peaks during the inductive phase of the quench and the low thermal conduction between the turns in the model, as it uses the thermal conductance of 16 RL-unit cells arranged in series. Note that the current analysis assumes that all the coils are open-circuited and quenched at the same time, or within a fraction of seconds between each other. A scenario in which only one (or part) of the coils quench before the others would result in highly asymmetric mechanical loads on the structure, and this should be avoided. Future analyses will evaluate this scenario, as well as highly risky quench scenarios such as hotspots due to damages, hot slug of helium coming through an inlet, etc.

A key challenge during a quench event is managing the high rate of change in turn current ($\partial I/\partial t$) while maintaining toroidal symmetry in the electromagnetic stresses. To address this, the system design includes early detection of hotspots and the capability to quench all coils simultaneously using quench heaters or capacitor discharge systems [313]. Operation in an N-1 configuration, where one coil is quenched while the others remain active, is explicitly avoided. Additionally, matching the L/R ratio during the inductive quench through controlled adjustments of contact resistance is a potential solution under consideration. In the simulated quench event, most of the current in the turns decays within approximately two seconds. Despite the strong current variation, no large voltages are simulated in the NI coil. However, significant parasitic eddy currents are expected to flow in adjacent reactor components during the coil quench. To mitigate strong Lorentz forces on the vacuum vessel, 'close coupled secondary' (CCS) loops – typically made of hard copper and inductively closely coupled to the superconducting coils – can be included in the reactor design. These loops would take on large transient eddy currents induced in them during the 'inductive quench wave.' Such loops have two benefits: relieving heating of the HTS (as a significant portion of the current inductively transfers from HTS tapes to the CCS loops) and slowing the collapse of the magnetic field, as seen by other components [322,323]. A more detailed study of such eddy currents is left for further investigation—noting that the CCS may impact charging time and charging losses, too.

2.10. Support structures

For high magnetic field fusion devices, the support structure must withstand the resulting large Lorentz forces. Various stellarator support structure concepts have been suggested over the years [59,324–328], but no high-field stellarator designs with modular coils and $B > 20T$ at the conductor have been presented until now. Whether there exist support structure solutions for high-field stellarators with modular coils has therefore been a source of uncertainty for stellarator reactor studies.

Here, we suggest and analyze for the first time a support structure concept designed to cope with the high electromagnetic (Lorentz) loads of a high-field HTS stellarator. Structural steel for coil casings and inter-coil support structure need to fulfill several criteria, including high-yield strength at cryogenic temperatures, low activation, and manufacturability for irregular parts as required in a stellarator. We have chosen AISI 316LN steel as the support structure material for this concept. This is standard in the industry as a cryogenic high-strength steel (it is used, for example, in ITER [329]). The 316LN grade can be manufactured in the form of plates, castings, or forgings, and its yield strength at the support structure operating temperature range (20 - 30 K) is around 1000 MPa. We note that at the high field strengths considered here, gravity and thermomechanical loads are lower than the electromagnetic loads on the support structure, so we neglect the former in our analysis.

In order to estimate peak stresses in the design, we perform a linear stress finite element analysis in 'Ansys®Mechanical, 2023 R2' (Ansys),

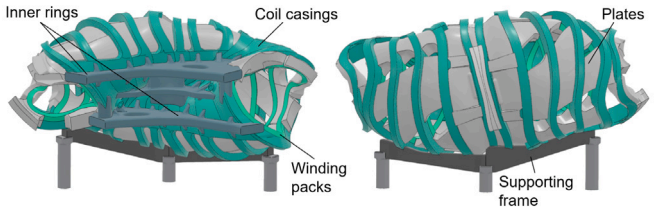

Fig. 48. Schema of the support structure set-up used for the analysis. The exact set-up of the stress simulation with boundary conditions and connection is described in the text. (a) Internal view; (b) external view.

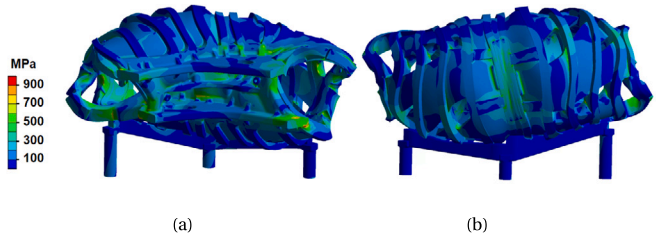

Fig. 49. Von Mises stress in the support structure under full load. Forces are calculated according to an axis-averaged magnetic field strength of 9 T. The majority of the support structure stays below the design limit of 800 MPa for cryogenic AISI 316LN steel. (a) Internal view; (b) external view.

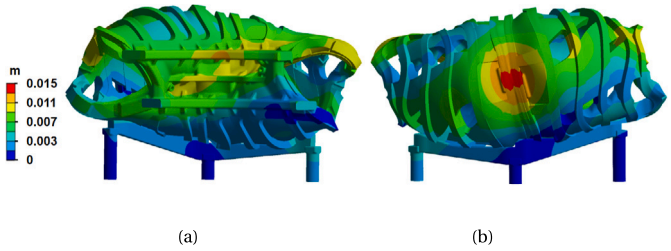

Fig. 50. Displacement analysis of the coils under full load. The peak displacements occur in the outboard region at the toroidal location where the magnetic field is highest in the QI stellarator. (a) Internal view; (b) external view.

for which we define a 3D model consisting of the coil winding packs and a design of the coil support structure—which consists of casings, inter-coil supports, and the central support ring. Fig. 48 schematically shows the different components in one module. For the simulation, we 'smear out' the internal structure of the winding pack as one homogeneous and isotropic material. We take an effective average of the winding pack material, obtaining an averaged Young's modulus of about 170 GPa and a Poisson's ratio of 0.3 for the winding pack. For this high-level calculation, we simply consider the support structure and the casings with the winding pack that carries the loads to be fully bonded.

We then proceed to calculate static electromagnetic loads, using a fixed discretization of 300 points for each coil. This point load is then converted to a volumetric load, mapped to the section of the winding pack (WP), and interpolated with the adjacent points within Ansys. Resulting net forces for each coil range from 100 MN to 350 MN per coil. We model only one full stellarator module (one field period), and periodic boundary conditions are applied to ensure the displacement field is continuous at the interfaces. Support legs are constrained in the Z and toroidal φ directions at their root to simulate the behavior of cryogenic legs, which are not modeled here but which would result in similar behavior [330].

The support structure design includes three key features:

- thick steel casings around the winding pack;
- welded or bolted plates between the coils to stabilize lateral loads, similar to the concept suggested in [59];
- inner support rings that carry a major fraction of the net centering force.

Depending on the local force field, support plates are not needed everywhere. This creates natural openings that can be used as ports for internal components, such as the first wall and blanket inlet/outlet. The open port area is mostly located on the outboard side of the machine, in the low-field region, and amounts to roughly 200 m^2 per module. We design a specific opening for the ports for ECRH injection from the inboard side, which is included in the stress calculations.

The coil casings could be cast with parts weighing between 63 tons and 200 tons—which is challenging, but comparable to existing parts in heavy machinery [331]. The plates between the coils have thicknesses between 0.7 m and 1 m and could be forged, with the heaviest plate in this design weighing 58 tons. The inner rings, about 0.7 m thick and weighing about 200 tons each, can also be forged. The reinforcement gussets would be designed to be welded as the coils are successively installed. The weights of these parts are compatible with industry standards.

A linear structural simulation is carried out using the volumetric loads and boundary conditions in Ansys. Second-order tetrahedrons are used for meshing, with a maximum mesh size of 0.15 m. Results displaying peak stresses are shown in Fig. 49. Following the ASME Boiler and Pressure Vessel Code Section VIII Division 2 [332], Eurocode 3 [333], and Eurocode 8 [334], the stress state needs to be decomposed between membrane and membrane plus bending stresses then respectively compared to 2/3 of the yield stress, and the yield stress as upper limits. We study the stress state of our design in multiple regions; the membrane stress in the high stress regions is lower than 660 MPa. To simplify the assessment and the readability of the stress of this high-level concept, we propose considering von Mises stresses as a proxy for membrane plus bending stresses. The simulation results indicate that those are below 800 MPa throughout most of the structure, demonstrating its ability to withstand the electro-mechanical loads. In the coil casings, the stress is below 700 MPa, providing a margin for manufacturing defects inherent to steel casting. It is worth reiterating that in comparison to tokamaks, QI stellarators are not subject to disruptions and fatigue from cyclic loadings. Therefore, our main design focus is the static electromagnetic loads.

Fig. 50 reports on simulated displacements of coils under full load. A peak displacement of 15 mm is simulated here in the outboard side of the high-field region. To quantify the effect of this displacement, we repeat the most sensitive calculation: the calculation of the location of the islands. We find distortions of the island locations to a comparable degree as those caused by finite β effects as shown in Fig. 13, which ultimately need to be controlled with an array of correction coils.

Finally, detailed tolerances, assembly, and manufacturing of the support structure would need to be considered in further analyses.

2.11. Remote maintenance

Throughout the lifetime of a fusion reactor, several scheduled maintenance periods must be planned to replace deteriorating components. Routine maintenance intervals are based on the anticipated lifespan of critical parts. Key components expected to require multiple replacements during the stellarator's operational life include first wall tiles, blanket modules, and divertor plates. Minor maintenance tasks should be manageable without significant machine disassembly, but unplanned interventions must also be considered. These could include replacing damaged diagnostics, repairing minor leaks, and addressing the failure of major components. In this section, we outline strategies for managing both major unplanned interventions and scheduled remote maintenance periods.

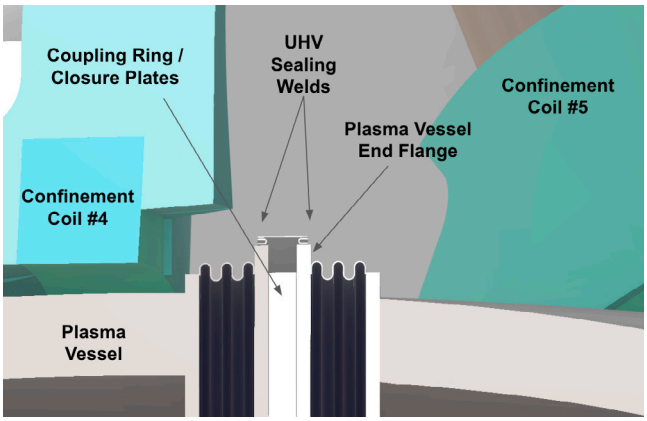

Fig. 51. Schematic visualization of the design of the sector interface, which is located in four symmetric positions around the torus.

While remote maintenance in tokamaks is explored in the EU DEMO program and conceptualized to utilize a combination of large vertical and horizontal ports [335,336], analogous concepts for stellarators are far less mature. Compared to tokamaks, stellarators face the challenge of regular vertical ports often being infeasible due to irregularly distributed vertical openings between the non-planar coils. Remote maintenance concepts via vertical port openings almost always require a rail system to transport heavy blanket segments to the openings [59]. The installation of such rail systems is often remarkably complex, due to the need to transport components weighing up to several tens of tons within the vessel.

There have been several investigations into remote maintenance concepts for stellarators [337–342]. One explored method is known as 'sector splitting,' which involves removing a complete toroidal section of the reactor without removing individual coils. This approach forms the basis for the chosen maintenance strategy of the Stellaris reactor. This procedure offers a significant advantage over traditional port-based maintenance approaches by providing substantial access to the inside of the plasma vessel at the two ends of the removed sector. We note that the sector splitting approach to maintenance is particularly well-suited for stellarator designs with modular coils—while sector splitting is also possible in tokamaks, it would first require the removal of large poloidal field coils, leading to further complications during the maintenance period.

Key to sector splitting is the careful design of the splitting interfaces, and a meticulous procedure to manage nuclear contamination. Fig. 51 shows the schematic design of the sector interfaces, which in the present design are located at four distinct locations around the torus. The interface is designed to enable dynamic containment (via internal atmospheric depression) and re-weldability during the procedure, explained in more detail below.

The necessary individual steps of the remote maintenance procedure using the sector splitting approach can be summarized as follows:

1. **Machine preparation**;
2. **Sector interfaces access operations**;
3. **Sector splitting operations**;
4. **Sector module transport operations**;
5. In-vessel systems removal;
6. Plasma vessel preparation;
7. In-vessel systems installation;
8. Assembled module transport to torus hall;
9. Sector joining and sealing operations;
10. Reconnection of services and remote maintenance equipment removal;
11. Machine recommissioning and plasma vessel conditioning.

The first four steps, highlighted in **bold**, are discussed in more detail below. Full details, however, are outside the scope of this paper, and are the subject of dedicated R&D.

Machine preparation. In the first step, the device must be prepared for disassembly, which involves isolating and disconnecting all associated service connections to the sector modules that need to be removed. These activities include, but are not limited to:

- De-energizing and warming up the primary confinement coils;
- Draining and purging the liquid breeder material within the breeder blanket modules;
- Draining, purging, and disconnecting all machine service lines;
- Disconnecting and removing ancillary external equipment;
- Raising the plasma vessel and cryostat to atmospheric pressure using dry nitrogen.

Immediately after operation, an initial cool-down time will be required to allow short-lived radionuclides to decay and to reduce the gamma radiation flux to acceptable levels before deploying the remote handling systems. Based on previous assessments, this cool-down period is expected to be approximately 30 days [343]. It is assumed that all necessary preparation activities will take place within this cool-down period to minimize the overall maintenance duration. The corresponding vacuum pump-down, conditioning, and system commissioning activities required at the end of the maintenance phases are similarly assumed to take approximately 30 days [343].

As it will be necessary to breach the plasma vessel containment boundary to split the sectors, active ventilation of the plasma vessel during the sector splitting operation is required. This ventilation aims to control the spread of contamination (both gaseous and particulate) by maintaining a negative pressure differential between the plasma vessel and the torus hall environment. The proposed design targets a pressure differential of 125 Pa across the interface opening [344]. To enable active ventilation, temporary connections to suitably monitored exhaust manifolds will be established during the sector splitting and transport to the hot cells. Preliminary in-vessel cleaning may be necessary to remove as much of the activated dust that has accumulated during operations as is possible. These cleaning operations would be performed using small dexterous manipulators deployed through dedicated access ports in the plasma vessel near the sector interfaces, similar to the manipulators used in JET [345]. Such dexterous manipulators will need to be hardened against gamma radiation, and the radiation tolerance of such devices – as well as the effect on planned maintenance operations – will need to be considered carefully in future design studies.

Sector interfaces access operations. After the initial machine preparation, the sector interfaces will need to be readied for separation. To split the modules from each other, the cryostat vacuum must be breached. Local sealing welds around removable sections will be cut, and the 'clamshell' panels in the cryostat shell will be removed. This operation can be accomplished using bespoke remotely operated or autonomous cutting tools and a specifically designed lip weld interface joint. 'Cold' cutting operations are preferred due to the presence of hydrogen in the vessel, likely using a 'nibbler' or reciprocating punch-type tool. Once the sealing lip welds are cut, the cryostat clamshell panels are removed, as shown in step 1 of Fig. 52.

Next, to access the sector interfaces and allow the sectors to separate, it is necessary to remove the inter-coil support structure between coil 4 and coil 5. The respective structure members, highlighted in the left picture of step 2 in Fig. 52, need to be designed specifically to be removable. This can be achieved using teleoperated manipulators. Once this removal is complete, remote handling access is granted to the sector interfaces, as shown in the top-right image of step 2 in Fig. 52.

In the interface, an ultra-high vacuum (UHV) seal is needed to obtain the necessary vacuum quality during plasma operations. This will be achieved through lip-welding a collar around the interface

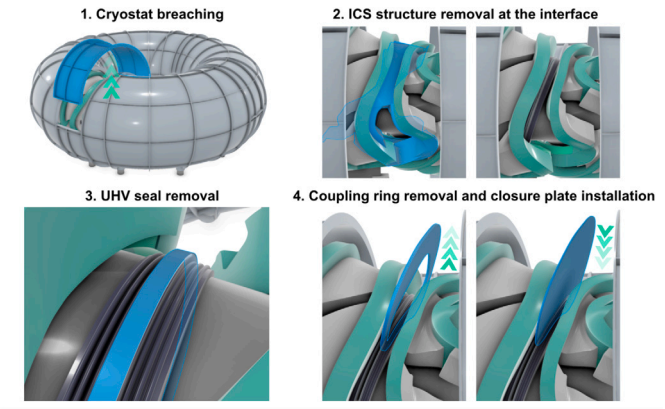

Fig. 52. A schematic procedure of the sector interface splitting, described in more detail within the text.

perimeter. The UHV seal does not mechanically couple the different sector modules together. The mechanical connection occurs separately at the interface flanges, for example, using a bolted interface. In the next step of the procedure, the UHV vacuum seal is removed by cutting the lip welds and removing the sealing collar, as illustrated in step 3 in Fig. 52.

Next, a removable, straight 'coupling ring' is removed from between the coils in a predefined direction to further increase clearance at the interface, as seen in the lower-left image of step 4 in Fig. 52. Once this has been removed, two closure plates can be installed at each interface to provide the primary method of containment for particulate and gaseous contamination, as shown in the right-hand picture of step 4 in Fig. 52. Although there remains a risk of some spread of contamination during this plate removal and insertion step, it is expected that through cleaning the inside of the plasma vessel – and by maintaining a sufficient depression within the plasma vessel during the operation – any external contamination can be kept to acceptable levels. However, further substantiation of this approach is required.

It is unknown at this stage exactly how much mechanical compliance between plasma vessel sections is required at the interface, so although bellows-like structures are shown (similar to the approach used in the connections between the JET vacuum vessel sections [346]), it has not yet been determined whether this is necessary. After this procedure, a full field period is mechanically decoupled from the rest of the torus, and nuclear contamination is controlled via the installation of closure plates and the sustained internal depression within the sector. The module can then be extracted in the next step.

Sector module transport operations. The handling and transport operations of the sector assemblies are intended to be performed using ground-based equipment. This approach avoids the need for very high-capacity cranes and lifting tools, mitigating the risks inherent in performing significant nuclear lifting operations fully remotely in a hazardous environment. Additionally, to avoid dismantling the coil assembly, the complete module assembly will be transported as a single unit. Given that the mass of a single module once the breeder fluid has been drained is predicted to be around 7000 tons, it is impractical to transport using overhead cranes.

Once the closure plates are installed, a ground-based transporter will be positioned to support the sector module assembly and withdraw it from the reactor. The sector interface is designed to simplify the kinematics of extracting a sector assembly, enabling the sector to be withdrawn using a single purely radial translation vector, as shown in the relevant figure. The machine and all interfaces are designed to allow single-sector removal to be kinematically possible without clashes. The sector extraction is showcased in Fig. 53. Once extracted, the sector transporter will transfer the sector to the hot cells along

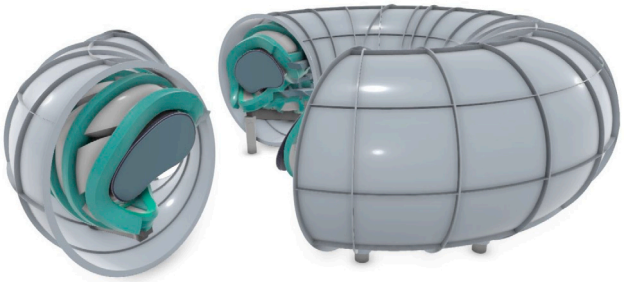

Fig. 53. The device after one sector has been extracted.

existing rails installed in the torus hall and hot cells. In order to sustain the active depression (as well as to provide other services such as power and active cooling), flexible and mobile service connections will need to be provided to the module sector and/or module transporter during transit to the hot cells.

Other steps. Once in the hot cells, the closure plates can be removed, and the in-vessel assemblies can be taken out, with new components installed through the open ends of the plasma vessel. The horizontal openings are approximately 5 m×3 m in size, allowing for the horizontal removal of blanket segments, typically achieved by installing a separate rail system.

In addition to these specific operations to enable and replace the in-vessel systems and components, further parallel operations in other hot cells will be required to manage the disposal of the spent components removed from the reactor. Some expected operations include:

- further system disassembly, cleaning, processing, and possible reconditioning;
- size reduction of components;
- separation of different materials and waste classifications;
- transfer to waste casks/storage containers;
- waste storage to allow further cool-down and reduction in activity;
- transfer to offsite disposal.

An indication of the type of hot cell facility layout that could be used – and a possible logical flow of a module through such a facility – is shown in Fig. 54. This hot cell diagram is intended to give an impression of the facility size and possible floor plan, as well as how the equipment could progress through the facility. A more detailed design study for the hot cell building is required, including further assessment of how separation of 'dirty' and 'clean' equipment will be achieved (for instance, through the use of separate transfer airlocks).

In order to demonstrate commercial viability, a target overall plant availability of 90% has been set, based on an approximate 4.5 year operating cycle. The plant operational lifetime between major maintenance periods is set at four years, which is limited by the accumulated radiation damage to the in-vessel systems. This operating schedule imposes a target on the remote maintenance systems to achieve replacement of the in-vessel components within a five-month window. A provisional, early estimate of the possible overall maintenance duration to replace the in-vessel assemblies, including full replacement of the breeder blankets, has been performed, and a completion time of seven months is estimated. However, this estimate is based on a very early definition of the maintenance activities, sequences, and reactor design concept. It will be refined as the design concept progresses in maturity, and it is expected that opportunities to optimize and reduce the maintenance duration will be identified and leveraged. One major advantage of the sector splitting approach is that the coil assembly and associated support structures can be transported as a single module. This eliminates any disturbance to the coil positioning and alignment within a module, and significantly reduces the amount of realignment required upon reassembly.

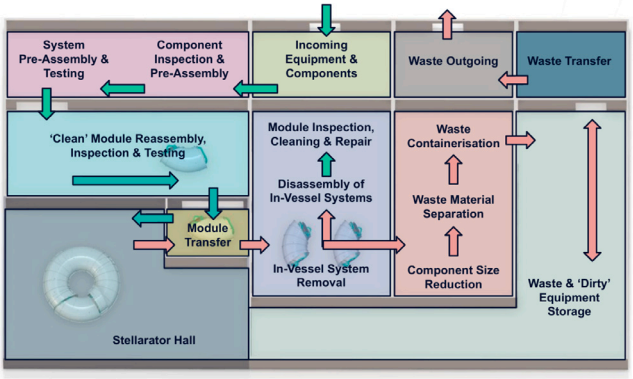

Fig. 54. A schema of a possible hall layout of the stellarator power plant. Green arrows indicate steps for 'usable', still functional components, while red indicators refer to waste or contaminated material.

3. Summary and conclusions

We conclude with a summary of this paper's major findings and suggest further avenues of research, before putting this work into broader context.

3.1. Summary

In this paper, we have introduced a new stellarator concept for fusion power plant applications. The concept is mostly based on (a) advances in stellarator optimization, which allow for higher performance QI stellarator configurations, and (b) modern high-temperature superconductors capable of achieving magnetic field strengths far exceeding those considered in previous reactor studies.

The physics design point proposed in this study provides a maximum of 2.7 GW of fusion energy, which – together with power multiplication in the blanket – results in about 3.1 GW of thermal power for the plant. It is worth noting that the machine presented here will similarly be able to operate at lower total power, though likely at the cost of economic attractiveness. We estimate a required regular maintenance interval of four to six years for scheduled component substitutions, given structural degradation of the first wall.

The analysis performed in this study covers a wide range of relevant physics and engineering aspects, with a far greater coherence than that of any published (modular) stellarator designs or reactor studies conducted up to this point, which often cover only a subset of the overall stellarator. Our physics analysis spans from MHD stability to neoclassical and turbulent transport, and we assess and confirm the resilience of equilibrium properties with respect to relevant plasma profile changes. All physics analyses are performed using the free-boundary VMEC equilibrium. For the first time, we use realistic values of fast particle confinement for the power balance of a stellarator reactor study that are derived from the actual free-boundary plasma equilibrium of the stellarator.

Additional high-fidelity validation efforts, such as electrostatic 'flux-tube' GENE heat flux calculations coupled with the transport code TANGO, indicate that the required peak temperatures in the plasma core can be supported, given a set of assumptions for the edge temperature value. However, the employed GENE-TANGO model is subject to significant uncertainty still and neglects effects such as turbulence stabilization by density profile steepening, electromagnetic effects, and radial electric fields. Significant theoretical uncertainties still exist regarding profile predictions in stellarators, especially when considering effects of density and temperature gradients in the heat flux calculations.

Plasma properties, coil geometries, dimensions, support structures, port locations, and first wall geometries are shared among the different subsystem analyses. This comprehensive approach brings together physics and engineering efforts, providing an unprecedented level of completeness for a stellarator reactor study.

The most challenging aspects of a high-field stellarator reactor concept have been addressed with special care in this paper, including the properties of HTS magnets in terms of critical current density and quench behavior, structural support, and managing strong radiation heat loads resulting from high power density in the plasma. Conceptual designs for the first wall, support structure, and divertor plates have been developed, and feasibility has been demonstrated to the targeted degree of fidelity.

For the first wall, we simulated a net photon load from plasma radiation, taking into account both core radiation and edge radiation as described in Section 2.7, between $0.18\,\mathrm{MW\,m^{-2}}$ and $0.77\,\mathrm{MW\,m^{-2}}$, and thermal analysis predicts temperatures below 500 °C when cooled with pressurized helium.

The chosen liquid lithium-lead based breeding blanket employed in Stellaris is simulated to provide a tritium breeding ratio of about 1.07, potentially sufficient for self-sufficient operation. The blanket concept exploits a liquid breeding material that reduces component complexity in shaped stellarators compared to solid breeders. Additionally, a liquid breeding material can potentially be drained for maintenance applications, drastically easing functional requirements of lifting capabilities of maintenance equipment. The chosen material fraction of the breeding blanket and neutron shield is optimized for sufficient neutron shielding of the cryogenic coils, ensuring both simulated fast neutron fluxes and nuclear heating in the coils stay within reasonable limits. 3D neutronic simulations were employed based on homogenized materials.

Scheduled maintenance is conceptualized to employ the process of sector splitting. Sector splitting for modular stellarators has been suggested in various contexts before, most recently in Ref. [339]. Modular stellarators in particular can benefit from this technique due to their lack of poloidal or helical coils—which would otherwise first need to be removed, as they span around the machine and would hinder the extraction of a sector. For the first time, Stellaris conceptualizes the sector splitting approach for a stellarator reactor, and provides concrete solutions for the splitting interfaces and contamination control. We checked detailed kinematics for a concrete stellarator's geometry with realistic dimensions, and verified that a clash-free extraction of a single sector along a straight path can be achieved.

The support structure in Stellaris uses a combination of strong coil cases, inter-coil support structure elements, and a central support ring. We find that a feasible support structure is possible using a readily-available high-strength cryogenic steel alloy. By simulating peak stresses and expected coil displacements, we show that Stellaris can operate within material limits.

Stellaris employs the island divertor concept for particle and heat exhaust at the edge. Building on recent progress from the W7-X experiment, we aim to achieve a high level of detachment and design the divertor so that a large fraction of the power is radiated in the outermost layers of the plasma. This operational scenario underscores the importance of further research on stable steady-state detachment scenarios in the W7-X stellarator. Higher heat fluxes on divertor plates are foreseen to be transient and to require active detachment and edge radiation control (e.g. by edge impurity seeding).

Assuming that high radiated power fractions can be achieved, this paper has shown that steady-state heat loads on the first wall can be readily managed with a sufficiently sophisticated cooling system.

Additionally, a heating scheme capable of supporting the device at the chosen fusion power design point is identified, consistent with existing efforts to develop high-efficiency electron-cyclotron-resonance heating (ECRH) technology in the frequency range of 240 GHz. We propose injecting microwave beams from the high-field side using the first extra-ordinary (X1) mode, which has the highest cut-off density of

all usually considered ECRH schemes and can heat effectively at the target densities and temperatures.

We simulate the neutron-induced deterioration to reach a peak of 11 DPA per full power year in dedicated regions of the first wall using the ARC-DPA model [265]. Average values are simulated to stay within 6 DPA per full power year at the first wall.

Overall, based on the fidelity of the analysis conducted in this paper, we find the suggested concept to be feasible under all investigated aspects.

3.2. Further improvements and ongoing research

The Stellaris reactor concept presented here is only the first version of a QI stellarator reactor design fully leveraging HTS magnets. The analysis in this paper is meant to demonstrate physics and engineering feasibility to a sufficient extent to motivate further efforts on the QI-HTS stellarator concept. The following is a non-comprehensive list of further studies that would elevate the presented concept:

- in-depth studies of economic viability;
- use of a lower aspect ratio stellarator configuration to optimize economic viability;
- conceptualization of plasma diagnostics solutions aligned with reactor requirements;
- high-fidelity prediction of kinetic profiles and plasma performance evaluations, including electromagnetic effects and impurities;
- investigations of H-mode access in stellarator reactor candidates;
- simulations of flux surface degradation at finite beta, as recently simulated in [118];
- simulations of effects of ECRH heating in X1 mode, particularly examining the impact of heating superthermal and trapped particles as in the current concept;
- density control using cryogenic pellets, including deposition profiles and effects on the device performance;
- full neutronics and structural calculations of a blanket design that is not fully homogenized and includes open ports, including thermal stress analysis and estimation of pumping requirements;
- examination of the maintenance concept, including estimates for the duration of maintenance operations, structural stability simulations during sector extraction, and studies on activation and nuclear containment;
- higher fidelity simulation of fast particle physics, especially including collisional losses and wave-particle scattering between fast particles and Alfvén waves;
- optimization of a Stellaris device to maximize coil tolerances, assessing trade-offs with plasma performance;
- divertor design, to include heat load calculations in attached and detached conditions, active control schemes (including stable detachment steady-state detachment conditions), particle recycling, neutral gas compression, and pumping;
- further tritium blanket analyses, including simulating MHD effects in the PbLi, estimations of corrosion, simulation of tritium transport and a respective TBR target, water activation and safety relevant analyses;
- analysis of ferromagnetic effects of non-magnetic steel, such as EUROFER, and the liquid PbLi blanket on the magnetic field quality;
- high fidelity quench modeling in a detailed HTS coil design in 3D, as opposed to the simplified analysis presented in this study for an initial feasibility assessment.

We note that several of these topics are already under examination by the authors, especially those related to quench modeling and neutronics. Economic aspects – including parasitic electricity consumption and availability – are outside the scope of this paper, but are paramount to assessing the feasibility of a commercial power plant. It is also worth noting that stellarators with lower aspect ratios would potentially require smaller capital costs, though at the expense of overall fusion power. Appendix C shows an example of a stellarator configuration with comparable physics performance to Stellaris, but at a lower aspect ratio.

Multiple models should be developed and compared for all of the above topics, and collaborative efforts between public and private research institutions are recommended to accelerate progress.

3.3. Conclusion

Stellaris is a first-of-a-kind concept for a high-field, QI stellarator fusion power plant. It combines significant physics performance improvements, an integrated and self-consistent engineering feasibility study, and novel concepts for key subsystems and operations. Due to the QI symmetry of the magnetic field, Stellaris is designed to operate as an intrinsically steady-state device without disruptions. While the basic concept of a modular QI stellarator operating in steady-state has already been demonstrated by the W7-X experiment [51], it has only recently become possible to optimize QI stellarator plasma and coil shapes to target reactor viability [71]. The latter requires not only excellent confinement of fusion-born fast particles, but also the feasibility of reactor-relevant magnets and engineering systems.

New stellarator configurations presented in the literature often perform well in one metric but poorly in others. For example, a configuration optimized for good fast particle confinement may not be ideally-MHD stable, or an MHD stable configuration with good fast particle confinement may not be feasible with realistic coils. Until now, no single consistent stellarator reactor study has been presented that fulfills all relevant performance aspects of stellarator configuration simultaneously, including an engineering feasibility analysis that builds credibility for a reactor candidate. This paper aims to address this gap, suggesting a new stellarator concept alongside a broad range of analyses targeted at indicating viability for a power plant prototype.

As part of the Stellaris concept, several novel engineering design solutions are suggested and corresponding analyses have been performed. Of particular relevance are the suggested concepts for high-field HTS magnets, the support structure, and a high power density first wall and blanket system handling tritium breeding and neutron shielding. Additionally, a remote maintenance solution is conceptualized that overcomes the limitations of port-based scheduled maintenance in stellarators—a major challenge on the path to commercial energy production.

The main value of this paper is in showcasing a baseline QI stellarator design for prototypical power plant applications. The authors hope and anticipate that Stellaris will serve as a foundation for further research and development on burning plasma physics, as well as engineering solutions for economically viable fusion power plants.

Given increasing demand for clean energy and heightened investment in fusion technology – including HTS magnets and neutron-resilient materials – QI stellarators are now positioned to play a prominent role in the global race to commercial fusion.

CRediT authorship contribution statement

J. Lion: Writing – original draft, Visualization, Supervision, Software, Methodology, Investigation, Conceptualization. **J.-C. Anglès:** Writing – original draft, Software, Methodology, Conceptualization. **L. Bonauer:** Software. **A. Bañón Navarro:** Software, Methodology. **S.A. Cadena Ceron:** Software. **R. Davies:** Software, Methodology. **M. Drevlak:** Software, Methodology. **N. Foppiani:** Writing – original draft, Visualization, Software, Methodology. **J. Geiger:** Methodology. **A. Goodman:** Methodology. **W. Guo:** Visualization, Methodology. **E.**

Guiraud: Software. **F. Hernández:** Writing – review & editing, Supervision. **S. Henneberg:** Supervision, Methodology. **R. Herrero:** Writing – original draft, Visualization, Software, Methodology. **C. Hintze:** Methodology. **H. Höchter:** Software. **J. Jelonnek:** Writing – review & editing, Investigation. **F. Jenko:** Writing – review & editing, Supervision. **R. Jorge:** Supervision, Methodology. **M. Kaiser:** Software. **M. Kubie:** Writing – review & editing, Supervision, Software, Methodology, Conceptualization. **E. Lascas Neto:** Software, Methodology. **H. Laqua:** Writing – review & editing, Supervision. **M. Leoni:** Writing – original draft, Software, Methodology. **J.F. Lobsien:** Software, Methodology. **V. Maurin:** Writing – original draft, Software, Methodology. **A. Merlo:** Writing – original draft, Visualization, Software, Methodology, Investigation. **D. Middleton-Gear:** Writing – original draft, Visualization, Methodology, Investigation. **M. Pascu:** Software. **G.G. Plunk:** Writing – review & editing, Supervision, Methodology. **N. Riva:** Writing – original draft, Visualization, Software, Methodology, Investigation. **M. Savtchouk:** Software. **F. Sciortino:** Writing – review & editing, Methodology. **J. Schilling:** Writing – review & editing, Visualization, Methodology. **J. Shimwell:** Writing – review & editing, Validation, Investigation. **A. Di Siena:** Supervision, Methodology. **R. Slade:** Writing – review & editing, Methodology, Conceptualization. **T. Stange:** Writing – review & editing, Methodology. **T.N. Todd:** Writing – review & editing, Supervision, Conceptualization. **L. Wegener:** Writing – review & editing, Conceptualization. **F. Wilms:** Software, Methodology. **P. Xanthopoulos:** Supervision, Investigation. **M. Zheng:** Software, Investigation.

Declaration of competing interest

The authors declare the following financial interests/personal relationships which may be considered as potential competing interests: Eduardo Lascas Neto reports financial support was provided by Proxima Fusion GmbH. All Proxima Fusion Co-Authors reports a relationship with Proxima Fusion GmbH that includes: employment and equity or stocks. Martin Kubie, Wei Guo has patent #US63/665,597 pending to Proxima Fusion GmbH. Victor Maurin, Jean-Claude Angles has patent #EP24197718 pending to Proxima Fusion GmbH. Tom Todd, Martin Kubie, David Middleton-Gear, Wei Guo has patent #US63/688,883 pending to Proxima Fusion GmbH. Jorrit Lion, Rodrigo Herrero has patent #EP24197765 pending to Proxima Fusion GmbH. If there are other authors, they declare that they have no known competing financial interests or personal relationships that could have appeared to influence the work reported in this paper.

Acknowledgments

The authors would like to thank Alan Rochford, Fabrice Moncade, Bernhard Auchmann, Chuanren Wu, Felix Schauer, and Nikola Jaksic for their contributions and advice along the way.

We are grateful to Felix Warmer, Cesar Luongo, Craig Beidler, Per Helander, Hartmut Zohm, and Christian Bachmann, for feedback on the draft and their key role in driving the field forward over many years.

We are also thankful to Yasuhiro Suzuki for access and support with the `HINT-3D` code.

We thank all open source developers whose software have enabled this work, particularly the following developer communities: `simsopt`, `OpenMC`, `Gmsh`, `FEniCS-X`, `Open-CASCADE`.

The work presented here was independently funded by Proxima Fusion. Some optimizations and simulations were performed at the Max Planck Computing and Data Facility (Germany). Part of the work was funded by the European Union (EU) via the Euratom Research and Training Programme (Grant Agreement No. 101052200—EUROfusion). A. Goodman is supported by a grant from the Simons Foundation, United States (Grant No. 560651).

Appendix A. Confinement time scaling

For the physics design point exploration performed in Section 2.3, we restrict ourselves to a simple '0.5D' power balance, where the power balance is enforced only globally, after integration of both sides of the power balance equation. We introduce the terminology $p \equiv \langle p \rangle_V \equiv \int_V p dV$, where V is the plasma volume. Then, the integrated steady-state power balance can be written as

$$p_{\text{loss}} \overset{!}{=} p_{\text{heat}}, \tag{A.1}$$

$$\Rightarrow p_{\text{rad}} + p_{\text{conf}} = f_\alpha p_\alpha + p_{\text{aux}}. \tag{A.2}$$

In these equations, p_{loss} is the (volume averaged) loss power density, p_{heat} the heating power density, p_{rad} the loss power density by radiation, p_{conf} the loss power density due to finite confinement, p_{aux} is the auxiliary power density and p_α is the heating power density by fusion alpha particles. f_α is the fraction of the total alpha power absorbed in the plasma. When writing the volume averaged confinement loss power density p_{conf} in terms of the plasma energy density w and the energy confinement time τ_E, we arrive at

$$p_{\text{rad}} + \frac{w}{\tau_E} = f_\alpha E_\alpha n_D n_T \langle \sigma v \rangle_T + p_{\text{aux}}. \tag{A.3}$$

Here, p_{aux} is the auxiliary heating power density. E_α is the energy carried by fast fusion alpha particles (3.5 MeV), n_D and n_T are densities of deuterium and tritium in the plasma respectively. $\langle \sigma v \rangle_T$ is the Maxwellian averaged fusion reactivity.

The radiation term p_{rad} we split in line and continuum radiation, where we use a priori assumed impurity fractions and calculate the cooling factors using the 'Aurora' code [138], relying on the Atomic Data and Analysis Structure (ADAS) database [139]. For synchrotron radiation, we take the model suggested in Ref. [140],

$$p_{\text{sync}} \left[\text{W/m}^{-3}\right] = 1.32 \cdot 10^{-7} \left(B T_e\right)^{2.5} \sqrt{\frac{n_e}{a}} \left(1.0 + \frac{18.0\, a}{R \sqrt{T_e}}\right). \tag{A.4}$$

Here a, R are given in m, T_e in keV, B in T and n_e in 10^{20} m^{-3}.

To resolve the helium fraction f_{He}, one introduces the alpha particle balance equation,

$$\frac{n_{\text{He}}}{\tau_\alpha^\star} = n_D n_T \langle \sigma v \rangle_T, \tag{A.5}$$

and then usually $\tau_\alpha^\star$ is assumed to be proportional to the energy confinement time: $\tau_\alpha^\star = \rho^\star \tau_E$, where we use $\rho^\star \sim 8$, where $\rho^\star$ shall not be confused with the normalized minor plasma radius. Determining reasonable values for $\rho^\star$, and validity of that model in general, is a subject of active research [161,347]. In this article we introduce a new heuristic value f_{suppr} which is used to suppress the resulting helium density by a constant factor,

$$n'_{\text{He}} = f_{\text{suppr}} n_{\text{He}}. \tag{A.6}$$

This assumption is informed by two considerations: first, by suppression of helium ash due to a positive ambipolar radial electric field, and second, by the effect that fast particles do not slow down directly in the core, but are radially displaced due to their finite drift orbit. This effect was quantified in [110] by employing Monte-Carlo slowing down simulations in various stellarators. We capture it here heuristically by choosing a value of $f_{\text{suppr}} = \frac{1}{2}$.

To extrapolate to a reactor, one can use the ISS04 inter-machine scaling, which reads [141]

$$\tau_E = 0.134\, f_{\text{ren}} a^{2.28} B^{0.84} \iota_{2/3}^{0.41} n_{19}^{0.54} R^{0.64} P^{-0.61}. \tag{A.7}$$

where f_{ren} is a multiplier for the ISS04 scaling and the other variables have their usual meanings. Rewriting the heating power P in terms of temperature T, $P = W/\tau_E$, where W is the stored plasma energy, one arrives at

$$\tau_E = 0.152\, f_{\text{ren}}^{2.56} a^{2.72} B^{2.15} \iota_{2/3}^{1.05} n_{19}^{-0.18} R^{0.08} T_{\text{keV}}^{-1.56}, \tag{A.8}$$

which closely resembles the so called 'Gyro-Bohm scaling', which scales as $\tau_{GB} \sim \frac{L}{\rho^2 v_{th}} \sim \frac{a^3 B^2}{T^{3/2}}$. A similar approach was also shown in [348]. Note that this scaling can also be derived from invariance principles of the Maxwell–Vlasov equations [349]. A more careful consideration might retrieve other factors such as sensitivity in aspect ratio and iota [350], $\tau \sim \tau_{GB}\, f(A, \iota)$, but this was not yet retrieved from simulations or data.

Appendix B. First wall simulations

What follows is a brief outline of the method employed to calculate the first wall temperature in Section 2.7.

We estimated the temperature by numerically solving a heat equation with the Finite Element Method (FEM). We solved a steady-state heat equation with two different values for the thermal conductivity k, one for the EUROFER97 steel and one for the tungsten (W):

$$k_{\text{Eurofer}}(T) = 1.103 \times 10^{-7} T^3 - 8.4884 \times 10^{-5} T^2 + 1.0197 \times 10^{-2} T + 31.776\,, \tag{B.1}$$

$$k_W = 108.34 - 1.052 \times 10^{-2}(T + 273.15) + \frac{23\,419.9}{T + 273.15}, \tag{B.2}$$

where the temperature is expressed in Celsius.

The expression for the EUROFER97 conductivity comes from a fit of the experimental data in [251]. The expression for tungsten is from [351]. Both values for k_{Eurofer} and k_{W} are expressed in $\left[\text{W m}^{-1}\,\text{K}^{-1}\right]$.

The governing equations include a volumetric source term representing the neutron load (obtained from the neutronics analysis) and boundary conditions modeling heat input and output: a Neumann boundary condition on the plasma-facing surface prescribing a heat flux equal to the previously computed radiation load (combining edge radiation and core radiation), a homogeneous Neumann boundary condition at the blanket-facing surface, and a Robin boundary condition at the pipes where the heat flux is $-h(T - T_c)$, where T is the unknown temperature, T_c is the temperature of the coolant, and h is the heat transfer coefficient. As detailed in the main text, we considered only a limited portion of the wall: at its sides, we applied a homogeneous Neumann boundary condition. The entire problem then reads

$$\begin{cases} -\nabla \cdot (k(T)\,\nabla T) = f_{nl} & \text{in } \Omega \\ k(T)\,\partial_n T = w_{rl} & \text{on } \Gamma_{\text{pfs}} \\ k(T)\,\partial_n T = 0 & \text{on } \Gamma_{\text{outer}} \\ k(T)\,\partial_n T = 0 & \text{on } \Gamma_{\text{sides}} \\ k(T)\,\partial_n T = -h(T)\,(T - T_c(\vec{x})) & \text{on } \Gamma_{\text{pipes}} \end{cases} \tag{B.3}$$

where k is a piecewise constant function that evaluates to k_{Eurofer} and k_W (Eqs. (B.1) and (B.2)) on the respective subdomains, Ω is the computational domain, Γ_{pfs} is the plasma-facing part of the boundary, Γ_{outer} is the blanket-facing part of the boundary, Γ_{sides} are the lateral walls of the wall sector that we are simulating and Γ_{pipes} is the part of the boundary between the EUROFER97 and the pipes. The value of the heat transfer coefficient can be computed from experimental data. We used the Dittus–Bölter equation, according to which the heat transfer coefficient for Helium is given by [352]

$$h = 0.023\,\frac{k}{d}\left(j\frac{d}{\mu}\right)^{0.8}\left(\mu\frac{c_p}{k}\right)^{0.4}. \tag{B.4}$$

The quantities in Eq. (B.4) refer to the coolant: in our case, Helium. The values and meaning of all relevant thermo-physical properties of Helium and the cooling system are given in Table B.9.

The values listed here are for a temperature of 350 °C at a pressure of 8 MPa, but in the code we implemented temperature-dependence for the thermal conductivity and the dynamic viscosity as

$$\mu(T) = -7.2571 \times 10^{-12}\,T^2 + 4.2094 \times 10^{-8}\,T + 1.9366 \times 10^{-5}, \tag{B.5}$$

$$k(T) = -6.1429 \times 10^{-8}\,T^2 + 3.3172 \times 10^{-4}\,T + 0.15473, \tag{B.6}$$

Table B.9
Thermo-physical properties of Helium at 350 °C and cooling system hydraulic parameters.

Variable	Value
Thermal conductivity, k	$0.2633\,\text{W m}^{-1}\,\text{K}^{-1}$
Hydraulic diameter, d	12 mm
Mass flow, m	0.075 kg/s
Mass flux, j	$j = \frac{m}{d^2}$
Dynamic viscosity, μ	3.33×10^{-5} Pa s
Specific heat, c_p	$5188.7\,\text{J kg}^{-1}\,\text{K}^{-1}$

where the expressions are fits from experimental data from the NIST database [353].

In the Robin boundary condition, the temperature of the coolant cannot be taken as a constant, as this would violate energy conservation in that the energy flowing out of the wall and into the pipes must increase the temperature of the coolant in the pipes. To find the temperature of the coolant along the pipe, we implemented a fixed-point iteration in our solution strategy, in which we first solved for the heat in the first wall with an initial guess of what the final temperature will be at the pipes' outlet and then computed the actual heat Q that flows into each pipe with the calculated solution. We used this value to update the outlet temperature according to the equation

$$Q = m\,c_p(T_{\text{out}} - T_{\text{in}}) \tag{B.7}$$

where T_{in} and T_{out} are a pipe's inlet and outlet temperature. We note that this update must be done for each pipe independently, for the reasons outlined above.

We then iterated the solver and continued until the temperature in the whole domain after two successive solutions had a relative change in the L^2 norm, which is less than a given tolerance (in our case, 10^{-5}).

Having the inlet and outlet temperatures of a pipe does not tell us how the temperature varies along that pipe. Computing this value as a function of the temperature along the pipe is a complex operation, so we instead assumed that the temperature varies linearly along the pipe for simplicity.

For the purpose of this analysis, we developed C++ code based on OpenCASCADE for the CAD design. We used `gmsh` [354] for meshing, and performed a Finite Element Analysis using C++ code based on FEniCS-X [355–358]. Since the geometry is not particularly complex, in all our simulations we used a rather coarse tetrahedral mesh with high-order (3) continuous polynomial elements. Our design for the first wall, like most designs, comprises tiles which are physically separate, meaning we can avoid simulating a full wall in favor of just one column at a time, which is more convenient computationally.

Appendix C. Toward smaller aspect ratios

We encourage the reader to interpret the results in this publication as a high-level 'version 1' of what a QI stellarator fusion power plant may look like. Although economic viability was not a central consideration of the presented concept, at the time of writing it is already evident that more commercially attractive Stellaris designs are possible. Rapid iteration of such concepts is possible due to new computational tools that were partly developed for the present effort, and partly made available by international public research over the recent years.

This paper has described a QI configuration with an aspect ratio A $\simeq$ 10, corresponding to a major radius of $R_0 \simeq 12.5$ m. The major radius could be further reduced if an equivalently- or better-performing configuration at lower aspect ratio could be found. For example, a configuration with aspect ratio 6 and the same minor radius (upon which plasma confinement most directly depends) would result in a major plasma radius of $R_0 \simeq 7.8$ m. On the other hand, such a device would only 3/5 of the fusion power as the Stellaris concept demonstrated here.

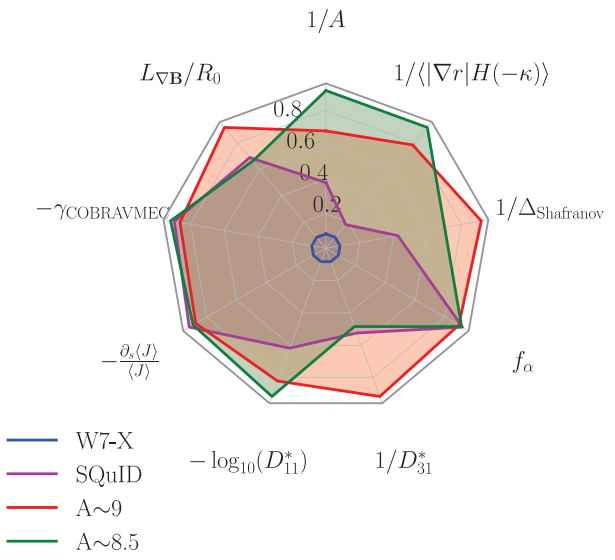

Fig. C.55. Comparison between alternative configurations with reduced aspect ratios from the SQuID family of QI configurations. The reference configuration used throughout the paper is labeled as 'SQuID'. The properties shown here match those presented in Fig. 4, thus indicating normalized quantities where the outermost value is normalized by the best performing configuration and innermost value refers to the worst performing configuration. Here also an ITG-turbulence proxy is shown, following Ref. [71], a proxy used that is expected to correlate with mitigation of ITG turbulence. For this, we compute a flux-surface averaged value of the flux compression $|\nabla r|$ in regions of 'bad' curvature (identified by the drift curvature [78,359], $K_d = \mathbf{B} \times \boldsymbol{\kappa} \cdot \nabla \alpha$). The value at $s = 0.5$ (the approximate location of the strongest temperature gradient) is reported. The spider plot dimensions have been normalized to reflect the best and worst values observed across all shown configurations. This plot focuses on fixed boundary metrics.

To validate the existence of equivalent lower aspect ratio stellarator configurations, in Fig. C.55 we compare the SQuID-configuration used in this paper with alternative plasma configurations at aspect ratios of approximately 9 and 8. These alternative configurations share key features: minimal Shafranov shift, excellent fast particle confinement, reduced bootstrap current, low radial neoclassical transport, and the maximum-J property. Additionally, they are ideal-MHD stable, and allow for sufficiently distant coils.

These stellarator configurations have recently been obtained and verified for engineering feasibility, though not to the same depth and extent as the configuration discussed in this report. Neoclassical transport is found to be slightly higher in the low aspect ratio configurations, though still much lower than in W7-X and well within the bounds considered necessary for a reactor. Ongoing work on physics, engineering, and economic optimization for these new configurations – and others that are certain to emerge in the near future – promises to further accelerate progress.

Appendix D. Mercier criterion

Within this article, to evaluate ideal MHD stability, we adopt the definition of the Mercier criterion used in the VMEC code:

$$
\begin{aligned}
D_{\text{Merc}} &= D_S + D_W + D_I + D_G, \\
D_S &= \frac{(\psi'' \chi')^2}{4} \frac{s}{\iota^2 \pi^2}, \\
D_W &= \frac{s}{\iota^2 \pi^2} \iint \left|\sqrt{g}\right| d\theta\, d\zeta\, \frac{B^2}{g^{ss}} \frac{dp}{ds} \left(V'' - \frac{dp}{ds} \iint \frac{g\, d\theta\, d\zeta}{B^2} \right), \\
D_I &= \frac{s}{\iota^2 \pi^2} \left[\iint \left|\sqrt{g}\right| d\theta\, d\zeta\, \frac{B^2}{g^{ss}} \psi'' I' - (\psi'' \chi') \right. \\
&\qquad \left. \iint \frac{\left|\sqrt{g}\right| (\vec{J} \cdot \vec{B})\, d\theta\, d\zeta}{g^{ss}} \right], \\
D_G &= \frac{s}{\iota^2 \pi^2} \left[\iint \left|\sqrt{g}\right| d\theta\, d\zeta \left(\frac{\vec{J} \cdot \vec{B}}{g^{ss}} \right)^2 \right. \\
&\qquad - \frac{s}{\iota^2 \pi^2} \left(\iint \frac{\left|\sqrt{g}\right| d\theta\, d\zeta\, (\vec{J} \cdot \vec{B})^2}{g^{ss} B^2} \right) \\
&\qquad \left. \left(\iint \frac{\left|\sqrt{g}\right| d\theta\, d\zeta\, B^2}{g^{ss}} \right) \right],
\end{aligned}
\tag{D.1}
$$

where ψ is the toroidal flux, χ is the poloidal flux, s is the normalized toroidal flux, ι is the rotational transform, $g^{ss} = |\nabla s \cdot \nabla s|$, V is the plasma volume, and $\left|\sqrt{g}\right| = (\nabla \psi \cdot \nabla \theta \times \nabla \phi)^{-1}$.

Data availability

Data will be made available on request.

References

[1] J.-Y. Lee, J. Marotzke, G. Bala, L. Cao, S. Corti, J. Dunne, F. Engelbrecht, E. Fischer, J. Fyfe, C. Jones, A. Maycock, J. Mutemi, O. Ndiaye, S. Panickal, T. Zhou, Future global climate: Scenario-based projections and near-term information, in: V. Masson-Delmotte, P. Zhai, A. Pirani, S. Connors, C. Péan, S. Berger, N. Caud, Y. Chen, L. Goldfarb, M. Gomis, M. Huang, K. Leitzell, E. Lonnoy, J. Matthews, T. Maycock, T. Waterfield, O. Yelekçi, R. Yu, B. Zhou (Eds.), Climate Change 2021: The Physical Science Basis. Contribution of Working Group I To the Sixth Assessment Report of the Intergovernmental Panel on Climate Change, Cambridge University Press, Cambridge, United Kingdom and New York, NY, USA, 2021, pp. 553–672, http://dx.doi.org/10.1017/9781009157896.006.

[2] I.C. Change, et al., Mitigation of climate change, in: Contribution of Working Group III to the Fifth Assessment Report of the Intergovernmental Panel on Climate Change, vol. 1454, 2014, p. 147.

[3] A. de Vries, The growing energy footprint of artificial intelligence, Joule 7 (10) (2023) 2191–2194, http://dx.doi.org/10.1016/j.joule.2023.09.004.

[4] G.P. Thiel, A.K. Stark, To decarbonize industry, we must decarbonize heat, Joule 5 (3) (2021) 531–550, http://dx.doi.org/10.1016/j.joule.2020.12.007.

[5] M. Wappler, D. Unguder, X. Lu, H. Ohlmeyer, H. Teschke, W. Lueke, Building the green hydrogen market–Current state and outlook on green hydrogen demand and electrolyzer manufacturing, Int. J. Hydrog. Energy 47 (79) (2022) 33551–33570, http://dx.doi.org/10.1016/j.ijhydene.2022.07.253.

[6] N. Salmon, R. Bañares-Alcántara, Green ammonia as a spatial energy vector: a review, Sustain. Energy Fuels 5 (11) (2021) 2814–2839, http://dx.doi.org/10.1039/d1se00345c.

[7] N. Ghaffour, T.M. Missimer, G.L. Amy, Technical review and evaluation of the economics of water desalination: Current and future challenges for better water supply sustainability, Desalination 309 (2013) 197–207, http://dx.doi.org/10.1016/j.desal.2012.10.015.

[8] R. Hanna, A. Abdulla, Y. Xu, D.G. Victor, Emergency deployment of direct air capture as a response to the climate crisis, Nat. Commun. 12 (1) (2021) 368, http://dx.doi.org/10.1038/s41467-020-20437-0.

[9] C. Bustreo, U. Giuliani, D. Maggio, G. Zollino, How fusion power can contribute to a fully decarbonized European power mix after 2050, Fusion Eng. Des. 146 (2019) 2189–2193, http://dx.doi.org/10.1016/j.fusengdes.2019.03.150.

[10] B. Sorbom, J. Ball, T. Palmer, F. Mangiarotti, J. Sierchio, P. Bonoli, C. Kasten, D. Sutherland, H. Barnard, C. Haakonsen, J. Goh, C. Sung, D. Whyte, ARC: A compact, high-field, fusion nuclear science facility and demonstration power plant with demountable magnets, Fusion Eng. Des. 100 (2015) 378–405, http://dx.doi.org/10.1016/j.fusengdes.2015.07.008.

[11] F. Warmer, S. Torrisi, C.D. Beidler, A. Dinklage, K. Egorov, Y. Feng, J. Geiger, H. Lux, F. Schauer, Y. Turkin, R. Wolf, P. Xanthopoulos, Systems code analysis of HELIAS-type fusion reactor and economic comparison to tokamaks, IEEE Trans. Plasma Sci. 44 (2016) 1576–1585, http://dx.doi.org/10.1109/TPS.2016.2545868.

[12] J. Lion, F. Warmer, H. Wang, C. Beidler, S. Muldrew, R. Wolf, A general stellarator version of the systems code PROCESS, Nucl. Fusion 61 (12) (2021) 126021, http://dx.doi.org/10.1088/1741-4326/ac2dbf.

[13] D. Maisonnier, I. Cook, S. Pierre, B. Lorenzo, G. Luciano, N. Prachai, P. Aldo, P. Team, et al., DEMO and fusion power plant conceptual studies in Europe, Fusion Eng. Des. 81 (8–14) (2006) 1123–1130, http://dx.doi.org/10.1016/j.fusengdes.2005.08.055.

[14] S. Entler, J. Horacek, T. Dlouhy, V. Dostal, Approximation of the economy of fusion energy, Energy 152 (2018) 489–497, http://dx.doi.org/10.1016/j.energy.2018.03.130.

[15] N. Nawal, H. Lux, R. Chapman, J.R. Cowan, Fusion power plant cost modeling uncertainties, IEEE Trans. Plasma Sci. (2024) 1–6, http://dx.doi.org/10.1109/tps.2024.3368623.

[16] M.C. Handley, D. Slesinski, S.C. Hsu, Potential early markets for fusion energy, J. Fusion Energy 40 (2) (2021) 18, http://dx.doi.org/10.1007/s10894-021-00306-4.

[17] S. Geng, An overview of the ITER project, J. Phys. Conf. Ser. 2386 (1) (2022) 012012, http://dx.doi.org/10.1088/1742-6596/2386/1/012012.

[18] H. Wilson, I. Chapman, T. Denton, W. Morris, B. Patel, G. Voss, C. Waldon, the STEP Team, STEP—on the pathway to fusion commercialization, in: Commercialising Fusion Energy, IOP Publishing, 2020, pp. 8–1–8–18, https://doi.org/10.1088/978-0-7503-2719-0ch8.

[19] A.J. Creely, M.J. Greenwald, S.B. Ballinger, D. Brunner, J. Canik, J. Doody, T. Fülöp, D.T. Garnier, R. Granetz, T.K. Gray, C. Holland, N.T. Howard, J.W. Hughes, J.H. Irby, V.A. Izzo, G.J. Kramer, A.Q. Kuang, B. LaBombard, Y. Lin, B. Lipschultz, N.C. Logan, J.D. Lore, E.S. Marmar, K. Montes, R.T. Mumgaard, C. Paz-Soldan, C. Rea, M.L. Reinke, P. Rodriguez-Fernandez, K. Särkimäki, F. Sciortino, S.D. Scott, A. Snicker, P.B. Snyder, B.N. Sorbom, R. Sweeney, R.A. Tinguely, E.A. Tolman, M. Umansky, O. Vallhagen, J. Varje, D.G. Whyte, J.C. Wright, S.J. Wukitch, J. Zhu, Overview of the SPARC tokamak, J. Plasma Phys. 86 (5) (2020) http://dx.doi.org/10.1017/s0022377820001257.

[20] Y. Song, J. Li, Y. Wan, Y. Liu, X. Wang, B. Wan, P. Fu, P. Weng, S. Wu, X. Duan, Q. Yang, K. Feng, Q. Li, M. Ye, G. Zhuang, Y. Liang, X. Gao, C. Chen, H. Wang, G. Zheng, Y. Xu, T. Qian, V. Chan, B. Xiao, K. Lu, J. Zheng, M. Lu, D. Liu, J. Liu, Y. Wu, X. Liu, Y. Shi, B. Hou, C. Liu, J. Ge, C. Zhou, H. Ran, Q. Wang, X. Wang, S. Liu, S. Liu, D. Yao, Y. Cheng, L. Hu, C. Hu, F. Liu, G. Chen, Engineering design of the CFETR machine, Fusion Eng. Des. 183 (2022) 113247, http://dx.doi.org/10.1016/j.fusengdes.2022.113247.

[21] G. Federici, C. Bachmann, L. Barucca, C. Baylard, W. Biel, L. Boccaccini, C. Bustreo, S. Ciattaglia, F. Cismondi, V. Corato, et al., Overview of the DEMO staged design approach in Europe, Nucl. Fusion 59 (6) (2019) 066013, http://dx.doi.org/10.1088/1741-4326/ab1178.

[22] K. Kim, K. Im, H. Kim, S. Oh, J. Park, S. Kwon, Y. Lee, J. Yeom, C. Lee, G. Lee, et al., Design concept of K-DEMO for near-term implementation, Nucl. Fusion 55 (5) (2015) 053027, http://dx.doi.org/10.1088/0029-5515/55/5/053027.

[23] N.W. Eidietis, Prospects for disruption handling in a tokamak-based fusion reactor, Fusion Sci. Technol. 77 (7–8) (2021) 738–744, http://dx.doi.org/10.1080/15361055.2021.1889919.

[24] J. Zhu, C. Rea, R. Granetz, E. Marmar, K. Montes, R. Sweeney, R. Tinguely, D. Chen, B. Shen, B. Xiao, D. Humphreys, J. Barr, O. Meneghini, Scenario adaptive disruption prediction study for next generation burning-plasma tokamaks, Nucl. Fusion 61 (11) (2021) 114005, http://dx.doi.org/10.1088/1741-4326/ac28ae.

[25] B.H. Guo, D.L. Chen, B. Shen, C. Rea, R.S. Granetz, L. Zeng, W.H. Hu, J.P. Qian, Y.W. Sun, B.J. Xiao, Disruption prediction on EAST tokamak using a deep learning algorithm, Plasma Phys. Control. Fusion 63 (11) (2021) 115007, http://dx.doi.org/10.1088/1361-6587/ac228b.

[26] J. Kates-Harbeck, A. Svyatkovskiy, W. Tang, Predicting disruptive instabilities in controlled fusion plasmas through deep learning, Nature 568 (7753) (2019) 526–531, http://dx.doi.org/10.1038/s41586-019-1116-4.

[27] P.L. Taylor, A.G. Kellman, T.E. Evans, D.S. Gray, D.A. Humphreys, A.W. Hyatt, T.C. Jernigan, R.L. Lee, J.A. Leuer, S.C. Luckhardt, P.B. Parks, M.J. Schaffer, D.G. Whyte, J. Zhang, Disruption mitigation studies in DIII-D, Phys. Plasmas 6 (5) (1999) 1872–1879, http://dx.doi.org/10.1063/1.873445.

[28] L. Baylor, T. Jernigan, S. Combs, S. Meitner, J. Caughman, N. Commaux, D. Rasmussen, P. Parks, M. Glugla, S. Maruyama, R. Pearce, M. Lehnen, Disruption-mitigation-technology concepts and implications for ITER, IEEE Trans. Plasma Sci. 38 (3) (2010) 419–424, http://dx.doi.org/10.1109/tps.2009.2039496.

[29] D.G. Whyte, T.C. Jernigan, D.A. Humphreys, A.W. Hyatt, C.J. Lasnier, P.B. Parks, T.E. Evans, M.N. Rosenbluth, P.L. Taylor, A.G. Kellman, D.S. Gray, E.M. Hollmann, S.K. Combs, Mitigation of tokamak disruptions using high-pressure gas injection, Phys. Rev. Lett. 89 (5) (2002) 055001, http://dx.doi.org/10.1103/physrevlett.89.055001.

[30] L. Baylor, S. Meitner, T. Gebhart, J. Caughman, J. Herfindal, D. Shiraki, D. Youchison, Shattered pellet injection technology design and characterization for disruption mitigation experiments, Nucl. Fusion 59 (6) (2019) 066008, http://dx.doi.org/10.1088/1741-4326/ab136c.

[31] A. Dinklage, C.D. Beidler, P. Helander, G. Fuchert, H. Maaßberg, K. Rahbarnia, T. Sunn Pedersen, Y. Turkin, R.C. Wolf, A. Alonso, T. Andreeva, B. Blackwell, S. Bozhenkov, B. Buttenschön, A. Czarnecka, F. Effenberg, Y. Feng, J. Geiger, M. Hirsch, U. Höfel, M. Jakubowski, T. Klinger, J. Knauer, G. Kocsis, A. Krämer-Flecken, M. Kubkowska, A. Langenberg, H.P. Laqua, N. Marushchenko, A. Mollén, U. Neuner, H. Niemann, E. Pasch, N. Pablant, L. Rudischhauser, H.M. Smith, O. Schmitz, T. Stange, T. Szepesi, G. Weir, T. Windisch, G.A. Wurden, D. Zhang, Magnetic configuration effects on the Wendelstein 7-X stellarator, Nat. Phys. 14 (8) (2018) 855–860, http://dx.doi.org/10.1038/s41567-018-0141-9.

[32] U. Stroth, G. Fuchert, M. Beurskens, G. Birkenmeier, P. Schneider, E. Scott, K. Brunner, F. Günzkofer, P. Hacker, O. Kardaun, J. Knauer, K. Rahbarnia, D. Zhang, Stellarator-tokamak energy confinement comparison based on ASDEX upgrade and Wendelstein 7-X hydrogen plasmas, Nucl. Fusion 61 (1) (2020) 016003, http://dx.doi.org/10.1088/1741-4326/abbc4a.

[33] M. Greenwald, Density limits in toroidal plasmas, Plasma Phys. Control. Fusion 44 (8) (2002) R27–R53, http://dx.doi.org/10.1088/0741-3335/44/8/201.

[34] A.H. Boozer, Stellarators as a fast path to fusion, Nucl. Fusion 61 (9) (2021) 096024, http://dx.doi.org/10.1088/1741-4326/ac170f.

[35] L. Giannone, J. Baldzuhn, R. Burhenn, P. Grigull, U. Stroth, F. Wagner, R. Brakel, C. Fuchs, H.J. Hartfuss, K. McCormick, A. Weller, C. Wendland, K. Itoh, S.-I. Itoh, Physics of the density limit in the W7-AS stellarator, Plasma Phys. Control. Fusion 42 (6) (2000) 603–627, http://dx.doi.org/10.1088/0741-3335/42/6/301.

[36] T. Eich, A. Leonard, R. Pitts, W. Fundamenski, R. Goldston, T. Gray, A. Herrmann, A. Kirk, A. Kallenbach, O. Kardaun, A. Kukushkin, B. LaBombard, R. Maingi, M. Makowski, A. Scarabosio, B. Sieglin, J. Terry, A. Thornton, Scaling of the tokamak near the scrape-off layer H-mode power width and implications for ITER, Nucl. Fusion 53 (9) (2013) 093031, http://dx.doi.org/10.1088/0029-5515/53/9/093031.

[37] T. Sunn Pedersen, R. König, M. Jakubowski, M. Krychowiak, D. Gradic, C. Killer, H. Niemann, T. Szepesi, U. Wenzel, A. Ali, G. Anda, J. Baldzuhn, T. Barbui, C. Biedermann, B. Blackwell, H.-S. Bosch, S. Bozhenkov, R. Brakel, S. Brezinsek, J. Cai, B. Cannas, J. Coenen, J. Cosfeld, A. Dinklage, T. Dittmar, P. Drewelow, P. Drews, D. Dunai, F. Effenberg, M. Endler, Y. Feng, J. Fellinger, O. Ford, H. Frerichs, G. Fuchert, Y. Gao, J. Geiger, A. Goriaev, K. Hammond, J. Harris, D. Hathiramani, M. Henkel, Y. Kazakov, A. Kirschner, A. Knieps, M. Kobayashi, G. Kocsis, P. Kornejew, T. Kremeyer, S. Lazerzon, A. LeViness, C. Li, Y. Li, Y. Liang, S. Liu, J. Lore, S. Masuzaki, V. Moncada, O. Neubauer, T. Ngo, J. Oelmann, M. Otte, V. Perseo, F. Pisano, A. Puig Sitjes, M. Rack, M. Rasinski, J. Romazanov, L. Rudischhauser, G. Schlisio, J. Schmitt, O. Schmitz, B. Schweer, S. Sereda, M. Sleczka, Y. Suzuki, M. Vecsei, E. Wang, T. Wauters, S. Wiesen, V. Winters, G. Wurden, D. Zhang, S. Zoletnik, First divertor physics studies in Wendelstein 7-X, Nucl. Fusion 59 (9) (2019) 096014, http://dx.doi.org/10.1088/1741-4326/ab280f.

[38] H. Niemann, P. Drewelow, M.W. Jakubowski, A. Puig Sitjes, B. Cannas, Y. Gao, F. Pisano, R. König, R. Burhenn, P. Hacker, F. Reimold, D. Zhang, K.J. Brunner, J. Knauer, T. Sunn Pedersen, Large wetted areas of divertor power loads at Wendelstein 7-X, Nucl. Fusion 60 (8) (2020) 084003, http://dx.doi.org/10.1088/1741-4326/ab937a.

[39] Y. Feng, M. Kobayashi, T. Lunt, D. Reiter, Comparison between stellarator and tokamak divertor transport, Plasma Phys. Control. Fusion 53 (2) (2011) 024009, http://dx.doi.org/10.1088/0741-3335/53/2/024009.

[40] Y. Feng, Up-scaling the island divertor along the W7-stellarator line, J. Nucl. Mater. 438 (2013) S497–S500, http://dx.doi.org/10.1016/j.jnucmat.2013.01.102.

[41] Y. Feng, C. Beidler, J. Geiger, P. Helander, H. Hölbe, H. Maassberg, Y. Turkin, D. Reiter, On the W7-X divertor performance under detached conditions, Nucl. Fusion 56 (12) (2016) 126011, http://dx.doi.org/10.1088/0029-5515/56/12/126011.

[42] O. Schmitz, Y. Feng, M. Jakubowski, R. König, M. Krychowiak, M. Otte, F. Reimold, T. Barbui, C. Biedermann, S.A. Bozhenkov, S. Brezinsek, B. Buttenschön, K.J. Brunner, P. Drewelow, F. Effenberg, E. Flom, H. Frerichs, O.P. Ford, G. Fuchert, Y. Gao, D. Gradic, O. Grulke, K. Hammond, U. Hergenhahn, U. Höfel, J.P. Knauer, P. Kornejew, T. Kremeyer, H. Niemann, E. Pasch, A. Pavone, V. Perseo, L. Rudischhauser, G. Schlisio, T. Sunn Pedersen, U. Wenzel, V. Winters, G.A. Wurden, D. Zhang, Stable heat and particle flux detachment with efficient particle exhaust in the island divertor of Wendelstein 7-X, Nucl. Fusion (2020) http://dx.doi.org/10.1088/1741-4326/abb51e.

[43] Y. Feng, M. Jakubowski, R. König, M. Krychowiak, M. Otte, F. Reimold, D. Reiter, O. Schmitz, D. Zhang, C. Beidler, C. Biedermann, S. Bozhenkov, K. Brunner, A. Dinklage, P. Drewelow, F. Effenberg, M. Endler, G. Fuchert, Y. Gao, J. Geiger, K. Hammond, P. Helander, C. Killer, J. Knauer, T. Kremeyer, E. Pasch, L. Rudischhauser, G. Schlisio, T. Sunn Pedersen, U. Wenzel, V. Winters, W7-X team, Understanding detachment of the W7-X island divertor, Nucl. Fusion 61 (8) (2021) 086012, http://dx.doi.org/10.1088/1741-4326/ac0772.

[44] S. Gori, W. Lotz, J.J. Nührenberg, Theory of Fusion Plasmas, vol. p. 335, Editrice Compositori, Bologna, 1996.

[45] P. Helander, J. Nührenberg, Bootstrap current and neoclassical transport in quasi-isodynamic stellarators, Plasma Phys. Control. Fusion 51 (5) (2009) 055004, http://dx.doi.org/10.1088/0741-3335/51/5/055004.

[46] P. Helander, J. Geiger, H. Maaßberg, On the bootstrap current in stellarators and tokamaks, Phys. Plasmas 18 (9) (2011) http://dx.doi.org/10.1063/1.3633940.

[47] M. Hirsch, J. Baldzuhn, C. Beidler, R. Brakel, R. Burhenn, A. Dinklage, H. Ehmler, M. Endler, V. Erckmann, Y. Feng, J. Geiger, L. Giannone, G. Grieger, P. Grigull, H.-J. Hartfuß, D. Hartmann, R. Jaenicke, R. König, H.P. Laqua, H. Maaßberg, K. McCormick, F. Sardei, E. Speth, U. Stroth, F. Wagner, A. Weller, A. Werner, H. Wobig, S. Zoletnik, Major results from the stellarator Wendelstein 7-AS, Plasma Phys. Control. Fusion 50 (5) (2008) 053001, http://dx.doi.org/10.1088/0741-3335/50/5/053001.

[48] L. Wegener, Status of Wendelstein 7-X construction, Fusion Eng. Des. 84 (2–6) (2009) 106–112, http://dx.doi.org/10.1016/j.fusengdes.2009.01.106.
[49] R.C. Wolf, et al., Major results from the first plasma campaign of the Wendelstein 7-X stellarator, Nucl. Fusion 57 (10) (2017) 102020, http://dx.doi.org/10.1088/1741-4326/aa770d.
[50] T. Klinger, et al., Overview of first Wendelstein 7-X high-performance operation, Nucl. Fusion 59 (11) (2019) 112004, http://dx.doi.org/10.1088/1741-4326/ab03a7.
[51] C.D. Beidler, et al., Demonstration of reduced neoclassical energy transport in Wendelstein 7-X, Nature 596 (7871) (2021) 221–226, http://dx.doi.org/10.1038/s41586-021-03687-w.
[52] F. Najmabadi, A.R. Raffray, S.I. Abdel-Khalik, L. Bromberg, L. Crosatti, L. El-Guebaly, P.R. Garabedian, A.A. Grossman, D. Henderson, A. Ibrahim, T. Ihli, T.B. Kaiser, B. Kiedrowski, L.P. Ku, J.F. Lyon, R. Maingi, S. Malang, C. Martin, T.K. Mau, B. Merrill, R.L. Moore, R.J.P. Jr., D.A. Petti, D.L. Sadowski, M. Sawan, J.H. Schultz, R. Slaybaugh, K.T. Slattery, G. Sviatoslavsky, A. Turnbull, L.M. Waganer, X.R. Wang, J.B. Weathers, P. Wilson, J.C.W. III, M. Yoda, M. Zarnstorff, The ARIES-CS compact stellarator fusion power plant, Fusion Sci. Technol. 54 (3) (2008) 655–672, http://dx.doi.org/10.13182/FST54-655.
[53] A. Sagara, Y. Igitkhanov, F. Najmabadi, Review of stellarator/heliotron design issues towards MFE DEMO, Fusion Eng. Des. 85 (7–9) (2010) 1336–1341, http://dx.doi.org/10.1016/j.fusengdes.2010.03.041.
[54] A. Sagara, H. Tamura, T. Tanaka, N. Yanagi, J. Miyazawa, T. Goto, R. Sakamoto, J. Yagi, T. Watanabe, S. Takayama, T.F. design group, Helical reactor design FFHR-d1 and c1 for steady-state DEMO, Fusion Eng. Des. 89 (2014) 2114, http://dx.doi.org/10.1016/j.fusengdes.2014.02.076.
[55] C. Beidler, E. Harmeyer, F. Herrnegger, Y. Igitkanov, A. Kendl, J. Kisslinger, Y.I. Kolesnichenko, V. Lutsenko, C. Nührenberg, I. Sidorenko, et al., The HELIAS reactor, in: 16th Int. Conf. Fusion Energy, vol. 3, 1997, pp. 407–418.
[56] H. Wobig, T. Andreeva, C. Beidler, E. Harmeyer, F. Herrnegger, Y. Igitkhanov, J. Kisslinger, Y.I. Kolesnichenko, V. Lutsenko, V. Marchenko, et al., Concept of a Helias ignition experiment, Nucl. Fusion 43 (9) (2003) 889, http://dx.doi.org/10.1088/0029-5515/43/9/313.
[57] T. Andreeva, C.D. Beidler, E. Harmeyer, Y.L. Igitkhanov, Y.I. Kolesnichenko, V.V. Lutsenko, A. Shishkin, F. Herrnegger, J. Kißlinger, H.F. Wobig, The helias reactor concept: comparative analysis of different field period configurations, Fusion Sci. Technol. 46 (2) (2004) 395–400, http://dx.doi.org/10.13182/fst04-a579.
[58] F. Schauer, K. Egorov, V. Bykov, Coil winding pack FE-analysis for a HELIAS reactor, Fusion Eng. Des. 86 (6–8) (2011) 636–639, http://dx.doi.org/10.1016/j.fusengdes.2011.01.058.
[59] F. Schauer, K. Egorov, V. Bykov, HELIAS 5-B magnet system structure and maintenance concept, Fusion Eng. Des. 88 (9–10) (2013) 1619–1622, http://dx.doi.org/10.1016/j.fusengdes.2013.01.035.
[60] F. Warmer, C. Beidler, A. Dinklage, R. Wolf, et al., From W7-X to a HELIAS fusion power plant: motivation and options for an intermediate-step burning-plasma stellarator, Plasma Phys. Control. Fusion 58 (7) (2016) 074006, http://dx.doi.org/10.1088/0741-3335/58/7/074006.
[61] T.S. Pedersen, et al., Confirmation of the topology of the Wendelstein 7-X magnetic field to better than 1:100,000, Nat. Commun. 7 (1) (2016) http://dx.doi.org/10.1038/ncomms13493.
[62] R. Wolf, A. Alonso, S. Äkäslompolo, J. Baldzuhn, M. Beurskens, C. Beidler, C. Biedermann, H.-S. Bosch, S. Bozhenkov, R. Brakel, et al., Performance of Wendelstein 7-X stellarator plasmas during the first divertor operation phase, Phys. Plasmas 26 (8) (2019) http://dx.doi.org/10.1063/1.5098761.
[63] M. Drevlak, J. Geiger, P. Helander, Y. Turkin, Fast particle confinement with optimized coil currents in the W7-X stellarator, Nucl. Fusion 54 (7) (2014) 073002, http://dx.doi.org/10.1088/0029-5515/54/7/073002.
[64] A. Häußler, Computational Approaches for Nuclear Design Analyses of the Stellarator Power Reactor HELIAS, Karlsruhe, 2020, http://dx.doi.org/10.5445/IR/1000124072.
[65] M.N.A. Beurskens, S.A. Bozhenkov, O.P. Ford, P. Xanthopoulos, A. Zocco, Y. Turkin, J. Alonso, C.D. Beidler, I. Calvo, et al., Ion temperature clamping in Wendelstein 7-X electron cyclotron heated plasmas, Nucl. Fusion Accept. (2021) http://dx.doi.org/10.1088/1741-4326/ac1653.
[66] A.B. Navarro, G. Merlo, G. Plunk, P. Xanthopoulos, A. Von Stechow, A. Di Siena, M. Maurer, F. Hindenlang, F. Wilms, F. Jenko, Global gyrokinetic simulations of ITG turbulence in the magnetic configuration space of the Wendelstein 7-X stellarator, Plasma Phys. Control. Fusion 62 (10) (2020) 105005, http://dx.doi.org/10.1088/1361-6587/aba858.
[67] T. Rummel, K. Ribe, G. Ehrke, K. Rummel, A. John, T. Monnich, K.-P. Buscher, W.H. Fietz, R. Heller, O. Neubauer, et al., The superconducting magnet system of the stellarator Wendelstein 7-X, IEEE Trans. Plasma Sci. 40 (3) (2012) 769–776, http://dx.doi.org/10.1109/tps.2012.2184774.
[68] M. Landreman, E. Paul, Magnetic fields with precise quasisymmetry for plasma confinement, Phys. Rev. Lett. 128 (3) (2022) 035001, http://dx.doi.org/10.1103/physrevlett.128.035001.
[69] F. Wechsung, M. Landreman, A. Giuliani, A. Cerfon, G. Stadler, Precise stellarator quasi-symmetry can be achieved with electromagnetic coils, Proc. Natl. Acad. Sci. 119 (13) (2022) http://dx.doi.org/10.1073/pnas.2202084119.
[70] A. Goodman, K.C. Mata, S.A. Henneberg, R. Jorge, M. Landreman, G. Plunk, H. Smith, R. Mackenbach, C. Beidler, P. Helander, Constructing precisely quasi-isodynamic magnetic fields, J. Plasma Phys. 89 (5) (2023) 905890504, http://dx.doi.org/10.1017/s002237782300065x.
[71] A.G. Goodman, P. Xanthopoulos, G.G. Plunk, H. Smith, C. Nührenberg, C.D. Beidler, S.A. Henneberg, G. Roberg-Clark, M. Drevlak, P. Helander, Quasi-isodynamic stellarators with low turbulence as fusion reactor candidates, PRX Energy 3 (2024) 023010, http://dx.doi.org/10.1103/PRXEnergy.3.023010.
[72] E. Sánchez, J. Velasco, I. Calvo, S. Mulas, A quasi-isodynamic configuration with good confinement of fast ions at low plasma β, Nucl. Fusion 63 (6) (2023) 066037, http://dx.doi.org/10.1088/1741-4326/accd82.
[73] J. Kappel, M. Landreman, D. Malhotra, The magnetic gradient scale length explains why certain plasmas require close external magnetic coils, Plasma Phys. Control. Fusion 66 (2) (2024) 025018, http://dx.doi.org/10.1088/1361-6587/ad1a3e.
[74] J. Baldzuhn, H. Damm, C.D. Beidler, K. McCarthy, N. Panadero, C. Biedermann, S.A. Bozhenkov, A. Dinklage, K.J. Brunner, G. Fuchert, Y. Kazakov, M. Beurskens, M. Dibon, J. Geiger, O. Grulke, U. Höfel, T. Klinger, F. Köchl, J. Knauer, G. Kocsis, P. Kornejew, P.T. Lang, A. Langenberg, H. Laqua, N.A. Pablant, E. Pasch, T.S. Pedersen, B. Ploeckl, K. Rahbarnia, G. Schlisio, E.R. Scott, T. Stange, A.V. Stechow, T. Szepesi, Y. Turkin, F. Wagner, V. Winters, G. Wurden, D. Zhang, Enhanced energy confinement after series of pellets in Wendelstein 7-X, Plasma Phys. Control. Fusion 62 (5) (2020) 055012, http://dx.doi.org/10.1088/1361-6587/ab8112.
[75] S. Bozhenkov, Y. Kazakov, O. Ford, M. Beurskens, J. Alcusón, J. Alonso, J. Baldzuhn, C. Brandt, K. Brunner, H. Damm, G. Fuchert, J. Geiger, O. Grulke, M. Hirsch, U. Höfel, Z. Huang, J. Knauer, M. Krychowiak, A. Langenberg, H. Laqua, S. Lazerson, N.B. Marushchenko, D. Moseev, M. Otte, N. Pablant, E. Pasch, A. Pavone, J. Proll, K. Rahbarnia, E. Scott, H. Smith, T. Stange, A. von Stechow, H. Thomsen, Y. Turkin, G. Wurden, P. Xanthopoulos, D. Zhang, R. Wolf, High-performance plasmas after pellet injections in Wendelstein 7-X, Nucl. Fusion 60 (6) (2020) 066011, http://dx.doi.org/10.1088/1741-4326/ab7867.
[76] J. Proll, G. Plunk, B. Faber, T. Görler, P. Helander, I. McKinney, M. Pueschel, H. Smith, P. Xanthopoulos, Turbulence mitigation in maximum-J stellarators with electron-density gradient, J. Plasma Phys. 88 (1) (2022) 905880112, http://dx.doi.org/10.1017/s002237782200006x.
[77] I. García-Cortés, K.J. McCarthy, T. Estrada, V. Tribaldos, D. Medina-Roque, B. van Milligen, E. Ascasíbar, R. Carrasco, A.A. Chmyga, R. García, J. Hernández-Sánchez, C. Hidalgo, A.S. Kozachek, F. Medina, M.A. Ochando, J.L. de Pablos, N. Panadero, I. Pastor, Enhanced confinement induced by pellet injection in the stellarator TJ-II, Phys. Plasmas 30 (7) (2023) http://dx.doi.org/10.1063/5.0151395.
[78] G.T. Roberg-Clark, G.G. Plunk, P. Xanthopoulos, C. Nührenberg, S.A. Henneberg, H.M. Smith, Critical gradient turbulence optimization toward a compact stellarator reactor concept, Phys. Rev. Res. 5 (3) (2023) l032030, http://dx.doi.org/10.1103/physrevresearch.5.l032030.
[79] G. Roberg-Clark, P. Xanthopoulos, G. Plunk, Reduction of electrostatic turbulence in a quasi-helically symmetric stellarator via critical gradient optimization, J. Plasma Phys. 90 (3) (2024) 175900301, http://dx.doi.org/10.1017/s0022377824000382.
[80] S. Stroteich, P. Xanthopoulos, G. Plunk, R. Schneider, Seeking turbulence optimized configurations for the Wendelstein 7-X stellarator: ion temperature gradient and electron temperature gradient turbulence, J. Plasma Phys. 88 (5) (2022) 175880501, http://dx.doi.org/10.1017/s0022377822000757.
[81] P. Kim, S. Buller, R. Conlin, W. Dorland, D.W. Dudt, R. Gaur, R. Jorge, E. Kolemen, M. Landreman, N.R. Mandell, et al., Optimization of nonlinear turbulence in stellarators, J. Plasma Phys. 90 (2) (2024) 905900210, http://dx.doi.org/10.1017/s0022377824000369.
[82] A. Godeke, High temperature superconductors for commercial magnets, Supercond. Sci. Technol. 36 (11) (2023) 113001, http://dx.doi.org/10.1088/1361-6668/acf901.
[83] Z.S. Hartwig, R.F. Vieira, B.N. Sorbom, R.A. Badcock, M. Bajko, W.K. Beck, B. Castaldo, C.L. Craighill, M. Davies, J. Estrada, et al., VIPER: an industrially scalable high-current high-temperature superconductor cable, Supercond. Sci. Technol. 33 (11) (2020) 11LT01, http://dx.doi.org/10.1088/1361-6668/abb8c0.
[84] M.J. Wolf, C. Ebner, W.H. Fietz, R. Heller, D. Nickel, K.-P. Weiss, High temperature superconductors for fusion applications and new developments for the HTS CroCo conductor design, Fusion Eng. Des. 172 (2021) 112739, http://dx.doi.org/10.1016/j.fusengdes.2021.112739.
[85] N. Riva, R. Granetz, R. Vieira, A. Hubbard, A. Pfeiffer, P. Harris, C. Chamberlain, Z. Hartwig, A. Watterson, D. Anderson, et al., Development of the first non-planar REBCO stellarator coil using VIPER cable, Supercond. Sci. Technol. 36 (10) (2023) 105001, http://dx.doi.org/10.1088/1361-6668/aced9d.
[86] R. Dewar, S. Hudson, Stellarator symmetry, Phys. D: Nonlinear Phenom. 112 (1–2) (1998) 275–280, http://dx.doi.org/10.1016/s0167-2789(97)00216-9.
[87] M. Shimada, D. Campbell, V. Mukhovatov, M. Fujiwara, N. Kirneva, K. Lackner, M. Nagami, V. Pustovitov, N. Uckan, J. Wesley, et al., Overview and summary, Nucl. Fusion 47 (6) (2007) S1, http://dx.doi.org/10.1088/0029-5515/47/6/S01.

[88] C. Zhu, S.R. Hudson, Y. Song, Y. Wan, Designing stellarator coils by a modified Newton method using FOCUS, Plasma Phys. Control. Fusion 60 (6) (2018) 065008, http://dx.doi.org/10.1088/1361-6587/aab8c2.

[89] V. Shafranov, L. Zakharov, Use of the virtual-casing principle in calculating the containing magnetic field in toroidal plasma systems, Nucl. Fusion 12 (5) (1972) 599, http://dx.doi.org/10.1088/0029-5515/12/5/009.

[90] D. Malhotra, A.J. Cerfon, M. O'Neil, E. Toler, Efficient high-order singular quadrature schemes in magnetic fusion, Plasma Phys. Control. Fusion 62 (2) (2019) 024004, http://dx.doi.org/10.1088/1361-6587/ab57f4.

[91] G. Grieger, I. Milch, Das fusionsexperiment Wendelstein 7-X, Phys. Blätter 49 (11) (1993) 1001, http://dx.doi.org/10.1002/phbl.19930491106.

[92] A. Subbotin, M. Mikhailov, V. Shafranov, M.Y. Isaev, C. Nührenberg, J. Nührenberg, R. Zille, V. Nemov, S. Kasilov, V. Kalyuzhnyj, et al., Integrated physics optimization of a quasi-isodynamic stellarator with poloidally closed contours of the magnetic field strength, Nucl. Fusion 46 (11) (2006) 921, http://dx.doi.org/10.1088/0029-5515/46/11/006.

[93] M.I. Mikhailov, V.D. Shafranov, J. Nührenberg, Pressure insensitivity of a high-β quasi-isodynamic stellarator, Plasma Phys. Rep. 35 (7) (2009) 529–534, http://dx.doi.org/10.1134/s1063780x09070010.

[94] M. Drevlak, C. Beidler, J. Geiger, P. Helander, Y. Turkin, Quasi-isodynamic configuration with improved confinement, in: 41st EPS Conference on Plasma Physics, 2014.

[95] S. Hirshman, Steepest-descent moment method for three-dimensional magnetohydrodynamic equilibria, Phys. Fluids 26 (12) (1983) 3553, http://dx.doi.org/10.1063/1.864116.

[96] T. Andreeva, Vacuum Magnetic Configurations of Wendelstein 7-X, IPP Report IPP III/270, Max-Planck-Institut für Plasmaphysik, 2002, URL https://pure.mpg.de/rest/items/item_2138236/component/file_2138235/content.

[97] C.G. Albert, S.V. Kasilov, W. Kernbichler, Accelerated methods for direct computation of fusion alpha particle losses within, stellarator optimization, J. Plasma Phys. 86 (2) (2020-03) http://dx.doi.org/10.1017/s0022377820000203.

[98] C.G. Albert, S.V. Kasilov, W. Kernbichler, Symplectic integration with non-canonical quadrature for guiding-center orbits in magnetic confinement devices, J. Comput. Phys. 403 (2020) 109065, http://dx.doi.org/10.1016/j.jcp.2019.109065.

[99] J.L. Velasco, I. Calvo, E. Sánchez, F. Parra, Robust stellarator optimization via flat mirror magnetic fields, Nucl. Fusion 63 (12) (2023) 126038, http://dx.doi.org/10.1088/1741-4326/acfe8a.

[100] P. Helander, Theory of plasma confinement in non-axisymmetric magnetic fields, Rep. Progr. Phys. 77 (8) (2014) 087001, http://dx.doi.org/10.1088/0034-4885/77/8/087001.

[101] E. Rodríguez, R. Mackenbach, Trapped-particle precession and modes in quasisymmetric stellarators and tokamaks: a near-axis perspective, J. Plasma Phys. 89 (5) (2023) 905890521, http://dx.doi.org/10.1017/s0022377823001125.

[102] E. Rodriguez, P. Helander, A. Goodman, The maximum-j property in quasi-isodynamic stellarators, J. Plasma Phys. 90 (2) (2024) 905900212, http://dx.doi.org/10.1017/S0022377824000345.

[103] J.H.E. Proll, P. Helander, J.W. Connor, G.G. Plunk, Resilience of quasi-isodynamic stellarators against trapped-particle instabilities, Phys. Rev. Lett. 108 (24) (2012) 245002, http://dx.doi.org/10.1103/physrevlett.108.245002.

[104] P. Helander, J.H.E. Proll, G.G. Plunk, Collisionless microinstabilities in stellarators. I. Analytical theory of trapped-particle modes, Phys. Plasmas 20 (12) (2013) http://dx.doi.org/10.1063/1.4846818.

[105] J.H.E. Proll, P. Xanthopoulos, P. Helander, Collisionless microinstabilities in stellarators. II. Numerical simulations, Phys. Plasmas 20 (12) (2013) 122506, http://dx.doi.org/10.1063/1.4846835.

[106] C. Beidler, K. Allmaier, M. Isaev, S. Kasilov, W. Kernbichler, G. Leitold, H. Maaßberg, D. Mikkelsen, S. Murakami, M. Schmidt, D. Spong, V. Tribaldos, A. Wakasa, Benchmarking of the mono-energetic transport coefficients—results from the international collaboration on neoclassical transport in stellarators (ICNTS), Nucl. Fusion 51 (7) (2011) 076001, http://dx.doi.org/10.1088/0029-5515/51/7/076001.

[107] M. Landreman, H.M. Smith, A. Mollén, P. Helander, Comparison of particle trajectories and collision operators for collisional transport in nonaxisymmetric plasmas, Phys. Plasmas 21 (4) (2014) http://dx.doi.org/10.1063/1.4870077.

[108] E.L. Neto, R. Jorge, C. Beidler, J. Lion, Electron root optimisation for stellarator reactor designs, 2024, arXiv preprint arXiv:2405.12058.

[109] R. Sanchez, S. Hirshman, H. Wong, Improved magnetic coordinate representation for ideal ballooning stability calculations with the COBRA code, Comput. Phys. Comm. 135 (1) (2001) 82–92, http://dx.doi.org/10.1016/s0010-4655(00)00225-3.

[110] J. Lion, Systems Code Models for Stellarator Fusion Power Plants and Application to Stellarator Optimisation (Ph.D. thesis), Technische Universitaet Berlin (Germany), 2023, http://dx.doi.org/10.14279/depositonce-18188.

[111] Y. Turkin, C.D. Beidler, H. Maaßberg, S. Muakami, V. Tribaldos, Neoclassical transport simulations for stellarators, Phys. Plasmas 18 (2011) 022505, http://dx.doi.org/10.1063/1.3553025.

[112] J.M. Greene, J.L. Johnson, Stability criterion for arbitrary hydromagnetic equilibria, Phys. Rev. Lett. 7 (11) (1961) 401, http://dx.doi.org/10.1063/1.1706651.

[113] C. Mercier, Critère de stabilité d'un système toroïdal hydromagnétique en pression scalaire, Nucl. Fusion Suppl. 2 (1962) 801.

[114] C. Mercier, Equilibrium and stability of a toroidal magnetohydrodynamic system in the neighbourhood of a magnetic axis, Nucl. Fusion 4 (3) (1964) 213–226, http://dx.doi.org/10.1088/0029-5515/4/3/008.

[115] F. Bauer, O. Betancourt, P. Garabedian, Magnetohydrodynamic Equilibrium and Stability of Stellarators, Springer Science & Business Media, 2012.

[116] M. Fujiwara, K. Kawahata, N. Ohyabu, O. Kaneko, A. Komori, H. Yamada, N. Ashikawa, L. Baylor, S. Combs, P. deVries, M. Emoto, A. Ejiri, P. Fisher, H. Funaba, M. Goto, D. Hartmann, K. Ida, H. Idei, S. Iio, K. Ikeda, S. Inagaki, N. Inoue, M. Isobe, S. Kado, K. Khlopenkov, T. Kobuchi, A. Krasilnikov, S. Kubo, R. Kumazawa, F. Leuterer, Y. Liang, J. Lyon, S. Masuzaki, T. Minami, J. Miyajima, T. Morisaki, S. Morita, S. Murakami, S. Muto, T. Mutoh, Y. Nagayama, N. Nakajima, Y. Nakamura, H. Nakanishi, K. Narihara, K. Nishimura, N. Noda, T. Notake, S. Ohdachi, Y. Oka, S. Okajima, M. Okamoto, M. Osakabe, T. Ozaki, R. Pavlichenko, B. Peterson, A. Sagara, K. Saito, S. Sakakibara, R. Sakamoto, H. Sanuki, H. Sasao, M. Sasao, K. Sato, M. Sato, T. Seki, T. Shimozuma, M. Shoji, H. Sugama, H. Suzuki, M. Takechi, Y. Takeiri, N. Tamura, K. Tanaka, K. Toi, T. Tokuzawa, Y. Torii, K. Tsumori, K. Watanabe, T. Watanabe, T. Watari, I. Yamada, S. Yamaguchi, S. Yamamoto, M. Yokoyama, N. Yoshida, Y. Yoshimura, Y. Zhao, R. Akiyama, K. Haba, M. Iima, J. Kodaira, T. Takita, T. Tsuzuki, K. Yamauchi, H. Yonezu, H. Chikaraishi, S. Hamaguchi, S. Imagawa, N. Inoue, A. Iwamoto, S. Kitagawa, Y. Kubota, R. Maekawa, T. Mito, K. Murai, A. Nishimura, H. Chikaraishi, K. Takahata, H. Tamura, S. Yamada, N. Yanagi, K. Itoh, K. Matsuoka, K. Ohkubo, I. Ohtake, S. Satoh, T. Satow, S. Sudo, S. Tanahashi, K. Yamazaki, Y. Hamada, O. Motojima, Overview of LHD experiments, Nucl. Fusion 41 (10) (2001) 1355–1367, http://dx.doi.org/10.1088/0029-5515/41/10/305.

[117] A. Weller, J. Geiger, A. Werner, M.C. Zarnstorff, C. Nührenberg, E. Sallander, J. Baldzuhn, R. Brakel, R. Burhenn, A. Dinklage, E. Fredrickson, F. Gadelmeier, L. Giannone, P. Grigull, D. Hartmann, R. Jaenicke, S. Klose, J.P. Knauer, A. Könies, Y.I. Kolesnichenko, H.P. Laqua, V.V. Lutsenko, K. McCormick, D. Monticello, M. Osakabe, E. Pasch, A. Reiman, N. Rust, D.A. Spong, F. Wagner, Y.V. Yakovenko, W. Team, NBI-Group, Experiments close to the beta-limit in W7-AS, Plasma Phys. Control. Fusion 45 (12A) (2003) A285, http://dx.doi.org/10.1088/0741-3335/45/12a/019.

[118] R. Ramasamy, K. Aleynikova, N. Nikulsin, F. Hindenlang, I. Holod, E. Strumberger, M. Hölzl, Nonlinear MHD modeling of soft β limits in W7-AS, Nucl. Fusion (2024) http://dx.doi.org/10.1088/1741-4326/ad56a1.

[119] A. Weller, S. Sakakibara, K.Y. Watanabe, K. Toi, J. Geiger, M.C. Zarnstorff, S.R. Hudson, A. Reiman, A. Werner, C. Nührenberg, S. Ohdachi, Y. Suzuki, H. Yamada, Significance of MHD effects in stellarator confinement, Fusion Sci. Technol. 50 (2) (2006) 158–170, http://dx.doi.org/10.13182/fst06-a1231.

[120] A. Reiman, M. Zarnstorff, D. Monticello, J. Krommes, A. Weller, J. Geiger, W7-AS Team, et al., Localized breaking of flux surfaces and the equilibrium β limit in the W7AS stellarator, in: 21st IAEA Fusion Energy Conference, International Atomic Energy Agency, 2007.

[121] Y. Suzuki, Effect of pressure profile on stochasticity of magnetic field in a conventional stellarator, Plasma Phys. Control. Fusion 62 (10) (2020) 104001, http://dx.doi.org/10.1088/1361-6587/ab9a13.

[122] A.H. Reiman, Pressure-driven stochastization of flux surfaces in stellarator equilibria: a review of the experimental observations and their analysis, Plasma Phys. Control. Fusion 63 (5) (2021) 054002, http://dx.doi.org/10.1088/1361-6587/abf091.

[123] X.-Q. Wang, Y. Xu, A. Shimizu, M. Isobe, S. Okamura, Y. Todo, H. Wang, H. Liu, J. Huang, X. Zhang, et al., The three-dimensional equilibrium with magnetic islands and MHD instabilities in the CFQS quasi-axisymmetric stellarator, Nucl. Fusion 61 (3) (2021) 036021, http://dx.doi.org/10.1088/1741-4326/abd3ec.

[124] A. Knieps, Y. Liang, Y. Suzuki, T. Andreeva, P. Drews, Y. Gao, J. Geiger, O. Grulke, K.-P. Hollfeld, M. Jakubowski, et al., Changes in the edge magnetic field of Wendelstein 7-X in high-beta plasmas, in: 47th EPS Conference on Plasma Physics, European Physical Society, 2021.

[125] Y. Suzuki, N. Nakajima, K. Watanabe, Y. Nakamura, T. Hayashi, Development and application of HINT2 to helical system plasmas, Nucl. Fusion 46 (11) (2006) L19, http://dx.doi.org/10.1088/0029-5515/46/11/l01.

[126] Y. Suzuki, HINT modeling of three-dimensional tokamaks with resonant magnetic perturbation, Plasma Phys. Control. Fusion 59 (5) (2017) 054008, http://dx.doi.org/10.1088/1361-6587/aa5adc.

[127] T. Pütterich, R. Dux, V. Bobkov, S. Marsen, R. Neu, M. Sertoli, M. Beurskens, K. Lawson, J. Mailloux, M.L. Mayoral, A. Meigs, F. Rimini, M. Stamp, S. Brezinsek, J.W. Coenen, M. Lehnen, S. Wiesen, J. Bucalossi, E. Joffrin, I. Coffey, A. Czarnecka, E. De la Luna, G. Van Rooij, Tungsten screening and impurity control in JET, 2012.

[128] S. Buller, H. Smith, P. Helander, A. Mollén, S. Newton, I. Pusztai, Collisional transport of impurities with flux-surface varying density in stellarators, J. Plasma Phys. 84 (4) (2018) 905840409, http://dx.doi.org/10.1017/s0022377818000867.

[129] I. Calvo, F.I. Parra, J.L. Velasco, J.A. Alonso, J. García-Regaña, Stellarator impurity flux driven by electric fields tangent to magnetic surfaces, Nucl. Fusion 58 (12) (2018) 124005, http://dx.doi.org/10.1088/1741-4326/aae8a1.

[130] P. Helander, A. Goodman, C. Beidler, M. Kuczynski, H. Smith, Optimised stellarators with a positive radial electric field, J. Plasma Phys. 90 (6) (2024) 175900602, http://dx.doi.org/10.1017/S0022377824001004.
[131] S. Sudo, Y. Takeiri, H. Zushi, F. Sano, K. Itoh, K. Kondo, A. Iiyoshi, Scalings of energy confinement and density limit in stellarator/heliotron devices, Nucl. Fusion 30 (1) (1990) 11, http://dx.doi.org/10.1088/0029-5515/30/1/002.
[132] A.B. Navarro, A. Di Siena, J.L. Velasco, F. Wilms, G. Merlo, T. Windisch, L. LoDestro, J.B. Parker, F. Jenko, First-principles based plasma profile predictions for optimized stellarators, Nucl. Fusion 63 (5) (2023) 054003, http://dx.doi.org/10.1088/1741-4326/acc3af.
[133] F. Wilms, A.B. Navarro, G. Merlo, L. Leppin, T. Görler, T. Dannert, F. Hindenlang, F. Jenko, Global electromagnetic turbulence simulations of W7-X-like plasmas with GENE-3D, J. Plasma Phys. 87 (6) (2021) 905870604, http://dx.doi.org/10.1017/s0022377821001082.
[134] A. Bañón Navarro, G. Roberg-Clark, G. Plunk, D. Fernando, A. Di Siena, F. Wilms, F. Jenko, Assessing core ion thermal confinement in critical-gradient-optimized stellarators, Phys. Plasmas 31 (6) (2024) http://dx.doi.org/10.1063/5.0204597.
[135] O.P. Ford, M.N. Beurskens, S.A. Bozhenkov, S.A. Lazerson, L. Vano, A. Alonso, J. Baldzuhn, C.D. Beidler, C. Biedermann, R. Burhenn, et al., Turbulence-reduced high-performance scenarios in Wendelstein 7-X, Nucl. Fusion (2024) http://dx.doi.org/10.1088/1741-4326/ad5e99.
[136] F. Warmer, C.D. Beidler, A. Dinklage, K. Egorov, Y. Feng, J. Geiger, F. Schauer, Y. Turkin, R. Wolf, P. Xanthopoulos, HELIAS module development for systems codes, Fusion Eng. Des. 91 (2014) 60, http://dx.doi.org/10.1016/j.fusengdes.2014.12.028.
[137] H.-S. Bosch, G.M. Hale, Improved formulas for fusion cross-sections and thermal reactivities, Nucl. Fusion 32 (1992) 611, http://dx.doi.org/10.1088/0029-5515/32/4/i07.
[138] F. Sciortino, T. Odstrčil, A. Cavallaro, S. Smith, O. Meneghini, R. Reksoatmodjo, O. Linder, J. Lore, N. Howard, E. Marmar, et al., Modeling of particle transport, neutrals and radiation in magnetically-confined plasmas with Aurora, Plasma Phys. Control. Fusion 63 (11) (2021) 112001, http://dx.doi.org/10.1088/1361-6587/ac2890.
[139] H. Summers, W. Dickson, M. O'mullane, N.R. Badnell, A. Whiteford, D. Brooks, J. Lang, S. Loch, D. Griffin, Ionization state, excited populations and emission of impurities in dynamic finite density plasmas: I. The generalized collisional–radiative model for light elements, Plasma Phys. Control. Fusion 48 (2) (2006) 263, http://dx.doi.org/10.1088/0741-3335/48/2/007.
[140] H. Zohm, On the use of high magnetic field in reactor grade tokamaks, J. Fusion Energy 38 (2019) 3–10, http://dx.doi.org/10.1007/s10894-018-0177-y.
[141] H. Yamada, J. Harris, A. Dinklage, E. Ascasibar, F. Sano, S. Okamura, J. Talmadge, U. Stroth, A. Kus, S. Murakami, M. Yokoyama, C. Beidler, V. Tribaldos, K. Watanabe, Y. Suzuki, Characterization of energy confinement in net-current free plasmas using the extended international stellarator database, Nucl. Fusion 45 (12) (2005) 1684–1693, http://dx.doi.org/10.1088/0029-5515/45/12/024.
[142] N. Uckan, J. Tolliver, W. Houlberg, S. Attenberger, Influence of fast alpha diffusion and thermal alpha buildup on tokamak reactor performance, Fusion Technol. 13 (3) (1988) 411–422, http://dx.doi.org/10.13182/fst88-a25117.
[143] G. Fuchert, K. Brunner, K. Rahbarnia, T. Stange, D. Zhang, J. Baldzuhn, S. Bozhenkov, C. Beidler, M. Beurskens, S. Brezinsek, R. Burhenn, H. Damm, A. Dinklage, Y. Feng, P. Hacker, M. Hirsch, Y. Kazakov, J. Knauer, A. Langenberg, H. Laqua, S. Lazerson, N. Pablant, E. Pasch, F. Reimold, T.S. Pedersen, E. Scott, F. Warmer, V. Winters, R. Wolf, Increasing the density in Wendelstein 7-X: benefits and limitations, Nucl. Fusion 60 (3) (2020) 036020, http://dx.doi.org/10.1088/1741-4326/ab6d40.
[144] M. Zanini, H. Laqua, H. Thomsen, T. Stange, C. Brandt, H. Braune, K.J. Brunner, G. Fuchert, M. Hirsch, J. Knauer, et al., ECCD-induced sawtooth crashes at W7-X, Nucl. Fusion 60 (10) (2020) 106021, http://dx.doi.org/10.1088/1741-4326/aba72b.
[145] F. Jenko, W. Dorland, G. Hammett, Critical gradient formula for toroidal electron temperature gradient modes, Phys. Plasmas 8 (9) (2001) 4096–4104, http://dx.doi.org/10.1063/1.1391261.
[146] J.B. Parker, L.L. LoDestro, D. Told, G. Merlo, L.F. Ricketson, A. Campos, F. Jenko, J.A. Hittinger, Bringing global gyrokinetic turbulence simulations to the transport timescale using a multiscale approach, Nucl. Fusion 58 (5) (2018) 054004, http://dx.doi.org/10.1088/1741-4326/aab5c8.
[147] J.B. Parker, L.L. LoDestro, A. Campos, Investigation of a multiple-timescale turbulence-transport coupling method in the presence of random fluctuations, Plasma 1 (1) (2018) 126–143, http://dx.doi.org/10.3390/plasma1010012.
[148] A. Di Siena, A.B. Navarro, T. Luda, G. Merlo, M. Bergmann, L. Leppin, T. Görler, J. Parker, L. LoDestro, T. Dannert, et al., Global gyrokinetic simulations of ASDEX upgrade up to the transport timescale with GENE–Tango, Nucl. Fusion 62 (10) (2022) 106025, http://dx.doi.org/10.1088/1741-4326/ac8941.
[149] S.A. Lazerson, A. LeViness, J. Lion, Simulating fusion alpha heating in a stellarator reactor, Plasma Phys. Control. Fusion 63 (12) (2021) 125033, http://dx.doi.org/10.1088/1361-6587/ac35ee.
[150] A. Di Siena, R. Bilato, A.B. Navarro, M. Bergmann, L. Leppin, T. Görler, E. Poli, M. Weiland, G. Tardini, F. Jenko, et al., Impact of supra-thermal particles on plasma performance at ASDEX upgrade with GENE-Tango simulations, Nucl. Fusion 64 (6) (2024) 066020, http://dx.doi.org/10.1088/1741-4326/ad4168.
[151] F. Wilms, A. Banon Navarro, T. Windisch, S.A. Bozhenkov, F. Warmer, G. Fuchert, O. Ford, D. Zhang, T. Stange, F. Jenko, Global gyrokinetic analysis of Wendelstein 7-X discharge: unveiling the importance of trapped-electron-mode and electron-temperature-gradient turbulence, Nucl. Fusion (2024) http://dx.doi.org/10.1088/1741-4326/ad6675.
[152] V. Erckmann, F. Wagner, J. Baldzuhn, R. Brakel, R. Burhenn, U. Gasparino, P. Grigull, H. Hartfuss, J. Hofmann, R. Jaenicke, et al., H mode of the W 7-AS stellarator, Phys. Rev. Lett. 70 (14) (1993) 2086, http://dx.doi.org/10.1103/PhysRevLett.70.2086.
[153] F. Wagner, J. Baldzuhn, R. Brakel, R. Burhenn, V. Erckmann, T. Estrada, P. Grigull, H.J. Hartfuss, G. Herre, M. Hirsch, J.V. Hofmann, R. Jaenicke, A. Rudyj, U. Stroth, A. Weller, H-mode of W7-AS stellarator, Plasma Phys. Control. Fusion 36 (7A) (1994) A61–A74, http://dx.doi.org/10.1088/0741-3335/36/7a/006.
[154] Y. Martin, T. Takizuka, et al., Power requirement for accessing the H-mode in ITER, J. Phys. Conf. Ser. 123 (1) (2008) 012033, http://dx.doi.org/10.1088/1742-6596/123/1/012033.
[155] K. Tanaka, M. Nakata, Y. Ohtani, T. Tokuzawa, H. Yamada, F. Warmer, M. Nunami, S. Satake, T. Tala, T. Tsujimura, et al., Extended investigations of isotope effects on ECRH plasma in LHD, Plasma Phys. Control. Fusion 62 (2) (2019) 024006, http://dx.doi.org/10.1088/1361-6587/ab5bae.
[156] K. Tanaka, K. Nagaoka, K. Ida, H. Yamada, T. Kobayashi, S. Satake, M. Nakata, T. Kinoshita, Y. Ohtani, T. Tokuzawa, et al., Isotope effects on transport in LHD, Plasma Phys. Control. Fusion 63 (9) (2021) 094001, http://dx.doi.org/10.1088/1361-6587/abffb6.
[157] S. Kaye, M. Greenwald, U. Stroth, O. Kardaun, A. Kus, D. Schissel, J. DeBoo, G. Bracco, K. Thomsen, J. Cordey, et al., ITER L mode confinement database, Nucl. Fusion 37 (9) (1997) 1303, http://dx.doi.org/10.1088/0029-5515/37/9/i10.
[158] C.F. Maggi, H. Weisen, J.C. Hillesheim, A. Chankin, E. Delabie, L. Horvath, F. Auriemma, I.S. Carvalho, G. Corrigan, J. Flanagan, L. Garzotti, D. Keeling, D. King, E. Lerche, R. Lorenzini, M. Maslov, S. Menmuir, S. Saarelma, A.C.C. Sips, E.R. Solano, E. Belonohy, F.J. Casson, C. Challis, C. Giroud, V. Parail, C. Silva, M. Valisa, Isotope effects on L-H threshold and confinement in tokamak plasmas, Plasma Phys. Control. Fusion 60 (1) (2017) 014045, http://dx.doi.org/10.1088/1361-6587/aa9901.
[159] P. Xanthopoulos, S.A. Bozhenkov, M.N.A. Beurskens, H.M. Smith, G.G. Plunk, P. Helander, C.D. Beidler, J.A. Alcusón, A. Alonso, A. Dinklage, O. Ford, G. Fuchert, J. Geiger, J.H.E. Proll, M.J. Pueschel, Y. Turkin, F. Warmer, t.W.-X. Team, Turbulence mechanisms of enhanced performance stellarator plasmas, Phys. Rev. Lett. 125 (2020) 075001, http://dx.doi.org/10.1103/PhysRevLett.125.075001.
[160] T. Romba, F. Reimold, R. Jaspers, O. Ford, L. Vanó, T. Klinger, et al., Suppression of anomalous impurity transport in NBI-heated W7-X plasmas, Nucl. Fusion 63 (7) (2023) 076023, http://dx.doi.org/10.1088/1741-4326/acd5e1.
[161] H. Thienpondt, J. García-Regaña, I. Calvo, J. Alonso, J. Velasco, A. González-Jerez, M. Barnes, K. Brunner, O. Ford, G. Fuchert, et al., Prevention of core particle depletion in stellarators by turbulence, Phys. Rev. Res. 5 (2) (2023) L022053, http://dx.doi.org/10.1103/physrevresearch.5.l022053.
[162] P. Helander, A. Zocco, Quasilinear particle transport from gyrokinetic instabilities in general magnetic geometry, Plasma Phys. Control. Fusion 60 (8) (2018) 084006, http://dx.doi.org/10.1088/1361-6587/aac8b7.
[163] S. Sereda, S. Brezinsek, E. Wang, T. Barbui, R. Brakel, B. Buttenschön, A. Goriaev, U. Hergenhahn, U. Höfel, M. Jakubowski, et al., Impact of boronizations on impurity sources and performance in Wendelstein 7-X, Nucl. Fusion 60 (8) (2020) 086007, http://dx.doi.org/10.1088/1741-4326/ab937b.
[164] R. Lunsford, C. Killer, A. Nagy, D. Gates, T. Klinger, A. Dinklage, G. Satheeswaran, G. Kocsis, S. Lazerson, F. Nespoli, et al., Characterization of injection and confinement improvement through impurity induced profile modifications on the Wendelstein 7-X stellarator, Phys. Plasmas 28 (8) (2021) http://dx.doi.org/10.1063/5.0047274.
[165] K. McCarthy, S.K. Combs, L.R. Baylor, J. Caughman, D.T. Fehling, C.R. Foust, J.M. McGill, J. Carmona, D.A. Rasmussen, A compact flexible pellet injector for the TJ-II stellarator, Rev. Sci. Instrum. 79 (10) (2008) http://dx.doi.org/10.1063/1.2955706.
[166] I. Vinyar, A. Geraud, M. Wyman, L. Dequan, A. Lukin, A. Umov, S. Skoblikov, P. Reznichenko, Pellet injectors developed at PELIN for JET, TAE and HL-2A, Fusion Eng. Des. 86 (9–11) (2011) 2208–2211, http://dx.doi.org/10.1016/j.fusengdes.2011.03.108.
[167] S.K. Combs, C.R. Foust, J.M. McGill, J. Caughman, K. McCarthy, L.R. Baylor, M. Chamorro, D.T. Fehling, R. Garciab, J.H. Harris, et al., Results from laboratory testing of a new four-barrel pellet injector for the TJ-II stellarator, Fusion Sci. Technol. 64 (3) (2013) 513–520, http://dx.doi.org/10.13182/fst13-a19144.
[168] J. Baldzuhn, H. Damm, C. Beidler, K. McCarthy, N. Panadero, C. Biedermann, S. Bozhenkov, K. Brunner, G. Fuchert, Y. Kazakov, et al., Pellet fueling experiments in Wendelstein 7-X, Plasma Phys. Control. Fusion 61 (9) (2019) 095012, http://dx.doi.org/10.1088/1361-6587/ab3567.
[169] A. Geraud, M. Lennholm, T. Alarcon, P. Bennett, D. Frigione, D. Garnier, P. Lang, A. Lukin, R. Mooney, I. Vinyar, et al., Status of the JET high frequency pellet injector, Fusion Eng. Des. 88 (6–8) (2013) 1064–1068, http://dx.doi.org/10.1016/j.fusengdes.2012.12.019.

[170] S.K. Combs, L.R. Baylor, Pellet-injector technology—brief history and key developments in the last 25 years, Fusion Sci. Technol. 73 (4) (2018) 493–518, http://dx.doi.org/10.1080/15361055.2017.1421367.

[171] N. Panadero, F. Koechl, A. Polevoi, J. Baldzuhn, C. Beidler, P. Lang, A. Loarte, A. Matsuyama, K. McCarthy, B. Pégourié, et al., A comparison of the influence of plasmoid-drift mechanisms on plasma fuelling by cryogenic pellets in ITER and Wendelstein 7-X, Nucl. Fusion 63 (4) (2023) 046022, http://dx.doi.org/10.1088/1741-4326/acbc34.

[172] R. Ishizaki, N. Nakajima, Magnetohydrodynamic simulation on pellet plasmoid in torus plasmas, Plasma Phys. Control. Fusion 53 (5) (2011) 054009, http://dx.doi.org/10.1088/0741-3335/53/5/054009.

[173] D.G. Swanson, Radio frequency heating in the ion-cyclotron range of frequencies, Phys. Fluids 28 (9) (1985) 2645–2677, http://dx.doi.org/10.1063/1.865224.

[174] F.W. Perkins, Heating tokamaks via the ion-cyclotron and ion-ion hybrid resonances, Nucl. Fusion 17 (6) (1977) 1197, http://dx.doi.org/10.2172/7310011.

[175] D. Start, J. Jacquinot, V. Bergeaud, V. Bhatnagar, S. Conroy, G. Cottrell, S. Clement, G. Ericsson, L.-G. Eriksson, A. Fasoli, et al., Bulk ion heating with ICRH in JET DT plasmas, Nucl. Fusion 39 (3) (1999) 321, http://dx.doi.org/10.1088/0029-5515/39/3/303.

[176] P. Bonoli, Linear theory of lower hybrid heating, IEEE Trans. Plasma Sci. 12 (2) (1984) 95–107, http://dx.doi.org/10.1109/tps.1984.4316302.

[177] M. Porkolab, Survey of lower hybrid experiments, IEEE Trans. Plasma Sci. 12 (2) (1984) 107–117, http://dx.doi.org/10.1109/tps.1984.4316303.

[178] P. Pereslavtsev, U. Fischer, M. Loughlin, L. Lu, E. Polunovskiy, S. Vielhaber, Modelling and shielding analysis of the neutral beam injector ports in ITER, Fusion Eng. Des. 98 (2015) 1585–1588, http://dx.doi.org/10.1016/j.fusengdes.2015.02.051.

[179] P. Sonato, P. Agostinetti, T. Bolzonella, F. Cismondi, U. Fantz, A. Fassina, T. Franke, I. Furno, C. Hopf, I. Jenkins, et al., Conceptual design of the DEMO neutral beam injectors: main developments and R&D achievements, Nucl. Fusion 57 (5) (2017) 056026, http://dx.doi.org/10.1088/1741-4326/aa6186.

[180] V. Erckmann, P. Brand, H. Braune, G. Dammertz, G. Gantenbein, W. Kasparek, H.P. Laqua, H. Maassberg, N.B. Marushchenko, G. Michel, M. Thumm, Y. Turkin, M. Weissgerber, A. Weller, W.E.T. at IPP Greifswald, W.E.T. at FZK Karlsruhe, W.E.T. at IPF Stuttgart, Electron cyclotron heating for W7-X: Physics and technology, Fusion Sci. Technol. 52 (2) (2007) 291–312, http://dx.doi.org/10.13182/FST07-A1508.

[181] T. Stange, H.P. Laqua, M. Beurskens, H.-S. Bosch, S. Bozhenkov, R. Brakel, H. Braune, K.J. Brunner, A. Cappa, A. Dinklage, V. Erckmann, G. Fuchert, G. Gantenbein, F. Gellert, O. Grulke, D. Hartmann, M. Hirsch, U. Höfel, W. Kasparek, J. Knauer, A. Langenberg, S. Marsen, N. Marushchenko, D. Moseev, N. Pablant, E. Pasch, K. Rahbarnia, H.T. Mora, T. Tsujimura, Y. Turkin, T. Wauters, R. Wolf, Advanced electron cyclotron heating and current drive experiments on the stellarator Wendelstein 7-X, in: J. Hillairet (Ed.), EPJ Web of Conferences, 157 (2017) 02008, http://dx.doi.org/10.1051/epjconf/201715702008.

[182] R.C. Wolf, S. Bozhenkov, A. Dinklage, G. Fuchert, H.P. Laqua, S. Marsen, N.B. Marushchenko, T. Stange, M. Zanini, I. Abramovic, A. Alonso, J. Baldzuhn, M. Beurskens, C.D. Beidler, H. Braune, K.J. Brunner, N. Chaudhary, H. Damm, G. Gantenbein, J. Geiger, M. Hirsch, U. Höfel, J. Jelonnek, Y.O. Kasakov, W. Kasparek, J. Knauer, A. Langenberg, C. Lechte, H. Trimino Mora, U. Neuner, D. Moseev, H. Oosterbeek, N. Pablant, E. Pasch, B. Plaum, T. Sunn Pedersen, K. Rhabarnia, J. Schilling, E. Scott, H. Thomsen, M. Thumm, Y. Turkin, F. Wilde, the Wendelstein 7-X Team, Electron-cyclotron-resonance heating in Wendelstein 7-X: A versatile heating and current-drive method and a tool for in-depth physics studies, Plasma Phys. Control. Fusion 61 (1) (2018) 014037, http://dx.doi.org/10.1088/1361-6587/aaeab2.

[183] B. Plaum, C. Lechte, W. Kasparek, S. Gaiser, A. Zeitler, V. Erckmann, M. Weißgerber, A. Bechtold, M. Busch, B. Szcepaniak, Design of a remote steering antenna for ECRH heating in the stellarator Wendelstein 7-X, Fusion Eng. Des. 96 (2015) 568–572, http://dx.doi.org/10.1016/j.fusengdes.2015.03.026.

[184] T. Omori, M. Henderson, F. Albajar, S. Alberti, U. Baruah, T. Bigelow, B. Beckett, R. Bertizzolo, T. Bonicelli, A. Bruschi, et al., Overview of the ITER EC H&CD system and its capabilities, Fusion Eng. Des. 86 (6–8) (2011) 951–954, http://dx.doi.org/10.1016/j.fusengdes.2011.02.040.

[185] S. Garavaglia, B. Baiocchi, A. Bruschi, D. Busi, F. Fanale, L. Figini, G. Granucci, A. Moro, P. Platania, N. Rispoli, et al., Progress of DTT ECRH system design, Fusion Eng. Des. 168 (2021) 112678, http://dx.doi.org/10.1016/j.fusengdes.2021.112678.

[186] A. Salvitti, A. Bruschi, D. Busi, F. Fanale, F. Giorgetti, G. Granucci, G. Calabrò, P. Fanelli, M. Nobili, Preliminary design and thermal analyses of the steerable mirror cooling channel of the DTT ECRH, Fusion Eng. Des. 161 (2020) 111880, http://dx.doi.org/10.1016/j.fusengdes.2020.111880.

[187] A. Bruschi, A. Allio, F. Fanale, P. Fanelli, S. Garavaglia, F. Giorgetti, G. Granucci, A. Moro, P. Platania, A. Romano, et al., Conceptual design of the DTT ECRH quasi-optical transmission line, Fusion Eng. Des. 194 (2023) 113727, http://dx.doi.org/10.1016/j.fusengdes.2023.113727.

[188] M. Tran, P. Agostinetti, G. Aiello, K. Avramidis, B. Baiocchi, M. Barbisan, V. Bobkov, S. Briefi, A. Bruschi, R. Chavan, et al., Status and future development of heating and current drive for the EU DEMO, Fusion Eng. Des. 180 (2022) 113159, http://dx.doi.org/10.1016/j.fusengdes.2022.113159.

[189] A. Bruschi, J.-P. Hogge, J. Jelonnek, D. Strauss, C. Wu, G. Aiello, K. Avramidis, B. Baiocchi, D. Birlan, R. Chavan, et al., Conceptual design of a modular EC heating system for EU-DEMO, Nucl. Fusion (2024) http://dx.doi.org/10.1088/1741-4326/ad66e3.

[190] J.M. Dawson, M.F. Uman, Heating a plasma by means of magnetic pumping, Nucl. Fusion 5 (3) (1965) 242, http://dx.doi.org/10.1088/0029-5515/5/3/009.

[191] R. Majeski, P. Probert, P. Moroz, T. Intrator, R. Breun, D. Brouchous, H. Che, J. DeKock, D. Diebold, M. Doczy, et al., Alfvén wave experiments in the phaedrus-t tokamak, Phys. Fluids B: Plasma Phys. 5 (7) (1993) 2506–2512, http://dx.doi.org/10.1063/1.860736.

[192] L. Villard, S. Brunner, A. Jaun, J. Vaclavik, Alfvén wave heating and stability, Phys. Scr. 1995 (T60) (1995) 44, http://dx.doi.org/10.1088/0031-8949/1995/t60/006.

[193] T. Intrator, P.H. Probert, M. Vukovic, S. Wukitch, A. Elfimov, R. Durst, R.A. Breun, D. Brouchous, D. Diebold, M. Doczy, et al., Alfvén ion–ion hybrid wave heating in the Phaedrus-T tokamak, Phys. Plasmas 3 (4) (1996) 1331–1339, http://dx.doi.org/10.1063/1.871786.

[194] B. Joye, A. Lietti, J. Lister, J.-M. Moret, W. Simm, Measurements of strong electron core heating during Alfven-wave heating on the TCA tokamak, Phys. Rev. Lett. 56 (23) (1986) 2481, http://dx.doi.org/10.1103/physrevlett.56.2481.

[195] G.S. Nusinovich, Introduction to the Physics of Gyrotrons, JHU Press, 2004, http://dx.doi.org/10.1353/book.62236.

[196] M. Thumm, State-of-the-art of high-power gyro-devices and free electron masers, J. Infrared Millim. Terahertz Waves 41 (1) (2020) 1–140, http://dx.doi.org/10.1007/s10762-019-00631-y.

[197] M. Thumm, State-of-the-Art of High-Power Gyro-Devices: Update of Experimental Results 2023, KIT Scientific Publishing, 2024, http://dx.doi.org/10.5445/KSP/1000164947.

[198] K. Sakamoto, M. Tsuneoka, A. Kasugai, T. Imai, T. Kariya, K. Hayashi, Y. Mitsunaka, Major improvement of gyrotron efficiency with beam energy recovery, Phys. Rev. Lett. 73 (26) (1994) 3532, http://dx.doi.org/10.1103/physrevlett.73.3532.

[199] A. Singh, S. Rajapatirana, Y. Men, V.L. Granatstein, R.L. Ives, A.J. Antolak, Design of a multistage depressed collector system for 1-MW CW gyrotrons. I. Trajectory control of primary and secondary electrons in a two-stage depressed collector, IEEE Trans. Plasma Sci. 27 (2) (1999) 490–502, http://dx.doi.org/10.1109/27.772278.

[200] J. Jelonnek, et al., Design considerations for future DEMO gyrotrons: a review on related gyrotron activities within EUROfusion, in: Symposium of Fusion Technology 2016, Prague, 123, Elsevier BV, 2016, pp. 241–246, http://dx.doi.org/10.1016/j.fusengdes.2017.01.047,

[201] G. Ling, B. Piosczyk, M.K. Thumm, A new approach for a multistage depressed collector for gyrotrons, IEEE Trans. Plasma Sci. 28 (3) (2000) 606–613, http://dx.doi.org/10.1109/27.887683.

[202] C. Wu, I. Pagonakis, S. Illy, M. Thumm, G. Gantenbein, J. Jelonnek, Preliminary studies on multistage depressed collectors for fusion gyrotrons, in: 2016 German Microwave Conference, GeMiC, IEEE, 2016, pp. 365–368, http://dx.doi.org/10.1109/gemic.2016.7461632.

[203] H. Laqua, K. Avramidis, H. Braune, I. Chelis, G. Gantenbein, S. Illy, Z. Ioannidis, J. Jelonnek, J. Jin, L. Krier, et al., The ECRH-power upgrade at the Wendelstein 7-?x stellarator, EPJ Web Conf. 277 (2023) 04003, http://dx.doi.org/10.1051/epjconf/202327704003.

[204] M. Thumm, Progress on gyrotrons for ITER and future thermonuclear fusion reactors, IEEE Trans. Plasma Sci. 39 (4) (2010) 971–979, http://dx.doi.org/10.1109/tps.2010.2095042.

[205] S. Illy, K.A. Avramidis, G. Gantenbein, Z. Ioannidis, J. Jin, P.C. Kalaria, I.G. Pagonakis, S. Ruess, T. Ruess, T. Rzesnicki, et al., Recent status and future prospects of coaxial-cavity gyrotron development at KIT, EPJ Web Conf. 203 (2019) 04005, http://dx.doi.org/10.1051/epjconf/201920304005.

[206] M.K. Thumm, G. Denisov, K. Sakamoto, M.Q. Tran, High-power gyrotrons for electron cyclotron heating and current drive, Nucl. Fusion 59 (7) (2019) 073001, http://dx.doi.org/10.1088/1741-4326/ab2005.

[207] T. Kariya, R. Minami, T. Imai, M. Okada, F. Motoyoshi, T. Numakura, Y. Nakashima, H. Idei, T. Onchi, K. Hanada, et al., Development of high power gyrotrons for advanced fusion devices, Nucl. Fusion 59 (6) (2019) 066009, http://dx.doi.org/10.1088/1741-4326/ab0e2c.

[208] M. Henderson, G. Saibene, C. Darbos, D. Farina, L. Figini, M. Gagliardi, F. Gandini, T. Gassmann, G. Hanson, A. Loarte, et al., The targeted heating and current drive applications for the ITER electron cyclotron system, Phys. Plasmas 22 (2) (2015) http://dx.doi.org/10.1063/1.4908598.

[209] A. Pochelon, Electron Cyclotron Resonance Heating, Tech. Rep., Ecole Polytechnique Federale, 1994, URL https://inis.iaea.org/records/rn6kh-ncw23.

[210] T.N. Todd, MHD control and ECCD in compass-D, Plasma Phys. Control. Fusion 35 (SB) (1993) B231, http://dx.doi.org/10.1088/0741-3335/35/sb/019.

[211] D. Strauss, G. Aiello, R. Bertizzolo, A. Bruschi, N. Casal, R. Chavan, D. Farina, L. Figini, M. Gagliardi, T. Goodman, et al., Nearing final design of the ITER EC H&CD upper launcher, Fusion Eng. Des. 146 (2019) 23–26, http://dx.doi.org/10.1016/j.fusengdes.2018.11.013.

[212] G. Janeschitz, K. Borrass, G. Federici, Y. Igitkhanov, A. Kukushkin, H. Pacher, G. Pacher, M. Sugihara, The ITER divertor concept, J. Nucl. Mater. 220 (1995) 73–88, http://dx.doi.org/10.1016/0022-3115(94)00447-1.

[213] T.S. Pedersen, R. König, M. Krychowiak, M. Jakubowski, J. Baldzuhn, S. Bozhenkov, G. Fuchert, A. Langenberg, H. Niemann, D. Zhang, et al., First results from divertor operation in Wendelstein 7-X, Plasma Phys. Control. Fusion 61 (1) (2018) 014035, http://dx.doi.org/10.1088/1361-6587/aaec25.

[214] J. Fellinger, M. Richou, G. Ehrke, M. Endler, F. Kunkel, D. Naujoks, T. Kremeyer, A. Menzel-Barbara, T. Sieber, J. Lobsien, et al., Tungsten based divertor development for Wendelstein 7-X, Nucl. Mater. Energy 37 (2023) 101506, http://dx.doi.org/10.1016/j.nme.2023.101506.

[215] R. Davies, Y. Feng, B. D., A semi-automated algorithm for designing stellarator divertor and limiter plates and application to HSX, Submitt. Nucl. Fusion (2024) http://dx.doi.org/10.1088/1741-4326/ad8017.

[216] H. Renner, J. Boscary, H. Greuner, H. Grote, F.W. Hoffmann, J. Kisslinger, E. Strumberger, B. Mendelevitch, Divertor concept for the W7-X stellarator and mode of operation, Plasma Phys. Control. Fusion 44 (6) (2002) 1005, http://dx.doi.org/10.1088/0741-3335/44/6/325.

[217] Y. Feng, W. team, Review of magnetic islands from the divertor perspective and a simplified heat transport model for the island divertor, Plasma Phys. Control. Fusion 64 (12) (2022) 125012, http://dx.doi.org/10.1088/1361-6587/ac9ed9.

[218] D. Bohm, The characteristics of electrical discharges in magnetic fields, Qual. Descr. Arc Plasma A Magn. Field (1949).

[219] K.-U. Riemann, The Bohm criterion and sheath formation, J. Phys. D: Appl. Phys. 24 (4) (1991) 493, http://dx.doi.org/10.1088/0022-3727/24/4/001.

[220] R.S. Cohen, L. Spitzer Jr., P.M. Routly, The electrical conductivity of an ionized gas, Phys. Rev. 80 (2) (1950) 230, http://dx.doi.org/10.1103/PhysRev.80.230.

[221] L. Spitzer Jr., R. Härm, Transport phenomena in a completely ionized gas, Phys. Rev. 89 (5) (1953) 977, http://dx.doi.org/10.1103/PhysRev.89.977.

[222] E. Strumberger, Magnetic field line diversion in helias stellarator configurations: perspectives for divertor operation, Nucl. Fusion 32 (5) (1992) 737, http://dx.doi.org/10.1088/0029-5515/32/5/I02.

[223] H. Renner, D. Sharma, J. Kisslinger, J. Boscary, H. Grote, R. Schneider, Physical aspects and design of the Wendelstein 7-X divertor, Fusion Sci. Technol. 46 (2) (2004) 318–326, http://dx.doi.org/10.13182/FST04-A570.

[224] N. Ohyabu, N. Noda, H. Ji, H. Akao, K. Akaishi, T. Ono, H. Kaneko, T. Kawamura, Y. Kubota, S. Morimoto, et al., Helical divertor in the large helical device, J. Nucl. Mater. 196 (1992) 276–280, http://dx.doi.org/10.1016/S0022-3115(06)80045-0.

[225] S. Masuzaki, T. Morisaki, N. Ohyabu, A. Komori, H. Suzuki, N. Noda, Y. Kubota, R. Sakamoto, K. Narihara, K. Kawahata, et al., The divertor plasma characteristics in the large helical device, Nucl. Fusion 42 (6) (2002) 750, http://dx.doi.org/10.1088/0029-5515/42/6/313.

[226] B. Nelson, L. Berry, A. Brooks, M. Cole, J. Chrzanowski, H.-M. Fan, P. Fogarty, P. Goranson, P. Heitzenroeder, S. Hirshman, et al., Design of the national compact stellarator experiment (NCSX), Fusion Eng. Des. 66 (2003) 169–174, http://dx.doi.org/10.1016/S0920-3796(03)00183-2.

[227] T. Mau, T. Kaiser, A. Grossman, A. Raffray, X. Wang, J.F. Lyon, R. Maingi, L. Ku, M. Zarnstorff, A.-C. Team, Divertor configuration and heat load studies for the ARIES-CS fusion power plant, Fusion Sci. Technol. 54 (3) (2008) 771–786, http://dx.doi.org/10.13182/FST08-27.

[228] Y. Gao, Y. Feng, M. Endler, M.W. Jakubowski, J. Geiger, S. Bozhenkov, A.P. Sitjes, F. Pisano, C.P. Dhard, D. Naujoks, et al., Improvement in the simulation tools for heat distribution predictions and control of baffle and middle divertor loads in Wendelstein 7-X, Nucl. Fusion 63 (2) (2023) 026031, http://dx.doi.org/10.1088/1741-4326/acaf0e.

[229] Y. Feng, H. Frerichs, M. Kobayashi, A. Bader, F. Effenberg, D. Harting, H. Hoelbe, J. Huang, G. Kawamura, J.D. Lore, T. Lunt, D. Reiter, O. Schmitz, D. Sharma, Recent improvements in the EMC3-eirene code, Contrib. Plasma Phys. 54 (4–6) (2014) 426, http://dx.doi.org/10.1002/ctpp.201410092.

[230] D. Bold, F. Reimold, H. Niemann, Y. Gao, M. Jakubowski, C. Killer, V.R. Winters, et al., Parametrisation of target heat flux distribution and study of transport parameters for boundary modelling in W7-X, Nucl. Fusion 62 (10) (2022) 106011, http://dx.doi.org/10.1088/1741-4326/ac7e2f.

[231] V.R. Winters, F. Reimold, R. König, M. Krychowiak, T. Romba, C. Biedermann, S. Bozhenkov, P. Drewelow, M. Endler, Y. Feng, et al., EMC3-EIRENE simulation of first wall recycling fluxes in W7-X with relation to H-alpha measurements, Plasma Phys. Control. Fusion 63 (4) (2021) 045016, http://dx.doi.org/10.1088/1361-6587/abe39c.

[232] D. Zhang, R. König, Y. Feng, R. Burhenn, S. Brezinsek, M. Jakubowski, B. Buttenschön, H. Niemann, A. Pavone, M. Krychowiak, et al., First observation of a stable highly dissipative divertor plasma regime on the Wendelstein 7-X stellarator, Phys. Rev. Lett. 123 (2) (2019) 025002, http://dx.doi.org/10.1103/physrevlett.123.025002.

[233] F. Effenberg, S. Brezinsek, Y. Feng, R. König, M. Krychowiak, M. Jakubowski, H. Niemann, V. Perseo, O. Schmitz, D. Zhang, et al., First demonstration of radiative power exhaust with impurity seeding in the island divertor at Wendelstein 7-X, Nucl. Fusion 59 (10) (2019) 106020, http://dx.doi.org/10.1088/1741-4326/ab32c4.

[234] T. Barbui, F. Effenberg, R. König, M. Krychowiak, O. Schmitz, J. Baldzuhn, B. Blackwell, B. Buttenschön, P. Drews, M. Jakubowski, et al., Radiative edge cooling experiments in Wendelstein 7-X start-up limiter campaign, Nucl. Fusion 59 (7) (2019) 076008, http://dx.doi.org/10.1088/1741-4326/ab18c5.

[235] H. Renner, J. Boscary, V. Erckmann, H. Greuner, H. Grote, J. Sapper, E. Speth, F. Wesner, M. Wanner, et al., The capabilities of steady state operation at the stellarator W7-X with emphasis on divertor design, Nucl. Fusion 40 (6) (2000) 1083, http://dx.doi.org/10.1088/0029-5515/40/6/306.

[236] M. Jakubowski, M. Endler, Y. Feng, Y. Gao, C. Killer, R. König, M. Krychowiak, V. Perseo, F. Reimold, O. Schmitz, et al., Overview of the results from divertor experiments with attached and detached plasmas at Wendelstein 7-X and their implications for steady-state operation, Nucl. Fusion 61 (10) (2021) 106003, http://dx.doi.org/10.1088/1741-4326/ac1b68.

[237] M. Beckers, Entwicklung eines Werkzeugs zur Modellierung der Nettoerosion im Hauptraum der Brennkammer eines Tokamaks und Studium der Plasma-Wand-Wechselwirkung an DEMO1 (Ph.D. thesis), University of Duesseldorf, 2018, URL https://docserv.uni-duesseldorf.de/servlets/DocumentServlet?id=44726.

[238] R. Wenninger, R. Albanese, R. Ambrosino, F. Arbeiter, J. Aubert, C. Bachmann, L. Barbato, T. Barrett, M. Beckers, W. Biel, L. Boccaccini, D. Carralero, D. Coster, T. Eich, A. Fasoli, G. Federici, M. Firdaouss, J. Graves, J. Horacek, M. Kovari, S. Lanthaler, V. Loschiavo, C. Lowry, H. Lux, G. Maddaluno, F. Maviglia, R. Mitteau, R. Neu, D. Pfefferle, K. Schmid, M. Siccinio, B. Sieglin, C. Silva, A. Snicker, F. Subba, J. Varje, H. Zohm, The DEMO wall load challenge, Nucl. Fusion 57 (4) (2017-02) 046002, http://dx.doi.org/10.1088/1741-4326/aa4fb4.

[239] A. Kallenbach, M. Bernert, R. Dux, L. Casali, T. Eich, L. Giannone, A. Herrmann, R. McDermott, A. Mlynek, H. Müller, F. Reimold, J. Schweinzer, M. Sertoli, G. Tardini, W. Treutterer, E. Viezzer, R. Wenninger, M. Wischmeier, the ASDEX Upgrade Team, Impurity seeding for tokamak power exhaust: from present devices via ITER to DEMO, Plasma Phys. Control. Fusion 55 (12) (2013) 124041, http://dx.doi.org/10.1088/0741-3335/55/12/124041.

[240] J. Lion, F. Warmer, H. Wang, A deterministic method for the fast evaluation and optimisation of the 3D neutron wall load for generic stellarator configurations, Nucl. Fusion 62 (7) (2022) 076040, http://dx.doi.org/10.1088/1741-4326/ac6a67.

[241] W.D. D'haeseleer, W.N.G. Hitchon, W.I. van Rij, S.P. Hirshman, J.L. Shohet, Flux Coordinates and Magnetic Field Structure, Springer, 1991, http://dx.doi.org/10.1007/978-3-642-75595-8.

[242] F. Warmer, E. Bubelis, First considerations on the balance of plant for a HELIAS fusion power plant, Fusion Eng. Des. 146 (2019) 2259–2263, http://dx.doi.org/10.1016/j.fusengdes.2019.03.167.

[243] T. Tanaka, A. Sagara, T. Goto, N. Yanagi, S. Masuzaki, H. Tamura, J. Miyazawa, T. Muroga, et al., Neutronics investigations for helical demo reactor FFHR-d1, Plasma Fusion Res. 7 (2012) 2405132, http://dx.doi.org/10.1585/pfr.7.2405132.

[244] I. Palermo, F. Warmer, A. Häußler, Nuclear design and assessments of helical-axis advanced stellarator with dual-coolant lithium-lead breeding blanket: adaptation from DEMO tokamak reactor, Nucl. Fusion 61 (7) (2021) 076019, http://dx.doi.org/10.1088/1741-4326/abfd71.

[245] I. Palermo, J. Alguacil, J.P. Catalán, I. Fernández-Berceruelo, J. Lion, J.Á.N. Valiente, D. Sosa, D. Rapisarda, F.R. Urgorri, F. Warmer, et al., Challenges towards an acceleration in stellarator reactors engineering: The dual coolant lithium–lead breeding blanket helical-axis advanced stellarator case, Energy 289 (2024) 129970, http://dx.doi.org/10.1016/j.energy.2023.129970.

[246] J. Alguacil, J. Catalan, I. Palermo, D. Sosa, J. Lion, F. Warner, J. Sanz, Fast generation of parametric neutronic models for stellarators. coupling HeliasGeom and GEOUNED, Fusion Eng. Des. 203 (2024) 114470, http://dx.doi.org/10.1016/j.fusengdes.2024.114470.

[247] A. Häußler, U. Fischer, F. Warmer, Verification of different Monte Carlo approaches for the neutronic analysis of a stellarator, Fusion Eng. Des. 124 (2016) 1207–1210, http://dx.doi.org/10.1016/j.fusengdes.2017.04.010.

[248] A. Häußler, F. Warmer, U. Fischer, Neutronics analyses for a stellarator power reactor based on the HELIAS concept, Fusion Eng. Des. 136 (2018) 345–349, http://dx.doi.org/10.1016/j.fusengdes.2018.02.026.

[249] G. Bongiovì, A. Häußler, P. Arena, Preliminary structural assessment of the HELIAS 5-B breeding blanket, Fusion Eng. Des. 146 (2019) 55–58, http://dx.doi.org/10.1016/j.fusengdes.2018.11.027.

[250] G. Bongiovì, G. Marra, R. Mozzillo, A. Tarallo, Heterogeneous design and mechanical analysis of HELIAS 5-B helium-cooled pebble bed breeding blanket concept, Int. J. Energy Res. 46 (3) (2022) 2748–2770.

[251] K. Mergia, N. Boukos, Structural, thermal, electrical and magnetic properties of Eurofer 97 steel, J. Nucl. Mater. 373 (1) (2008) 1–8, http://dx.doi.org/10.1016/j.jnucmat.2007.03.267.

[252] D. Brown, M. Chadwick, R. Capote, A. Kahler, A. Trkov, M. Herman, A. Sonzogni, Y. Danon, A. Carlson, M. Dunn, D. Smith, G. Hale, G. Arbanas, R. Arcilla, C. Bates, B. Beck, B. Becker, F. Brown, R. Casperson, J. Conlin, D. Cullen, M.-A. Descalle, R. Firestone, T. Gaines, K. Guber, A. Hawari, J. Holmes, T. Johnson, T. Kawano, B. Kiedrowski, A. Koning, S. Kopecky, L. Leal, J. Lestone, C. Lubitz, J. Márquez Damián, C. Mattoon, E. McCutchan, S. Mughabghab, P. Navratil, D. Neudecker, G. Nobre, G. Noguere, M. Paris, M. Pigni, A. Plompen, B. Pritychenko, V. Pronyaev, D. Roubtsov, D. Rochman, P. Romano, P. Schillebeeckx, S. Simakov, M. Sin, I. Sirakov, B. Sleaford, V. Sobes, E. Soukhovitskii, I. Stetcu, P. Talou, I. Thompson, S. van der Marck, L. Welser-Sherrill, D. Wiarda, M. White, J. Wormald, R. Wright, M. Zerkle, G. Žerovnik, Y. Zhu, ENDF/B-VIII.0: the 8th major release of the nuclear reaction data library with CIELO-project cross sections, new standards and thermal scattering data, Nucl. Data Sheets 148 (2018-02) 1–142, Special Issue on Nuclear Reaction Data https://doi.org/10.1016/j.nds.2018.02.001.

[253] R. Mozzillo, C. Bachmann, G. Aiello, D. Marzullo, Design of the European DEMO vacuum vessel inboard wall, Fusion Eng. Des. 160 (2020) 111967, http://dx.doi.org/10.1016/j.fusengdes.2020.111967.

[254] R. Lindau, A. Möslang, M. Rieth, M. Klimiankou, E. Materna-Morris, A. Alamo, A.-A. Tavassoli, C. Cayron, A.-M. Lancha, P. Fernandez, et al., Present development status of EUROFER and ODS-EUROFER for application in blanket concepts, Fusion Eng. Des. 75 (2005) 989–996, http://dx.doi.org/10.1016/j.fusengdes.2005.06.186.

[255] U. Fischer, L. Boccaccini, F. Cismondi, M. Coleman, C. Day, Y. Hörstensmeyer, F. Moro, P. Pereslavtsev, Required, achievable and target TBR for the European DEMO, Fusion Eng. Des. 155 (2020) 111553, http://dx.doi.org/10.1016/j.fusengdes.2020.111553.

[256] G. Bongiovì, P. Arena, P. Chiovaro, P.A. Di Maio, A. Del Nevo, R. Forte, Multi-module vs. Single-module concept: Comparison of thermomechanical performances for the DEMO water-cooled lithium lead breeding blanket, Fusion Eng. Des. 136 (2018) 1472–1478, Special Issue: Proceedings of the 13th International Symposium on Fusion Nuclear Technology (ISFNT-13), https://doi.org/10.1016/j.fusengdes.2018.05.037.

[257] P.K. Romano, B. Forget, The OpenMC monte carlo particle transport code, Ann. Nucl. Energy 51 (2013) 274–281, http://dx.doi.org/10.1016/j.anucene.2012.06.040.

[258] P.K. Romano, N.E. Horelik, B.R. Herman, A.G. Nelson, B. Forget, K. Smith, OpenMC: A state-of-the-art Monte Carlo code for research and development, Ann. Nucl. Energy 82 (2015) 90–97, http://dx.doi.org/10.1016/j.anucene.2014.07.048.

[259] P.P. Wilson, T.J. Tautges, J.A. Kraftcheck, B.M. Smith, D.L. Henderson, Acceleration techniques for the direct use of CAD-based geometry in fusion neutronics analysis, Fusion Eng. Des. 85 (10) (2010) 1759–1765, Proceedings of the Ninth International Symposium on Fusion Nuclear Technology, https://doi.org/10.1016/j.fusengdes.2010.05.030.

[260] J. Shimwell, CAD to DAGMC. Convert CAD geometry (STP files) or Cadquery assemblies to DAGMC h5m files, 2024, URL https://github.com/fusion-energy/cad_to_dagmc.

[261] D.X. Fischer, R. Prokopec, J. Emhofer, M. Eisterer, The effect of fast neutron irradiation on the superconducting properties of REBCO coated conductors with and without artificial pinning centers, Supercond. Sci. Technol. 31 (4) (2018) 044006, http://dx.doi.org/10.1088/1361-6668/aaadf2.

[262] Y. Zhai, D. van der Laan, P. Connolly, C. Kessel, Conceptual design of HTS magnets for fusion nuclear science facility, Fusion Eng. Des. 168 (2021) 112611, http://dx.doi.org/10.1016/j.fusengdes.2021.112611.

[263] U. Fischer, C. Bachmann, I. Palermo, P. Pereslavtsev, R. Villari, Neutronics requirements for a DEMO fusion power plant, Fusion Eng. Des. 98 (2015) 2134–2137, http://dx.doi.org/10.1016/j.fusengdes.2015.02.029.

[264] M. Norgett, M. Robinson, I.M. Torrens, A proposed method of calculating displacement dose rates, Nucl. Eng. Des. 33 (1) (1975) 50–54, http://dx.doi.org/10.1016/0029-5493(75)90035-7.

[265] K. Nordlund, S.J. Zinkle, A.E. Sand, F. Granberg, R.S. Averback, R. Stoller, T. Suzudo, L. Malerba, F. Banhart, W.J. Weber, et al., Improving atomic displacement and replacement calculations with physically realistic damage models, Nat. Commun. 9 (1) (2018) 1084, http://dx.doi.org/10.1038/s41467-018-03415-5.

[266] F. Sun, D. Chen, C. Hao, Y. Oya, J. Zhu, D. Li, L. Luo, Y. Wu, Estimation of different calculation models for evaluating heavy ion-induced damage in plasma facing materials, Fusion Eng. Des. 194 (2023) 113910, http://dx.doi.org/10.1016/j.fusengdes.2023.113910.

[267] D.R. Olander, A.T. Motta, A new book:'light-water reactor materials', Nucl. Eng. Technol. 37 (4) (2005) 309–316.

[268] Y. Iwamoto, S.-i. Meigo, S. Hashimoto, Estimation of reliable displacements-per-atom based on athermal-recombination-corrected model in radiation environments at nuclear fission, fusion, and accelerator facilities, J. Nucl. Mater. 538 (2020) 152261, http://dx.doi.org/10.1016/j.jnucmat.2020.152261.

[269] N. Baluc, K. Abe, J. Boutard, V. Chernov, E. Diegele, S. Jitsukawa, A. Kimura, R. Klueh, A. Kohyama, R.J. Kurtz, et al., Status of R&D activities on materials for fusion power reactors, Nucl. Fusion 47 (10) (2007) S696, http://dx.doi.org/10.1088/0029-5515/47/10/s18.

[270] S. Breidokaite, G. Stankunas, Helium production and material damage rate assessment in EU DEMO HCPB divertor, Radiat. Phys. Chem. 210 (2023) 111024, http://dx.doi.org/10.1016/j.radphyschem.2023.111024.

[271] M. Gilbert, S. Dudarev, D. Nguyen-Manh, S. Zheng, L. Packer, J.-C. Sublet, Neutron-induced dpa, transmutations, gas production, and helium embrittlement of fusion materials, J. Nucl. Mater. 442 (1–3) (2013) S755–S760, http://dx.doi.org/10.1016/j.jnucmat.2013.03.085.

[272] B. Van der Schaaf, C. Petersen, Y. De Carlan, J. Rensman, E. Gaganidze, X. Averty, High dose, up to 80 dpa, mechanical properties of Eurofer 97, J. Nucl. Mater. 386 (2009) 236–240, http://dx.doi.org/10.1016/j.jnucmat.2008.12.329.

[273] G. Pintsuk, G. Aiello, S.L. Dudarev, M. Gorley, J. Henry, M. Richou, M. Rieth, D. Terentyev, R. Vila, Materials for in-vessel components, Fusion Eng. Des. 174 (2022) 112994, http://dx.doi.org/10.1016/j.fusengdes.2021.112994.

[274] F. Arbeiter, E. Diegele, U. Fischer, A. Garcia, A. Ibarra, J. Molla, F. Mota, A. Möslang, Y. Qiu, M. Serrano, et al., Planned material irradiation capabilities of IFMIF-DONES, Nucl. Mater. Energy 16 (2018) 245–248, http://dx.doi.org/10.1016/j.nme.2018.05.026.

[275] U. Fischer, B. Bienkowska, K. Drozdowicz, M. Frisoni, F. Mota, F. Ogando, Y. Qiu, G. Stankunas, G. Tracz, Neutronics of the IFMIF-DONES irradiation facility, Fusion Eng. Des. 146 (2019) 1276–1281, http://dx.doi.org/10.1016/j.fusengdes.2019.02.057.

[276] L. Pilloni, C. Cristalli, O. Tassa, L. Bozzetto, E. Zanin, N. Bettocchi, Development of innovative materials and thermal treatments for DEMO water cooled blanket, Nucl. Mater. Energy 19 (2019) 79–86, http://dx.doi.org/10.1016/j.nme.2019.01.026.

[277] A.-A. Tavassoli, E. Diegele, R. Lindau, N. Luzginova, H. Tanigawa, Current status and recent research achievements in ferritic/martensitic steels, J. Nucl. Mater. 455 (1–3) (2014) 269–276, http://dx.doi.org/10.1016/j.jnucmat.2014.06.017.

[278] L. Tan, Y. Katoh, A.-A. Tavassoli, J. Henry, M. Rieth, H. Sakasegawa, H. Tanigawa, Q. Huang, Recent status and improvement of reduced-activation ferritic-martensitic steels for high-temperature service, J. Nucl. Mater. 479 (2016) 515–523, http://dx.doi.org/10.1016/j.jnucmat.2016.07.054.

[279] V. Cossu, F. Galleni, M. Eboli, A.D. Nevo, N. Forgione, S. Paci, Lithium-lead/water interaction: LIFUS5/Mod3 series E tests analysed by SIMMER-III coupled with RELAP5, Fusion Eng. Des. 190 (2023) 113537, http://dx.doi.org/10.1016/j.fusengdes.2023.113537.

[280] A. Tassone, A.D. Nevo, P. Arena, G. Bongiovi, G. Caruso, P.A. di Maio, G. di Gironimo, M. Eboli, N. Forgione, R. Forte, F. Giannetti, G. Mariano, E. Martelli, F. Moro, R. Mozzillo, A. Tarallo, R. Villari, Recent progress in the WCLL breeding blanket design for the DEMO fusion reactor, IEEE Trans. Plasma Sci. 46 (5) (2018) 1446–1457, http://dx.doi.org/10.1109/tps.2017.2786046.

[281] D. Uglietti, A review of commercial high temperature superconducting materials for large magnets: from wires and tapes to cables and conductors, Supercond. Sci. Technol. 32 (2019) http://dx.doi.org/10.1088/1361-6668/ab06a2.

[282] D. Larbalestier, A. Gurevich, D.M. Feldmann, A. Polyanskii, High-Tc superconducting materials for electric power applications, Nature 414 (6861) (2001) 368–377, http://dx.doi.org/10.1038/35104654.

[283] V. Braccini, A. Xu, J. Jaroszynski, Y. Xin, D.C. Larbalestier, Y. Chen, G. Carota, J. Dackow, I. Kesgin, Y. Yao, A. Guevara, T. Shi, V. Selvamanickam, Properties of recent IBAD–MOCVD coated conductors relevant to their high field, low temperature magnet use, Supercond. Sci. Technol. 24 (3) (2010) 035001, http://dx.doi.org/10.1088/0953-2048/24/3/035001.

[284] S. Hahn, K. Kim, K. Kim, X. Hu, T. Painter, I. Dixon, S. Kim, K.R. Bhattarai, S. Noguchi, J. Jaroszynski, D.C. Larbalestier, 45.5-Tesla direct-current magnetic field generated with a high-temperature superconducting magnet, Nature 570 (7762) (2019) 496–499, http://dx.doi.org/10.1038/s41586-019-1293-1.

[285] D.C. Van Der Laan, J.D. Weiss, D.M. McRae, Status of CORC cables and wires for use in high-field magnets and power systems a decade after their introduction, Supercond. Sci. Technol. 32 (3) (2019) 33001, http://dx.doi.org/10.1088/1361-6668/aafc82.

[286] M.J. Wolf, W.H. Fietz, C.M. Bayer, S.I. Schlachter, R. Heller, K.-P. Weiss, HTS CroCo: A stacked HTS conductor optimized for high currents and long-length production, IEEE Trans. Appl. Supercond. 26 (2) (2016) 19–24, http://dx.doi.org/10.1109/tasc.2016.2521323.

[287] L. Muzzi, A. Augieri, G. Celentano, S. Chiarelli, A. della Corte, G. De Marzi, A. Di Zenobio, L. Giannini, M. Marchetti, A. Masi, G. Messina, A. Rufoloni, S. Turtù, A. Vannozzi, A. Bragagni, M. Seri, M. Arabi, A. Anemona, A. Formichetti, Design and feasibility assessment of an HTS sector shaped high-current conductor for fusion coils, IEEE Trans. Appl. Supercond. 33 (5) (2023) 1–6, http://dx.doi.org/10.1109/TASC.2023.3236592.

[288] R.F. Vieira, D. Arsenault, R. Barnett, L. Bartoszek, W. Beck, S. Chamberlain, J.L. Cheng, E. Dombrowski, J. Doody, D. Dunn, J. Estrada, V. Fry, S. Garberg, T. Golfinopoulos, A. Greenberg, S. Heller, A. Hubbard, D. Korsun, S. Kuznetsov, B. LaBombard, C. Lammi, R. Leccacorvi, M. Levine, D.C. Mendoza, K. Metcalfe, P. Michael, T. Mouratidis, R. Mumgaard, J.P. Muncks, R. Murray, D. Nash, A. Pfeiffer, S. Pierson, A. Radovinsky, R. Rosati, M. Rowell, E. Salazar, S. Schweiger, S. Shiraiwa, B. Sorbom, P. Stahle, K. Stevens, D. Tammana, T. Toland, M. Vernacchia, E. Voirin, A. Warner, A. Watterson, D.G. Whyte, S. Wilcox, L. Zhou, A. Zhukovsky, Z.S. Hartwig, Design, fabrication, and assembly of the SPARC toroidal field model coil, IEEE Trans. Appl. Supercond. 34 (2) (2024) 1–15, http://dx.doi.org/10.1109/TASC.2024.3356571.

[289] D. Whyte, B. LaBombard, J. Doody, T. Golfinopolous, R. Granetz, C. Lammi, S. Lane-Walsh, P. Michael, T. Mouratidis, R. Mumgaard, et al., Experimental assessment and model validation of the SPARC toroidal field model coil, IEEE Trans. Appl. Supercond. 34 (2) (2023) 1–18, http://dx.doi.org/10.1109/tasc.2023.3332823.

[290] N. Yanagi, Y. Terazaki, S. Ito, K. Kawai, Y. Seino, T. Ohinata, Y. Tanno, K. Natsume, S. Hamaguchi, H. Noguchi, H. Tamura, T. Mito, H. Hashizume, A. Sagara, Progress of the design of HTS magnet option and R&D activities for the helical fusion reactor, IEEE Trans. Appl. Supercond. 24 (3) (2014) 4202805, http://dx.doi.org/10.1109/TASC.2013.2292775.

[291] N. Yanagi, S. Ito, Y. Terazaki, K. Natsume, H. Tamura, S. Hamaguchi, T. Mito, H. Hashizume, J. Morikawa, Y. Ogawa, M. Iwakuma, A. Sagara, Feasibility of HTS magnet option for fusion reactors, Plasma Fusion Res. 9 (2014) 1405013, http://dx.doi.org/10.1585/pfr.9.1405013.

[292] N. Deelen, B. Curé, A. Dudarev, M. Mentink, A. Vaskuri, High temperature superconductor detector magnets for future particle physics experiments, IEEE Trans. Appl. Supercond. 33 (5) (2023) 1–6, http://dx.doi.org/10.1109/TASC.2023.3243873.

[293] T. Mito, Y. Onodera, N. Hirano, K. Takahata, N. Yanagi, A. Iwamoto, S. Hamaguchi, S. Takada, T. Baba, N. Chikumoto, A. Kawagoe, R. Kawanami, Development of FAIR conductor and HTS coil for fusion experimental device, J. Phys. Commun. 4 (3) (2020) 035009, http://dx.doi.org/10.1088/2399-6528/ab7954.

[294] S. Imagawa, K. Takahata, H. Tamura, N. Yanagi, T. Mito, T. Obana, A. Sagara, Concept of magnet systems for LHD-type reactor, Nucl. Fusion 49 (7) (2009) 075017, http://dx.doi.org/10.1088/0029-5515/49/7/075017.

[295] COMSOL Multiphysics® v. 5.4. (Website), - Software COMSOL Multiphysics® V. 5.4 - Stockholm, Sweden, URL www.comsol.com.

[296] X. Zhang, Z. Zhong, H. Ruiz, J. Geng, T. Coombs, General approach for the determination of the magneto-angular dependence of the critical current of YBCO coated conductors, Supercond. Sci. Technol. 30 (2) (2016) 025010, http://dx.doi.org/10.1088/1361-6668/30/2/025010.

[297] S. Wimbush, N. Strickland, A. Pantoja, Critical current characterisation of SuperOx YBCO 2G HTS superconducting wire, 2021, http://dx.doi.org/10.6084/m9.figshare.13708690.v1.

[298] S.J. Sackett, EFFI: A Code for Calculating the Electromagnetic Field, Force, and Inductance in Coil Systems of Arbitrary Geometry, Tech. Rep. UCRL-52402, LLL, Univ. California, Oakland, CA, USA, 1978.

[299] C. Paz-Soldan, Non-planar coil winding angle optimization for compatibility with non-insulated high-temperature superconducting magnets, J. Plasma Phys. 86 (5) (2020) 815860501, http://dx.doi.org/10.1017/s0022377820001208.

[300] P. Huslage, D. Kulla, J.-F. Lobsien, T. Schuler, E.V. Stenson, Winding angle optimization and testing of small-scale, non-planar, high-temperature superconducting stellarator coils, Supercond. Sci. Technol. (2024) http://dx.doi.org/10.1088/1361-6668/ad5382.

[301] D.S. Nickel, W.H. Fietz, K.-P. Weiss, M.J. Wolf, Impact of bending on the critical current of HTS CrossConductors, IEEE Trans. Appl. Supercond. 31 (5) (2021) 1–4, Conference Name: IEEE Transactions on Applied Superconductivity, https://doi.org/10.1109/TASC.2021.3076491.

[302] M. Takayasu, J.V. Minervini, L. Bromberg, Torsion strain effects on critical currents of HTS superconducting tapes, AIP Conf. Proc. 1219 (1) (2010) 337–344, http://dx.doi.org/10.1063/1.3402320.

[303] F. Pierro, M. Delgado, L. Chiesa, X. Wang, S.O. Prestemon, Measurements of the strain dependence of critical current of commercial REBCO tapes at 15 T between 4.2 and 40 K for high field magnets, IEEE Trans. Appl. Supercond. 29 (5) (2019) 1–5, http://dx.doi.org/10.1109/TASC.2019.2902458.

[304] C. Barth, G. Mondonico, C. Senatore, Electro-mechanical properties of REBCO coated conductors from various industrial manufacturers at 77 K, self-field and 4.2 K, 19 T, Supercond. Sci. Technol. 28 (4) (2015) 045011, http://dx.doi.org/10.1088/0953-2048/28/4/045011.

[305] T. Lécrevisse, X. Chaud, P. Fazilleau, C. Genot, J.-B. Song, Metal-as-insulation HTS coils, Supercond. Sci. Technol. 35 (7) (2022) 074004, http://dx.doi.org/10.1088/1361-6668/ac49a5.

[306] W. Lee, D. Park, J. Bascuñán, Y. Iwasa, Partial-insulation HTS magnet for reduction of quench-induced peak currents, IEEE Trans. Appl. Supercond. 32 (6) (2022) 1–5, http://dx.doi.org/10.1109/tasc.2022.3156064.

[307] J.-B. Song, S. Hahn, Y. Kim, D. Miyagi, J. Voccio, J. Bascuñán, H. Lee, Y. Iwasa, Dynamic response of no-insulation and partial-insulation coils for HTS wind power generator, IEEE Trans. Appl. Supercond. 25 (3) (2014) 1–5, http://dx.doi.org/10.1109/tasc.2014.2384739.

[308] T. Mouratidis, D.G. Whyte, B. LaBombard, W.K. Beck, Performance of demountable solder joints for no-insulation superconducting coils produced by vacuum pressure impregnation, Supercond. Sci. Technol. 37 (2) (2024) 025006, http://dx.doi.org/10.1088/1361-6668/ad0b2b.

[309] T. Mouratidis, D.G. Whyte, Performance degradation due to thermal cycling in soldered Faraday and SuperPower HTS tape stacks, Supercond. Sci. Technol. 37 (5) (2024) 055001, http://dx.doi.org/10.1088/1361-6668/ad3313.

[310] Y. Wang, H. Song, D. Xu, Z.Y. Li, Z. Jin, Z. Hong, An equivalent circuit grid model for no-insulation HTS pancake coils, Supercond. Sci. Technol. 28 (4) (2015) 045017, http://dx.doi.org/10.1088/0953-2048/28/4/045017.

[311] S. Noguchi, S. Hahn, A newly developed screening current simulation method for REBCO pancake coils based on extension of PEEC model, Supercond. Sci. Technol. 35 (4) (2022) 044005, http://dx.doi.org/10.1088/1361-6668/ac5315.

[312] S. An, K. Choi, S. Noguchi, C. Im, J. Bang, U. Bong, J. Kim, S. Hahn, A feasibility study on "magnetic dam" to absorb magnetic energy in NI HTS magnet during quench, IEEE Trans. Appl. Supercond. 30 (4) (2020) 1–5, http://dx.doi.org/10.1109/tasc.2020.2972221.

[313] T. Mulder, M. Wozniak, A. Verweij, Quench protection of stacks of no-insulation HTS pancake coils by capacitor discharge, IEEE Trans. Appl. Supercond. (2024) http://dx.doi.org/10.1109/tasc.2024.3362755.

[314] M. Mentink, A. Dudarev, T. Mulder, J. Van Nugteren, H. ten Kate, Quench protection of very large, 50-GJ-class, and high-temperature-superconductor-based detector magnets, IEEE Trans. Appl. Supercond. 26 (4) (2016) 1–8, http://dx.doi.org/10.1109/TASC.2015.2510078.

[315] National Institute of Standards and Technology, Properties of Solid Materials from Cryogenic-to Room-Temperatures, U.S. Department of Commerce, Washington, D.C., URL https://trc.nist.gov/cryogenics/materials/materialproperties.htm.

[316] L. Bottura, Magnet quench 101, 2014, arXiv preprint arXiv:1401.3927.

[317] G. Ambrosio, Maximum allowable temperature during quench in Nb3Sn accelerator magnets, 2014, arXiv preprint arXiv:1401.3955.

[318] C. Sanabria, The SPARC tokamak central solenoid model coil test campaign, in: ASC 2024, Salt Lake City, 2024, Invited Talk.

[319] C. Sanabria, A. Radovinsky, C. Craighill, K. Uppalapati, A. Warner, J. Colque, E. Allen, S. Evcimen, S. Heller, D. Chavarria, K. Metcalfe, S. Lenzen, A. Hubbard, A. Watterson, S. Chamberlain, R. Diaz-Pacheco, B. Weinreb, E. Brownell, J. Nealey, A. Hughes, E. Laamanen, K. Vasudeva, D. Nash, C. McCormack, E. Salazar, O. Duke, M. Hicks, J. Adams, D. Kolb-Bond, T. Liu, K. Malhotra, D.P. Meichle, A. Francis, J. Cheng, M. Shepard, A. Greenberg, V. Fry, N. Kostifakis, C. Avola, P. Ljubicic, L. Palmer, G.S. Rajan, R. Padukone, S. Kuznetsov, K. Donez, T. Golfinopoulos, P.C. Michael, R. Vieira, N. Martovetsky, R. Badcock, M. Davies, A. Hunze, B. Ludbrook, R. Gupta, P. Joshi, S. Joshi, A.B. Yahia, H. Bajas, M. Jenni, C. Mueller, M. Holenstein, K. Sedlak, B. Sorbom, D. Brunner, Development of a high current density, high temperature superconducting cable for pulsed magnets, Supercond. Sci. Technol. 37 (11) (2024) 115010, http://dx.doi.org/10.1088/1361-6668/ad7efc.

[320] K.R. Bhattarai, K. Kim, K. Kim, K. Radcliff, X. Hu, C. Im, T. Painter, I. Dixon, D. Larbalestier, S. Lee, et al., Understanding quench in no-insulation (NI) REBCO magnets through experiments and simulations, Supercond. Sci. Technol. 33 (3) (2020) 035002, http://dx.doi.org/10.1088/1361-6668/ab6699.

[321] K.R. Bhattarai, K. Kim, S. Kim, S. Lee, S. Hahn, Quench analysis of a multiwidth no-insulation 7-t 78-mm REBCO magnet, IEEE Trans. Appl. Supercond. 27 (4) (2017) 1–5, http://dx.doi.org/10.1109/tasc.2017.2669962.

[322] P. Smith, Protection of superconducting coils, Rev. Sci. Instrum. 34 (4) (1963) 368–373, http://dx.doi.org/10.1063/1.1718368.

[323] M. Green, The role of quench back in quench protection of a superconducting solenoid, Cryogenics 24 (12) (1984) 659–668, http://dx.doi.org/10.1016/0011-2275(84)90034-1.

[324] M. Gasparotto, F. Elio, B. Heinemann, N. Jaksic, B. Mendelevitch, J. Simon-Weidner, B. Streibl, et al., The WENDELSTEIN 7-X mechanical structure support elements: Design and tests, Fusion Eng. Des. 74 (1–4) (2005) 161–165, http://dx.doi.org/10.1016/j.fusengdes.2005.06.039.

[325] S. Kinoshita, A. Shimizu, S. Okamura, M. Isobe, G. Xiong, H. Liu, Y. Xu, C. Team, et al., Engineering design of the Chinese first quasi-axisymmetric stellarator (CFQS), Plasma Fusion Res. 14 (2019) 3405097, http://dx.doi.org/10.1585/pfr.14.3405097.

[326] N. Jaksic, B. Mendelevitch, J. Tretter, Alternative conceptual design of a magnet support structure for plasma fusion devices of stellarator type, Fusion Eng. Des. 86 (6–8) (2011) 689–693, http://dx.doi.org/10.1016/j.fusengdes.2011.01.139.

[327] H. Tamura, N. Yanagi, T. Goto, J. Miyazawa, T. Tanaka, A. Sagara, S. Ito, H. Hashizume, Design modification of structural components for the helical fusion reactor FFHR-d1 with challenging options, Fusion Eng. Des. 124 (2017) 605–609, http://dx.doi.org/10.1016/j.fusengdes.2017.03.031.

[328] H. Tamura, T. Goto, J. Miyazawa, T. Tanaka, N. Yanagi, Seismic analysis of magnet systems in helical fusion reactors designed with topology optimization, IEEE Trans. Appl. Supercond. 32 (6) (2022) 1–4, http://dx.doi.org/10.1109/tasc.2022.3149731.

[329] M. Iguchi, T. Sakurai, M. Nakhira, N. Koizumi, H. Nakajima, Cryogenic structural materials of the ITER toroidal field coil structure, in: Fourth International Workshop on Structural Materials for Innovative Nuclear Systems (SMINS-4), Nuclear Energy Agency Paris, France, 2016.

[330] P. Lee, B. Hou, Z. Sun, D. Kang, S. Han, T. Zhang, D. Xu, T. Yan, B. Zhang, Design, qualification & manufacture of ITER gravity supports, Heliyon 6 (3) (2020) http://dx.doi.org/10.1016/j.heliyon.2020.e03609.

[331] M. Blair, T.L. Stevens, Steel Castings Handbook, ASM International, 1995.

[332] A. Boiler, ASME bOiler and Pressure Vessel Code: an International Code, American Society of Mechanical Engineers New York, 1998.

[333] E.-E.C. for Constructional Steelwork, Design of Steel Structures: Eurocode 3: Design of Steel Structures, Part 1-1: General Rules and Rules for Buildings, John Wiley & Sons, 2015.

[334] B. Standard, Eurocode 8: Design of structures for earthquake resistance, Part 1 (2005) 1998–1.
[335] O. Crofts, A. Loving, D. Iglesias, M. Coleman, M. Siuko, M. Mittwollen, V. Queral, A. Vale, E. Villedieu, Overview of progress on the European DEMO remote maintenance strategy, Fusion Eng. Des. 109 (2016) 1392–1398, http://dx.doi.org/10.1016/j.fusengdes.2015.12.013.
[336] C. Bachmann, C. Gliss, G. Janeschitz, T. Steinbacher, R. Mozzillo, Conceptual study of the remote maintenance of the DEMO breeding blanket, Fusion Eng. Des. 177 (2022) 113077, http://dx.doi.org/10.1016/j.fusengdes.2022.113077.
[337] A.R.R. X. R. Wang, Maintenance approaches for ARIES-CS compact stellarator power core, Fusion Sci. Technol. 47 (4) (2005) 1074–1078, http://dx.doi.org/10.13182/FST05-A829.
[338] V. Queral, F.A. Volpe, D. Spong, et al., Initial exploration of high-field pulsed stellarator approach to ignition experiments, J. Fusion Energy 37 (2018) 275–290, http://dx.doi.org/10.1007/s10894-018-0199-5.
[339] A.W. James Lilburne, Remote maintenance, safety and control (2020) (CCFE), EuroFusion Report S2-WP19.2-T003-D002, 2020.
[340] A. Sagara, S. Imagawa, O. Mitarai, T. Dolan, T. Tanaka, Y. Kubota, K. Yamazaki, K. Watanabe, N. Mizuguchi, T. Muroga, et al., Improved structure and long-life blanket concepts for heliotron reactors, Nucl. Fusion 45 (4) (2005) 258, http://dx.doi.org/10.1088/0029-5515/45/4/006.
[341] N. Yanagi, T. Goto, J. Miyazawa, H. Tamura, Y. Terazaki, S. Ito, T. Tanaka, H. Hashizume, A. Sagara, Progress in the conceptual design of the helical fusion reactor FFHR-d1, J. Fusion Energy 38 (2019) 147–161, http://dx.doi.org/10.1007/s10894-018-0193-y.
[342] J. Miyazawa, H. Tamura, T. Tanaka, T. Murase, T. Goto, N. Yanagi, R. Sakamoto, A. Sagara, et al., Cartridge-type helical blankets aiming at easy construction and maintenance for the FFHR-d1, Plasma Fusion Res. 12 (2017) 1405017, http://dx.doi.org/10.1585/pfr.12.1405017.
[343] I. Farquhar, J. Davies, J. Caumont, G. Keech, A. Loving, Parametric modelling of EU-DEMO remote maintenance strategies and concepts, Fusion Eng. Des. 145 (2019) 29–32, http://dx.doi.org/10.1016/j.fusengdes.2019.04.097.
[344] J. Keeton, An aid to the deisgn of radioactive areas, Nucl. Ind. Guid. (2009) URL https://www.nuclearinst.com/write/mediauploads/sdf%20documents/ventilation/nvf_dg001_ventilation_design_guide_issue_1_2009.pdf.
[345] A. Rolfe, P. Brown, P. Carter, R. Cusack, A. Gaberscik, L. Galbiati, B. Haist, R. Horn, M. Irving, D. Locke, et al., A report on the first remote handling operations at JET, Fusion Eng. Des. 46 (2–4) (1999) 299–306, http://dx.doi.org/10.1016/s0920-3796(99)00022-8.
[346] G. Rappé, The j.e.t. (joint European torus) vacuum vessel, Rev. Phys. Appl. 12 (10) (1977) 1735–1741, http://dx.doi.org/10.1051/rphysap:0197700120100173500.
[347] T. Kremeyer, R. König, S. Brezinsek, O. Schmitz, Y. Feng, V. Winters, L. Rudischhauser, B. Buttenschön, K. Brunner, P. Drewelow, E. Flom, G. Fuchert, Y. Gao, J. Geiger, M. Jakubowski, C. Killer, J. Knauer, M. Krychowiak, S. Lazerson, F. Reimold, G. Schlisio, H. Viebke, the W7-X Team, Analysis of hydrogen fueling, recycling, and confinement at Wendelstein 7-X via a single-reservoir particle balance, Nucl. Fusion 62 (3) (2022) 036023, http://dx.doi.org/10.1088/1741-4326/ac4acb.
[348] J. Miyazawa, H. Yamada, R. Sakamoto, H. Funaba, K. Watanabe, S. Sakakibara, K. Ida, M. Goto, T. Morisaki, S. Murakami, et al., Characteristics of the global energy confinement and central pressure in LHD, Fusion Sci. Technol. 58 (1) (2010) 29–37, http://dx.doi.org/10.13182/fst10-a10790.
[349] W.K. Hagan, E.A. Frieman, Nonlinear gyrokinetic theory, the direct interaction approximation, and anomalous thermal transport in tokamaks, Phys. Fluids 29 (11) (1986) 3635, http://dx.doi.org/10.1063/1.865793.
[350] J. Connor, Invariance principles and plasma confinement, Plasma Phys. Control. Fusion 30 (6) (1988) 619–650, http://dx.doi.org/10.1088/0741-3335/30/6/001.
[351] I.L. Shabalin, Tungsten, in: Ultra-High Temperature Materials I, Springer Netherlands, Dordrecht, 2014, pp. 237–315, http://dx.doi.org/10.1007/978-94-007-7587-9_3.
[352] R. Winterton, Where did the Dittus and Boelter equation come from? Int. J. Heat Mass Transfer 41 (4) (1998) 809–810, http://dx.doi.org/10.1016/S0017-9310(97)00177-4.
[353] National Institute of Standards and Technology, NIST Chemistry WebBook, U.S. Department of Commerce, URL https://webbook.nist.gov.
[354] C. Geuzaine, J.-F. Remacle, Gmsh: A 3-D finite element mesh generator with built-in pre- and post-processing facilities, Internat. J. Numer. Methods Engrg. 79 (11) (2009) 1309–1331, http://dx.doi.org/10.1002/nme.2579.
[355] I.A. Baratta, J.P. Dean, J.S. Dokken, M. Habera, J.S. Hale, C.N. Richardson, M.E. Rognes, M.W. Scroggs, N. Sime, G.N. Wells, DOLFINx: the next generation FEniCS problem solving environment, 2023, Published: preprint, https://doi.org/10.5281/zenodo.10447666.
[356] M.W. Scroggs, J.S. Dokken, C.N. Richardson, G.N. Wells, Construction of arbitrary order finite element degree-of-freedom maps on polygonal and polyhedral cell meshes, ACM Trans. Math. Softw. 48 (2) (2022) 18:1–18:23, http://dx.doi.org/10.1145/3524456.
[357] M.W. Scroggs, I.A. Baratta, C.N. Richardson, G.N. Wells, Basix: a runtime finite element basis evaluation library, J. Open Source Softw. 7 (73) (2022) 3982, http://dx.doi.org/10.21105/joss.03982.
[358] M.S. Alnaes, A. Logg, K.B. Ølgaard, M.E. Rognes, G.N. Wells, Unified form language: A domain-specific language for weak formulations of partial differential equations, ACM Trans. Math. Softw. 40 (2014) http://dx.doi.org/10.1145/2566630.
[359] G.T. Roberg-Clark, G.G. Plunk, P. Xanthopoulos, Coarse-grained gyrokinetics for the critical ion temperature gradient in stellarators, Phys. Rev. Res. 4 (2022) L032028, http://dx.doi.org/10.1103/PhysRevResearch.4.L032028.